OPTICAL PROPERTIES OF AlGaN NANOSTRUCTURES

By

SIVADASAN. A. K.
PHYS 02 2012 04 003

Indira Gandhi Centre for Atomic Research, Kalpakkam, Tamilnadu, India, 603102

A thesis submitted to the
Board of Studies in Physical Sciences

In partial fulfillment of requirements
for the Degree of
DOCTOR OF PHILOSOPHY
of
HOMI BHABHA NATIONAL INSTITUTE

November, 2016

Homi Bhabha National Institute

Recommendations of the Viva Voce Committee

As members of the Viva Voce Committee, we certify that we have read the dissertation prepared by Sivadasan. A. K. entitled "Optical Properties of AlGaN Nanostructures" and recommend that it may be accepted as fulfilling the thesis requirement for the award of Degree of Doctor of Philosophy.

Chairman - Prof. M. Kamruddin	**Date:** 10/3/17
Guide / Convener - Dr. Sandip Kumar Dhara	**Date:** 10-03-2017
Examiner - Prof. P. K. Giri	**Date:** 21/03/2017
Member 1- Dr. Sharat Chandra	**Date:** 10/03/2017
Member 2- Dr. T. R. Ravindran	**Date:** 10.3.2017

Final approval and acceptance of this thesis is contingent upon the candidate's submission of the final copies of the thesis to HBNI.

I/We hereby certify that I/we have read this thesis prepared under my/our direction and recommend that it may be accepted as fulfilling the thesis requirement.

Date: 10-03-2017

Place: Kalpakkam

Guide

STATEMENT BY AUTHOR

This dissertation has been submitted in partial fulfillment of requirements for an advanced degree at Homi Bhabha National Institute (HBNI) and is deposited in the Library to be made available to borrowers under rules of the HBNI.

Brief quotations from this dissertation are allowable without special permission, provided that accurate acknowledgement of source is made. Requests for permission for extended quotation from or reproduction of this manuscript in whole or in part may be granted by the Competent Authority of HBNI when in his or her judgment the proposed use of the material is in the interests of scholarship. In all other instances, however, permission must be obtained from the author.

Sivadasan. A. K.

DECLARATION

I, hereby declare that the investigation presented in the thesis has been carried out by me. The work is original and has not been submitted earlier as a whole or in part for a degree / diploma at this or any other Institution / University.

Sivadasan. A. K.

List of Publications Arising from the Thesis

Journals

1. “Far field photoluminescence imaging of single AlGaN nanowire in the sub–wavelength scale using confinement of polarized light”, **A. K. Sivadasan**, Manas Sardar and Sandip Dhara, *Ann. Phys. (Berlin)*, **2016**, 1–8. DOI; 10.1002/andp.201600165

2. “Interface phonon modes in the $[AlN/GaN]_{20}$ and $[Al_{0.35}Ga_{0.65}N/Al_{0.55}Ga_{0.45}N]_{20}$ 2D multi–quantum well structures”, **A. K. Sivadasan**, Chirantan Singha, A. Bhattacharyya and Sandip Dhara, *Phys. Chem. Chem. Phys.*, **2016**, *18*, 29864–29870

3. “The light–matter interaction of single semiconducting AlGaN nanowire and noble metal Au nanoparticle in the sub–diffraction limit”, **A. K. Sivadasan**, Kishore K. Madapu, and Sandip Dhara, *Phys. Chem. Chem. Phys.*, **2016**, *18*, 23680–23685

4. “Piezoelectric domains in the AlGaN hexagonal microrods: Effect of crystal orientations”, **A. K. Sivadasan**, G. Mangamma, Santanu Bera, M. Kamruddin and Sandip Dhara, *J. Appl. Phys.*, **2016**, *119*, 174304–9

5. “Polarized Raman and photoluminescence studies of a sub–micron sized hexagonal AlGaN crystallite for structural and optical properties”, **A. K. Sivadasan** and Sandip Dhara, *J. Raman. Spectrosc.*, **2016**, *47*, 656–611

6. “Optically confined polarized resonance Raman studies in identifying crystalline orientation of sub–diffraction limited AlGaN nanostructure”, **A. K. Sivadasan**, Avinash Patsha and Sandip Dhara, *Appl. Phys. Lett.*, **2015**, *106*, 173107–4

7. “Optical properties of mono–dispersed AlGaN nanowires in the single–prong growth mechanism”, **A. K. Sivadasan**, Avinash Patsha, S. Polaki, S. Amirthapandian, Sandip Dhara, Anirban Bhattacharya, B. K. Panigrahi, and A. K. Tyagi, *Cryst. Growth Des.*, **2015**, *15*, 1311–1318

8. “Surface optical phonon modes in hexagonal shaped 1D $Al_{0.97}Ga_{0.03}N$ nanorods”, **A. K. Sivadasan**, Chirantan Singha, K. G. Raghavendra, S. Amirthapandian, A. Bhattacharyya, Arup Dasgupta, and Sandip Dhara (*Communicated*)

Conference Proceedings

1. "The self–catalytic and catalyst assisted CVD growth of high optical quality AlGaN nanowires", **A. K. Sivadasan**, Santanu Parida, and Sandip Dhara, *AIP Conf. Proc.* **2017**

2. "Self–catalyzed growth of novel AlGaN hexagonal microrods", **A. K. Sivadasan**, S. R. Polaki, S. Ilango, and S. Dhara, *AIP Conf. Proc.* **2015**, *1665*, 140003–3

Conference Attended

1. "The self–catalytic and catalyst assisted CVD growth of high optical quality AlGaN nanowires", (Poster presentation), **A. K. Sivadasan**, Santanu Parida, and Sandip Dhara, *DAE Solid State Physics Symposium DAE SSPS*, 26–30, *Dec* **2016**, KIIT University, Bhubaneswar, India

2. "Crystal orientation dependent polarized photoluminescence of sub–micron sized GaN crystallite" (Poster presentation), **A. K. Sivadasan**, and Sandip Dhara, *Emerging Trends in Advanced Functional Materials* ETAFM, 18–21, *Jan* **2016**, Institute of Physics (IOP), Bhubaneswar, India

3. "The role of Purcell effect in the photoluminescence spectra of single AlGaN nanowire" (Short invited talk), **A. K. Sivadasan**, and Sandip Dhara, *World Congress on Microscopy: Instrumentation, Techniques and Applications in Life Sciences and Materials Sciences* WCM, 09–11, *Oct* **2015**, Mahathma Gandhi University, Kottayam, Kerala, India

4. "Polarized Raman studies in the optically confined sub–diffraction limited AlGaN nanostructure" (Contributory presentation), **A. K. Sivadasan**, Avinash Patsha, and Sandip Dhara, *Intl. Conf. Optics and Photonics* ICOP, 20–22, *Feb* **2015**, University of Calcutta, Kolkata, India

5. "Self–catalyzed growth of novel AlGaN hexagonal microrods", (Poster presentation), **A. K. Sivadasan**, S. R. Polaki, S. Ilango, and S. Dhara, *DAE Solid State Physics Symposium DAE SSPS*, 16–20, *Dec* **2014**, VIT University, Vellore, India

Others

1. “Invoking forbidden modes in SnO_2 nanoparticles using tip enhanced Raman spectroscopy” V. Bonu, A. Das, **A. K. Sivadasan**, A. K. Tyagi and S. Dhara, *J. Raman Spectrosc.* **2015**, *46*, 1037–1040

2. “Effect of annealing on the structural properties of vertical graphene nanosheets”, Subrata Ghosh, K. Ganesan, S. R. Polaki, **A. K. Sivadasan**, M. Kamruddin, and A. K. Tyagi, *Adv. Sc. Eng. Med.* **2016**, *8*,146–14

3. “Confocal Raman studies in determining crystalline nature of PECVD grown Si nanowires”, Nafis Ahmed, **A. K. Sivadasan**, S. Amirthapandian, P. Balaji Bhargav, S. Bhattacharya, P. Ramasamy, B. K. Panigrahi, A. K. Tyagi, and S. Dhara, *AIP Conf. Proc.* **2015**, *1665*, 050018–2

Sivadasan. A. K.

DEDICATIONS

"Dedicating My Thesis for the

Motivation of My Future

Students"

………………..*Alppettiyil Krishnankutty Sivadasan*

ACKNOWLEDGEMENTS

First of all, I am acknowledging everybody whoever helped me directly or indirectly to finish my Ph.D programme at IGCAR. I am taking this opportunity to express my deep and sincere gratitude to Dr. Sandip Dhara, Nanomaterials and Sensors Section, MSG, IGCAR for his constant encouragement with critical discussions during my research work.

I would like to thank the Director IGCAR, Dr. A. K. Bhaduri and the Director MSG, Dr. G. Amarendra for permitting me to pursue my Ph. D. I thank Dr. Saibaba for a nice hospitality at JRF Enclave and Department of Atomic Energy for financial support.

My sincere thanks to the former and present doctoral committee chairman Dr. A. K. Tyagi and Dr. M. Kamruddin, members, Dr. S. Chandra, and Dr. T. R. Ravindran for their continuous evaluations and valuable suggestions. I am thankful to my collaborators Dr. G. Mangamma, Dr. S. Amirthapandian, Dr. M. Sardar, Mr. S. R. Polaki, and Dr. B. K. Panigrahi, of MSG, IGCAR; Dr. S. Bera of WSCD, BARCF; Dr. A. Dasgupta and Mr. K. G. Raghavendra of MPD, IGCAR as well as Dr. A. Bhattacharyya and Dr. C. Singha of University of Calcutta, Kolkata for their contributions. I deeply express my heart–full thanks to all of my colleagues at NSS, Dr. A. Das, Dr. A. K. Prasad, Dr. A. Patsha, Mr. K. K. Madapu, Dr. B.V. Ramana, Mr. S. K. Parida, Mr. B. K. Sahu, Ms. R. Basu, Ms. P. R. Reshma and Dr. S. Ghosh, for sharing scientific thoughts.

It is my pleasure to remember my family members, A. K. Krishanankutty (*Achan*), Radha (*Amma*), A. K. Suresh Kumar (*Kuttan*), A. K. Baby (*Kunjipennu*) and Mr. V. M. Saji and former project guide Dr. S. N. Potty (C–MET, Thrissur), as well as my batchmates JRF–2012, Mr. A. D. Arun, classmates and teachers in Sri Vyasa College (Kerala), and all of my friends at Kalpakkam and Kondazhy, for their constant encouragements and supports.

……..Sivan (*Kunji*)

Optical Properties of AlGaN Nanostructures

CONTENTS

Page No.

CHAPTER 2: EXPERIMENTAL TECHNIQUES 59

SYNOPSIS

The wide–band gap group III nitride semiconductor materials are very important because of their applications in short wavelength and high frequency optoelectronic devices such as blue to UV and deep–UV light emitting diodes (LEDs) and laser diodes (LDs). The striking properties of these materials are significant hardness, large hetero–junction offsets, high thermal conductivity and melting temperature. InN, GaN, and AlN and its ternary (InGaN and AlGaN) and quaternary (InAlGaN) alloys are the well–known candidates for major optoelectronic applications. Along with optoelectronic properties, the III–nitride families are used in various applications such as photovoltaic, hydrogen storage, field emissions and gas sensing. It is reported that the dissociation of water into H and O can be achieved under the exposure of light on the surfaces of GaN nanowire (NW) arrays as wells as *p*–type InGaN or GaN/InGaN multi–band hetero–structures.

The scientific community already developed different one dimensional (1D) nanostructures such as nanotubes, NWs, and nanocones for the binary AlN, GaN, and InN and their alloys. The NWs find enormous utility in a variety of optoelectronics applications, as high aspect ratio leads to the strain relaxation of the material without the formation of dislocation. This thesis contains, the synthesis of 1D AlGaN NWs by atmospheric pressure chemical vapor deposition (APCVD) technique *via* Au naoparticle (NP) assisted vapor–liquid–solid (VLS) growth mechanism. Along with NWs, reports are also available for the sub–micro and microrod structures of group III nitrides. These structures are also used for demonstrating room–temperature continuous wave lasing *via* high–Q whispering gallery modes (WGM) which are applicable for LDs. The presence of WGMs in the microrods is a signature of excellent morphological, structural, and high optical quality of the material. The synthesis part of the present thesis does also deal with the growth of high quality, single crystalline, hexagonal shaped, AlGaN sub–micro and mocrorods using APCVD technique *via* self catalytic vapor–solid (VS) growth mechanism.

Vertically aligned nanostructures and microrods are attractive for 1D light emitting device for its applications in exclusively for making coaxial quantum well (QW) structures. The performances of such devices are dependent on both the crystalline as well as the electronic properties of the material. In this context, the understanding of the crystalline properties of the sub–micron sized cystallite using Raman spectroscopy is not only a very efficient non–destructive characterization tool for the phase confirmation of the material, but also capable to investigate the crystallographic orientation in agreement with the Raman selection rules for different polarization configurations. There are several reports available for polarized as well as angle dependent polarized Raman studies collected from a single spot on the crystals. Moreover, the polarized Raman imaging corresponding to the peak intensities of the Raman allowed vibrational modes throughout different crystal planes may help us to predict the exact crystalline orientation and compositional homogeneity of the material. The Raman imaging as a technique for testing the single crystalline nature of the material is not well utilized yet. Therefore, the present dissertation assures the capability of polarized Raman imaging studies to investigate the single crystalline nature of the hexagonal sub–microrods.

The wurtzite III–nitrides are non–centrosymmetric crystals which show inbuilt spontaneous polarizations. Consequently, a piezoelectric potential may be generated across the crystal by applying an external stress or vice versa. Therefore, these features can be utilized for different micro–mechanical devices such as micro–actuators, micro–sensors, ultrasonic motors, micro–pumps, self–powered devices, electro–mechanical sensing, mechanical energy harvesting and other various applications as MEMS based device. It is reported that the III–nitrides, grown along the *c*–axis [0001] with polar orientation, lead to a huge amount of intrinsic electric field which degrades the efficiency of LEDs. Therefore, it is very important to study the crystallographic orientation dependent optical properties of these III–nitrides. The problems due to the polarity of the crystals can be overcome for the low dimensional systems by allowing the growth along non–polar directions normal to *a*– (1-120) and *m*–plane (1-100) instead of the *c*–plane (0001). These polarities of the crystal plane also can influence the polarized photoluminescence (PL) spectra. The investigations of the effect of intrinsic electric field on the crystal orientation dependent PL spectra are also included in the thesis. The crystal orientation dependent piezo–response force microscopic (PFM) studies are incorporated in the thesis for confirming the existence of internal electric field as well as the observation of spontaneous and piezoelectric domains of single crystalline AlGaN microrods, which supports the observed crystal orientation dependent PL emissions.

The remarkable scope of applications and importance of group III nitrides, as mentioned above, motivated the researchers to establish almost all the characteristic features of these materials including the detailed study of the phonon modes. However, there are only few reports available on specific class of phonon modes, which can be localized only on the surfaces of nanostructures. The reduction of size in the materials up to nanometer scale reduces the degrees of freedom for phonon leading to the spatial confinement of the bulk phonon modes. It may also change significantly the density of phonon states, responsible for the origin of surface and interface related optical phonon modes. The frequency of such surface lattice vibrations are found in between the transverse optical ($\mathrm{TO}_{q=0}$) and longitudinal optical ($LO_{q=0}$) phonon modes at Brillouin zone center (Wave vector, $q=0$). The vibration of surface atoms, with amplitudes confined near to the surface, decrease exponentially with depth and is named as surface optical (SO) phonon modes, also known as Fröhlich modes. The SO modes are observed because of the breakdown of translational symmetry of the surface potential due to the surface roughness or creation of periodic structures and interfaces or formation of grating in the surface of nanostructures. The breakdown of translational symmetry of surface potential corresponding to the periodicity leads to an additional crystal momentum that allows the generation of some phonon modes away from zone centre (non–zone centre, $q\neq0$).The identification of such SO phonon mode is difficult to be detected in the case of bulk materials because of the constraint in conservation of momentum due to their perfect crystalline symmetry. Therefore, the nanomaterials such as 1D NWs, 2D multi–QWs (MQWs) and superlattices (SLs) with a large surface area contribute better SO or interface optical (IO) phonon signal compared to that of the bulk crystals. It was well established that, the SO phonon mode frequency depends on the dielectric constant of the surrounding medium (ε_m) as well as the shape, size, interfaces, saw tooth edges, periodicity, diameter modulations and density of the nanostructures. The studies involved in the thesis includes the calculations of SO phonon mode frequencies from the theoretically simulated dispersion curve for the periodic surface modulations due to the presence of sharp edges at the corners of well–faceted 1D $Al_{0.97}Ga_{0.03}N$ hexagonal crystallites in the sample as well as an equivalent periodicity generated due to the row and columnar array of NRs, in presence of different media of air and CCl_4. Because of the capability to create 2D electron gas at the hetero–junctions, the III–nitrides especially AlGaN/GaN MQWs and SLs are used for the development of high electron mobility transistors (HEMT) along with the hetero–junction field effect transistors (HJFET) and bipolar transistors.[1-3] The SLs and MQWs of AlGaN/GaN with different Al percentages are used as active region as well as buffer, carrier confining and electron blocking layers (EBL) to improve the internal and external quantum efficiency of blue, UV and deep–UV LEDs and LDs.[1-3] Because of the above discussed importance of MQWs and SLs, the studies involved in the thesis also investigated the behavior of IO phonon modes in the Raman spectra of $[AlN/GaN]_{20}$ and $[Al_{0.35}Ga_{0.65}N/Al_{0.55}Ga_{0.45}N]_{20}$ 2D MQWs.

The light–matter interaction in the near–field regime at the vicinity of nanostructures is a very interesting as well as challenging task in the scientific community. The Abbe's diffraction limit prevents conventional optical microscopes to possess a spatial resolution beyond the value of $\sim\lambda/2$, where λ is the wavelength of excitation light with a maximum numerical aperture (N.A.) value of unity for the probing objective. The rate of interaction of a light emitting material with electromagnetic (*em*) radiation can be enhanced by keeping it in a micro–cavity. The spontaneous emission rate is not only a material characteristic but also depends on the photon density (energy density of the fluctuating *em* field) in the surrounding environment. The long lived interactive photons, enhances the photon density leading to the improved emission/absorption of light in the process of Purcell enhancement. Tightly confined light or trapped photons in between two semiconductor or dielectric media with sizes comparable to the wavelength of the confined light, increases photon density leading to the enhanced light–matter interaction, enabling a range of non–linear applications. The optical confinement of polarized light enabled us to record the far–field PL imaging of a single AlGaN NW, in the sub–diffraction length scale. Moreover, this thesis tried to shed a glimpse on, how the proximity of other NWs influence on the PL spectra of a single and isolated NW, even though the separation between the nearest NWs is more than the exciting laser beam diameter. The optical confinement of polarized light, which may enhance the light–matter interaction between two semiconductor or dielectric media along with strong electron–phonon coupling in the polarized resonance Raman spectroscopy (RRS) allow us to understand the crystallographic orientations of single NW in the sub–diffraction length scale.

The near–field scanning optical microscopy (NSOM) assisted with the help of plasmonics is a unique tool to understand the light–matter interaction in the near–field regime for optical and spectroscopic imaging of nanostructures in the sub–diffraction limit. In the near–field regime, the confined light with evanescent field components emanating from the NSOM probe is not diffraction limited. The light–matter interaction in metallic nanostructures have opened to a new branch of surface plasmon (SP) based photonics, called plasmonics. The coupling of the incident *em* waves to the coherent oscillation of free–electron plasma near the metal surface is known as a surface plasmon polariton (SPP) and it is a propagating surface wave at the continuous metal–dielectric interface. The *em* field perpendicular to the metal surface decays exponentially and is known as evanescent waves providing sub–wavelength confinement near to the metal surface. Matching of the incident excitation frequency (ω) of *em* wave with the plasmon frequency (ω_p) of the electrons in metal nanostructures, leads to an enhanced light–matter interaction, known as surface plasmon resonance (SPR). The NSOM studies in the dissertation, is tried to establish the light–matter interaction of an isolated single and semiconductor AlGaN NW (diameter ~120 nm) grown *via* VLS mechanism along with metallic Au NP catalysts (diameter ~10–150 nm) in the near–field regime with a laser excitation of 532 nm (2.33 eV).

The studies included in the thesis are organized into seven chapters and the contents of each chapter are summarized as follows:

Chapter 1: Introduction

The Chapter 1 provides a brief outlines of the group III nitrides including its crystal structure, physico–chemical properties and significance of non–centrosymmetric nature which leads to the origin of intrinsic crystalline fields. The present status and developments in optical properties of 1D and 2D nanostructures and their applications are introduced along with the discussions of SO and IO phonon modes in the nanostructures. The possibilities of enhanced light–matter interactions in the sub–diffraction regime are briefly described with the help of different effects of photonic and plasmonics confinement as well as near–field interactions. The objectives of the present thesis are briefed at the end of the Chapter 1.

Chapter 2: Experimental Techniques

The Chapter 2 describes, the experimental techniques used to synthesis and characterize the AlGaN nanostructures in details. The major tools and techniques involved in the thesis are categorized as follows; synthesis techniques as well as characterization tools required for morphological, structural, and elemental analysis. The optical characterization tools used for vibrational and luminescence studies are also briefly discussed. The basic features of scanning probe microscopy (SPM) including atomic force microscopy (AFM), PFM and NSOM are also briefly introduced.

Chapter 3: Growth of AlGaN by Chemical Vapor Deposition Technique

The Chapter 3 includes the description of growth process of mono–dispersed and cylindrical shaped as well as high dense and triangular shaped AlGaN NWs of ternary wurtzite phase using APCVD *via* VLS process. The role of distribution of Au catalyst NPs on the size and the shape of AlGaN NWs along with the optimization of flow rate and decomposition temperature of $NH_{3,}$ during the growth process are discussed. These variations in the morphology of the NWs are understood by invoking Ostwald ripening of Au catalyst NPs at high temperature followed by the effect of single and multi–prong growth mechanism. Energy–filtered transmission electron microscopy is used as an evidence for the presence of Al in the as prepared samples. The Raman study reveals the formation of AlGaN NWs in the wurtzite phase. A significant blue shift of the band gap of ~3.55 eV as compared to ~3.47 eV for GaN at 300K was observed in the PL spectra, in the absence of quantum confinement effect in the NWs with diameter ~100 nm. Thus, the blue shift of the band edge peak is used as a supportive evidence for the AlGaN alloy formation. The corresponding approximate Al percentage, incorporated in the AlGaN NWs, is estimated to be ~3.0 at.%. Moreover, the simultaneous presence of Raman modes corresponding to GaN– E_2^H at 567 cm^{-1} and AlN– E_2^H at 668 cm^{-1} confirms the two mode behavior of AlGaN random alloy formation.

AlGaN sub–micro and microrods are also grown *via* self catalytic VS mechanism by APCVD on AlN base layer over intrinsic Si(100) as well as sapphire substrates. The growth process is substantiated using X–ray diffraction (XRD) and X–ray photoelectron spectroscopy (XPS) studies. The growth of self catalytic elongated AlGaN NWs are also carried out on the Al–Ga thin film. The Raman and PL study reveal the formation of AlGaN microrods in the wurtzite phase and ensures the high optical quality of the crystalline material. Similarly, the AlGaN sub–micro rods also shows the signature of mixed modes for the random alloy formation identified from the existence of two mode behavior of E_2^H and one mode behavior of A_1(LO) phonon modes in the observed Raman spectra. The approximate Al percentage is estimated to be 2.0–3.0 at.% from the blue shift of A_1(LO) phonon modes as well as the band edge emission in the PL spectra.

Chapter 4: Optical Properties: Effect of Crystallographic Orientations

The Chapter 4 mainly covers the crystal orientation dependent studies of hexagonal shaped AlGaN crystallites. The polarized Raman spectroscopy is capable of giving confirmation about the crystalline phase as well as the crystallographic orientation of the sample. The sub–micron sized hexagonal AlGaN crystallites are grown by self–catalytic VS process under N–rich condition used for the polarized Raman spectra in different crystalline orientations along with spectral imaging studies. The results obtained from the polarized Raman spectral studies shows single crystalline nature of sub–micron sized hexagonal AlGaN crystallites. In this context, apart from X–ray and electron diffraction tools, polarized Raman spectroscopy and the corresponding spectral imaging also can be an alternative as well as promising tool for determining both crystalline phase and orientation.

Optical properties of the sub–microrods for different crystalline orientations are also studied using polarized PL measurements. The influence of internal crystal field to the PL spectra is proposed to explain the observation of distinct splitting of emission intensity. The origin of enhanced splitting in the PL spectra along the *c*–plane compared to that of *m*–plane may be because of the interaction of electric field of the excitation wave with the intrinsic crystal field, which is the resultant of the spontaneous and strain related piezoelectric polarizations. The existence of crystal orientation dependent intrinsic electric field in the single crystal is investigated by the PFM imaging of AlGaN hexagonal microrods. The reasons for the contrast variation in the PFM image may be because of the variation of surface charge density over the surface of AlGaN microrods originated due to the crystalline orientation with respect to its AlN base layer. The effective piezoelectric coefficient for

AlGaN microrod along the *c*–axis (d_{33}) is found to be ~4.14 pm/V which falls well within the reported values of 5.10 and 3.10 pm/V of pure GaN and AlN, respectively.

Chapter 5: Surface and Interface Optical Phonon Modes in 1D Nanostructures and 2D Multi–Quantum Well Structures

The Chapter 5 mainly deals with the study of SO and IO phonon modes of 1D and 2D nanostructures of III–nitrides probed by the Raman spectroscopy. The plasma assisted molecular beam epitaxy (PAMBE) grown, vertically aligned and hexagonal shaped 1D $Al_{0.97}Ga_{0.03}N$ nanorods (NRs) are used for study the SO modes in this thesis. Apart from the group theoretically allowed optical phonons at zone center (q=0), two additional phonon modes around ~763 and ~846 cm^{-1} are observed in between the reported values of longitudinal optical ($LO_{q=0}$) and transverse optical ($TO_{q=0}$) phonon modes. Consequently, the observed phonon modes are calculated from the simulated dispersion curve and subsequently assigned as SO phonon modes of SO(A_1) and SO(E_1) with A_1 and E_1 symmetries, respectively. A change in the dielectric medium (ε_m=2.24) using CCl_4 is demonstrated to show a significant red shift of the additional modes with respect to those in air, authenticating the presence of SO phonon modes in the Raman spectra of $Al_{0.97}Ga_{0.03}N$ NRs, as it shows good agreement with the calculated SO phonon frequencies. The origin of SO phonon modes are attributed to the relaxation of Raman selection rules away from the Brillouin zone centre because of the presence of periodic surface modulations due to the presence of sharp edges at the corners of well–faceted 1D $Al_{0.97}Ga_{0.03}N$ hexagonal crystallites in the sample. An appropriate quantification is also made in this regard to find out the Fourier component of the surface potential responsible for the activation of SO mode.

The observation of IO phonon modes in the recorded Raman spectra of *c*–plane oriented [AlN(~1.25 nm)/GaN(~2.0 nm)/]$_{20}$ and [Al$_{0.35}$Ga$_{0.65}$N(~1.25 nm)/Al$_{0.55}$Ga$_{0.45}$N(~2.0 nm)]$_{20}$ MQW structures grown *via* PAMBE are also studied. The wavelength and wave vector leading to the formation of IO modes are calculated from the multiple periodicity of SLs in the 2D MQW structures. The nominal shift (~4 cm^{-1}) in IO phonon mode of E_1 symmetry (IO(E_1)) for [Al$_{0.35}$Ga$_{0.65}$N/Al$_{0.55}$Ga$_{0.45}$N]$_{20}$ compared to that of the [AlN/GaN]$_{20}$ MQW structure is understood on the basis of change in dielectric constants (ε_m) of the surrounding medium. The observed IO phonon modes in the spectra are attributed to the breakdown of translation symmetry of surface potential due to the presence of the periodic interfaces and surface modulations in the SL structures of MQWs. The corresponding required edge lengths of 2D plates are computed from the simulated dispersion relation curve of IO modes. The integral multiples of uniformly distributed platelets, originated due to the horizontal uneven irregularities on the surface of SLs, are matched with the calculated L values.

Chapter 6: Light–Matter Interactions of Nanostructures in the Sub–Diffraction Regime

In Chapter 6, the role of nanostructures for light–matter interaction in the sub–wavelength regime is discussed. Till now, the nanoscale focusing and imaging in the sub–diffraction limit is achieved mainly with the help of plasmonic field enhancement assisted with noble metal nanoparticles. Using far–field imaging technique, for the first time, we have recorded polarized spectroscopic PL imaging of a single AlGaN NW of size in the sub–diffraction limit with diameter ~100 nm using the optical confinement of polarized light. It is found that the PL from a single NW is influenced by the proximity to other NWs with the PL intensity proportional to $1/(l \times d)$, where l and d are the NW length and the separation from the neighboring NW, respectively. In case of the optical confinement effect, a non–zero non–

equilibrium population of long lived photons is envisaged to influence the increased PL emission intensity from the single NW. The enhancement of PL emission facilitated the far–field spectroscopic imaging of a single semiconductor AlGaN NW in the sub–diffraction regime. As a matter of fact, the optical confinement effect due to the dielectric contrast of NW with respect to that of surrounding media assisted with electron–phonon coupling of RRS helped us to understand the crystalline orientation of a single AlGaN NW of size in the sub–diffraction limit with diameter ~100 nm. The results are compared and matched with the high resolution transmission electron microscopic (HRTEM) analysis.

The NSOM is not only a tool for imaging of sub–diffraction limited objects but also a prominent characteristic tool for understanding the intrinsic properties of the nanostructures. In order to understand the light–matter interactions in the near–field regime using NSOM technique with an excitation of 532 nm (2.33 eV), we selected an isolated single semiconductor AlGaN NW of diameter ~120 nm along with metallic Au NP catalyst. The role of electronic transitions from different native defect related energy states of AlGaN are discussed in understanding the NSOM images for the semiconductor NW. The effect of strong SPR related absorption of excitation laser in the NSOM images for Au NP is also observed.

Chapter 7: Brief Summary of Thesis and Scope of Future Work

In Chapter 7, the major findings of the thesis are summarized. The directions for future research work are also proposed to explore optoelectronic properties, perform localized charge transfer process to understand sensing mechanism and also to probe localized spectroscopic studies on AlGaN nanostructures.

LIST OF FIGURES

LIST OF TABLES

LIST OF ABBREAVIATIONS

1	2D Electron Gas	2DEG
2	Aluminium Gallium Nitride	AlGaN
3	Atmospheric Pressure Chemical Vapor Deposition	APCVD
4	Atomic Force Microscopy	AFM
5	Back Scattered Electrons	BSEs
6	Electromagnetic	*em*
7	Electron Blocking Layers	EBL
8	Electron Energy Loss Spectroscopy	EELS
9	Energy Filtered Transmission Electron Microscopy	EFTEM
10	Energy Dispersive Spectroscopy	EDS
11	Fast Fourier Transform	FFT
12	Field Emission Scanning Electron Microscopy	FESEM
13	Free Exciton	FE
14	Glancing Incidence X–ray Diffraction	GIXRD
15	High Electron Mobility Transistor	HEMT
16	High Resolution TEM	HRTEM
17	Interface	IF
18	Interface Optical	IO
19	Inverse Fast Fourier Transform	IFFT
20	Inverse Fourier Transform	IFT
21	Kinetic Energy	KE
22	Laser Diodes	LDs
23	Light Emitting Devices/Diodes	LEDs
24	Longitudinal Optical	LO
25	Lyddane–Sachs–Teller	LST

26	Multi–QW	MQW
27	Nanoparticles	NPs
28	Nanorods	NRs
29	Nanowires	NWs
30	Near–field scanning optical microscopy	NSOM
31	Near–UV	NUV
32	Numerical Aperture	N.A.
33	Photoluminescence	PL
34	Physical Vapor Deposition	PVD
35	Piezoelectric	PE
36	Piezo–response Force Microscopy	PFM
37	Plasma–Assisted Molecular Beam Epitaxy	PAMBE
38	Power Density	PD
39	Quantum Well	QW
40	Radio Frequency	RF
41	Reflection High Energy Electron Diffraction	RHEED
42	Resonance Raman Spectra	RRS
43	Scanning Near–field Optical Microscopy	SNOM
44	Scanning Probe Microscopy	SPM
45	Scanning Transmission Electron Microscope	STEM
46	Secondary Electrons	SE
47	Selected Area Electron Diffraction	SAED
48	Spontaneous Polarization	SP
49	Superlattice	SL
50	Surface Optical	SO
51	Surface Plasmon	SP

52	Surface Plasmon Polaritons	SPP
53	Surface Plasmon Resonance	SPR
54	Transmission Electron Microscopy	TEM
55	Transverse Optical	TO
56	Vapor–Liquid–Solid	VLS
57	Vapor–Solid	VS
58	Ultraviolet	UV
59	Whispering Gallery Modes	WGM
60	X–ray Photoelectron Spectroscopy	XPS

CHAPTER 1

INTRODUCTION

“*We keep moving forward, opening new doors, and doing new things, because we're curious and curiosity keeps leading us down new paths*” ....Walt Disney

1.1 Group III nitrides

The research towards direct band gap group III nitride semiconductor materials and its alloys are very important because of its applications in blue to near–ultraviolet (UV) light emitting devices (LEDs) and laser diodes (LDs).[1-6] The main attractive material properties of them are enormous physical hardness, high thermal conductivity, elevated melting temperature and extremely large hetero–junction offsets.[1-6] Group III nitrides are one of the most promising candidates for fabricating the short wavelength and high frequency optical devices.[1-4,6-8] The variation in atomic percentage of the constituent elements in the alloy compositions allow us to tune the direct band gap of III–nitrides with an energy range of ~0.70 to 6.20 eV. InN, GaN, and AlN along with its ternary (InGaN and AlGaN) and quaternary (InAlGaN) alloys are the well–known candidates for major optoelectronic applications.[1-4,6-10] The prominent candidate for this wide band gap material is ternary alloy of $Al_xGa_{1-x}N$ system with the tunable band gap from ~3.40 to 6.20 eV and is also an ideal candidate for the fabrication of optoelectronic devices.[1-8] However, high crystalline and optical quality are essential for the various optoelectronic applications.[2,6,8] The high–quality GaN and AlGaN micro–crystallites are already used for demonstrating room temperature continuous wave lasing action *via* high–Q whispering gallery modes (WGM) which are applicable for LDs. The presence of WGMs in the microrods is a signature of excellent morphological, structural, and high optical quality of the material.[11-14] Vertically aligned microrods are attractive for LEDs for its applications in manufacturing coaxial quantum well (QW) structures.[15-17] Apart from the tunable band gap, the III–nitrides are well–known for its potential applications in high–performance, high–power optoelectronic devices because of their high carrier mobility, high electrical breakdown voltage, high melting point and low chemical reactivity.[2,6,8] Moreover, the group III nitrides are the key factor for the major revolutionary changes occurred in lighting, display technology, data storage and power switching. Furthermore, the engineering of band gap allow them also to use for photovoltaic, water splitting, hydrogen storage, gas sensing and field emissions.[2,15-23] As a result of the above mentioned applications, the families of III–nitride were recognized with the Nobel prize (2014).

1.1.1 Crystal structure

The group III nitrides are generally found as in the form a thermodynamically stable wurtzite structure with a hexagonal symmetry (Fig 1.1a). The wurtzite structure has lattice constants, *c* and *a*, with two formula units in the primitive cell *i.e.*, four atoms per primitive cell.

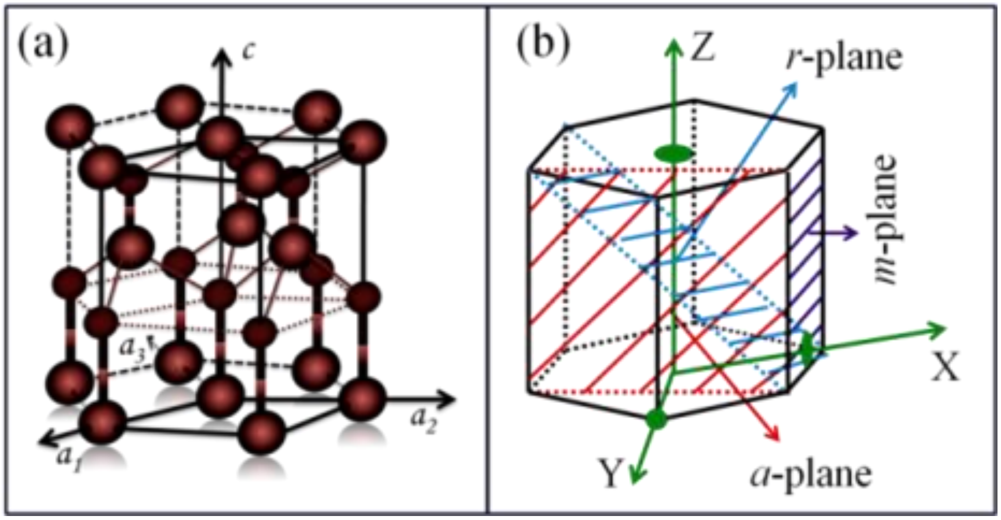

Figure 1.1 (a) Schematic sketch of the wurtzite crystal structure and (b) its different crystallographic planes.

The point group symmetry is denoted as 6*mm* in the Hermann–Mauguin and C_{6v} in the Schoenflies notations. The space group for the wurtzite structure is represented $P6_3mc$ in the Hermann–Mauguin and C_{6v}^4 in the Schoenflies notations. The wurtzite structure consists of two interpenetrating hexagonal close–packed (*hcp*) sub–lattices with an offset along the *c*–axis by 5/8 of the cell height (5*c*/8).[24-26]

The schematic sketch shows the wurtzite crystal structure (Fig. 1.1a) as well as the atomic planes (Fig. 1.1b) along the six–fold symmetry axis coincide with the [0001] direction. The crystal structure is constructed by the successive stacking of planes and each plane contain only either cations with positive (+ve) charges or anions with negative (−ve) charges, known as ABABAB… stacking. The center of gravity of cations and anions in the consecutive planes are not overlapped completely which leads to develop an electric dipole along the *c*–direction. In other words, the geometric center of the −ve charges (electron cloud) in the lattices of the solid does not coincide exactly with the geometric center for the +ve charges (nuclei).[24-26] Consequently, it creates an inherent spontaneous polarization (P^{SP}) to the wurtzite crystals. This effect is also called the pyroelectric effect because the magnitude of P^{SP} may change with respect to the temperature of the crystal, which induces the proportional changes in the c/a ratio. For pyroelectric materials, P^{SP} is always oriented along the low symmetry axis of the crystal called as pyroelectric axis. In the case of the wurtzite crystals the pyroelectric axis is parallel to the [0001] direction.[24-27]

1.1.2 Non−centrosymmetric: Spontaneous and piezoelectric polarizations

Group III nitride semiconductors show a well–defined polarization effect due to the lack of a center of inversion symmetry and exhibit piezoelectric effects by the application of strain to the lattice system. Generally, the piezoelectric effect is observed because of strain originated by two ways. The first one is due to the lattice mismatched strain between the samples and the substrate or the epitaxial layers. The second reason for the origin of strain is due to the difference in thermal expansion coefficient between the sample specimen and the substrate or the epitaxial layers. The presence of these strains can induce an additional polarization to the crystal which is known as piezoelectric polarization (P^{PZ}).[24-27] Moreover, as mentioned earlier; there exist a non–vanishing P^{SP} along the *c*–axis of an ideal wurtzite structure. Therefore, the total polarization experienced by the wurtzite crystal is the sum of the P^{SP} and P^{PZ}, which depends on the constituent elements (composition) present in the system as well as the strain. Moreover, the non–centrosymmetric structure of wurtzite III–nitrides results in intrinsic non–linear and anisotropic optical properties. The anisotropy results in uniaxial birefringence which can be observed due to the presence of two different refractive indices for polarizations parallel and perpendicular to the *c*–axis.[24-27]

In general, piezoelectricity is a phenomenon in which an electric field is generated inside a material subjected to a mechanical strain or vice versa.[26-31] Consequently, this strained material behaves like a charged capacitor with an electrostatic potential across it, which can be utilized for several applications.[28-31] It implies that the piezoelectric effect can be employed to convert mechanical energy into electrical energy also. Therefore, in addition to their utility as optical material, because of the presence of piezoelectricity in the III–nitrides establishes their importance, particularly in different micro–mechanical devices such as micro–actuators, micro–sensors, ultrasonic motors, micro–pumps, self–powered devices, electro–mechanical sensing, mechanical energy harvesting and other various applications as MEMS based device.[28-32] The performances of such devices are dependent on both the crystalline as well as the electronic properties of the material. It is reported that the III–nitrides grown along the *c*–axis [0001] with polar orientation lead to a huge amount of intrinsic electric field, which degrades the efficiency of LEDs.[26-32] The presence of these internal electric fields cause the separation of electron (e^-) and hole (h) wave function (quantum confined Stark effect), which reduces the rate of radiative recombination leading to the reduction in the quantum efficiency and hence the performance of optoelectronic devices. This is the origin for the interest in the growth of III–nitride crystals as well as the device manufacturing along the non–polar orientations of the wurtzite structure, which do not possess the internal electric fields and hence the efficiency of LEDs is expected to be improved.[24-27] Therefore, the crystallographic non–polar planes of *m*–plane (1-100) and *a*–plane (11-20) are more favorable for device making compared to that of polar *c*–plane (0001) as shown in the figure 1.1b. The studies included in the Chapter 3 of the thesis contain the catalytic assisted growth of AlGaN nanostructures along the non–polar *m*–plane (1-100) as well as the self catalytic growth of AlGaN crystallites along *c*–plane. In addition to that, the electromechanical coupling characteristics of various ferroelectric and piezoelectric materials can be studied using piezo–response force microscopy (PFM).[31,32] Therefore, the behavior of this intrinsic electric field to the external bias voltage is understood with the PFM studies of hexagonal AlGaN micro–rods which is included in the Chapter 4 of the present thesis.

1.1.3 Physico–chemical properties: III–nitrides

The group III nitride semiconductors are intrinsically *n*–type in nature due to the non–stoichiometry created by the N vacancies (V_N). High chemical stability, significant hardness, and wide band gap energy allow them to be an excellent candidate for device operation at high temperatures and caustic environments. The major physico–chemical properties of GaN, InN and AlN are compared with each other and tabulated (Table 1.1).[24-27]

Table 1.1: Comparison between the basic physico–chemical properties of wurtzite group III nitrides

Property	**GaN**	**InN**	**AlN**
Lattice parameters; a (Å)	3.188	3.539	3.110
c (Å)	5.185	5.708	4.980
c/a	1.627	1.613	1.610
Energy gap (eV) (at 0 K)	3.51	0.7	6.25
Exciton binding energy (meV)	23	9	57
Density (g.cm^{-3})	3.255	6.095	6.18
Exciton Bohr radius (nm)	2.4	8	1.4
Breakdown field (MV.cm^{-1}) (at 300 K)	3.0	2.0	1.8
Electron mobility (cm^{2}.V^{-1}.s^{-1}) (at 300 K)	1,400	4,000	--
Thermal conductivity (W.cm^{-1}.K^{-1}) (at 300 K)	2.3	0.8	2.9
Relative dielectric constant, (ε_r)	8.9	15	8.5
Spontaneous polarization; P^{SP} (C.m^{-2})	-0.0339	-0.0413	-0.0898
Piezolectric coefficients; d_{33} (pm. V^{-1})	1.9	7.6	5.4
d_{13} (pm. V^{-1})	-1.0	-3.5	-2.1
d_{15} (pm. V^{-1})	3.1	5.5	3.6
Refractive index (n)	2.7 for 353 nm	2.56 for 1 μm	2.58 for 220 nm

The Raman spectroscopy is used as the major characterization tool in the present thesis. Therefore, it is customary to understand the basic vibrational properties of the group III nitrides. In the case of hexagonal lattice structure, group theory predicts eight sets of phonon normal modes at the Γ point of the Brillouin zone center, $\Gamma_{acoustic}+\Gamma_{optical}$ =

$(A_1+E_1)+(A_1+2B_1+E_1+2E_2)$ (Schematic, Fig.1.2). Among them, one set of A_1 and E_1 are acoustic phonon modes, while the other remaining six modes, namely $A_1+E_1+2B_1+2E_2$, are the optical phonon modes. Because of the above mentioned polar nature of wurtzite crystal, the A_1 and E_1 modes split into longitudinal optical (A_1(LO) and E_1(LO)) modes implying that they are beating along the *c*–axis, and transverse optical (A_1(TO) and E_1(TO)) modes meaning that they are beating perpendicular to the *c*–axis (along the basal plane).

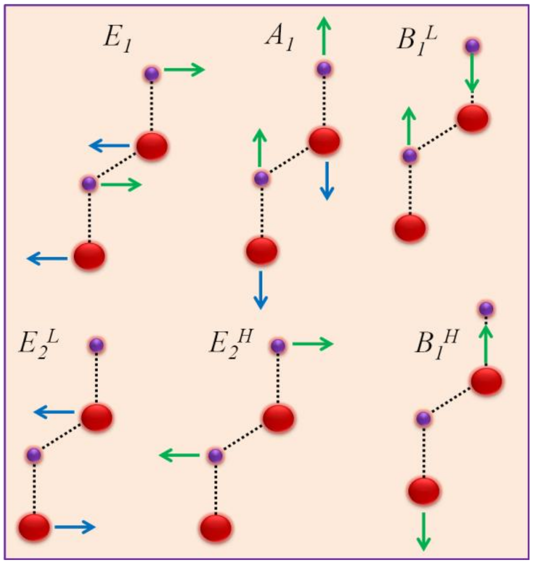

Figure 1.2 The schematic sketch of different vibrational modes for wurtzite III–nitride structures.

Generally, the A_1 and B_1 modes represent the atomic vibrations beating along the *c*–axis, whereas the other modes, E_1 and E_2, signify atomic vibrations on the basal plane. The A_1 and E_1 modes are found to be both Raman and IR active, whereas the two E_2 modes are only Raman active. The two B_1 modes are neither Raman nor IR active, therefore they are named as silent modes. The details of the typical energy values in the spectroscopic units of cm^{-1} for different Raman phonon modes reported for the group III nitride members are tabulated (Table 1.2).[25-27,33,34]

Table 1.2: Typical values of Raman shift for zone center phonons of group III nitride semiconductors

Raman shift (cm^{-1})	**GaN**	**InN**	**AlN**
E_2(low) or E_2^L	144	87	248
A_1(TO)	533	447	614
E_1(TO)	558	472	672
E_2 (high) or E_2^H	569	488	660
A_1(LO)	734	588	894
E_1 (LO)	742	593	917
B_1(low) or B_1^L	334	225	547
B_1(high) or B_1^H	690	576	719

1.1.4 Aluminium gallium nitride

The ternary alloys of wurtzite $Al_xGa_{1-x}N$ form a continuous alloy system in accordance with the constituent elements present in it and generate a wide range of band gap with respect to the small changes in the lattice constants. The compositional dependence of the principal band gap of $Al_xGa_{1-x}N$ can be calculated from the following empirical expression: $E_g(x) = xE_g(AlN) + (1-x)E_g(GaN) - bx(1-x)$; where E_g(GaN) and E_g(AlN) are the known band gap values of GaN and AlN, respectively; x is the Al molar fraction, and b is the bowing parameter.[25-27] The ternary alloy of $In_xGa_{1-x}N$ nanowires (NWs) were grown with a tunable band gap in the range of 1.1–3.4 eV, showing the emission from the near–IR to the blue/violet region.[1-5,25-27] In order to attain the applications in wide electromagnetic (*em*) spectral region, it is necessary to cover the wavelength ranges again from near–UV to deep–UV region. The prominent candidate for covering the UV and the deep–UV region is the ternary alloy of $Al_xGa_{1-x}N$ with a wide and a tunable band gap range of 3.4–6.2 eV.[5-10,25-27] However, for making such optoelectronic devices operating at short UV wavelengths, alloy compositions with greater Al content are required. The properties of these materials lie on the border between conventional semiconductors and insulators, which adds an additional degree of complexity for the growth and device manufacturing.[5-10,25-27] In the present study, we report a simple technique of atmospheric pressure chemical vapor deposition (APCVD) for synthesizing AlGaN NWs in the catalyst assisted vapor–liquid–solid (VLS) process. We mainly focus in to the synthesis of AlGaN NWs of different size and shapes as reported in the Chapter 3 of the present dissertation.

As per the discussion included in the above section 1.1.2 the crystalline orientation dependent characterizations and analysis of crystallites are very important. In the context of understanding the crystalline orientation dependent properties of the cystallites, the Raman spectroscopy is not only a very efficient non–destructive characterization tool for the phase confirmation of the sample, but also the fact that the polarized Raman spectrum is capable to investigate the crystallographic orientation in agreement with the selection rules.[25,36-39] There are several reports available for polarized as well as angular dependent polarized Raman studies collected from a single spot on material.[25,36-39] However, the polarized Raman studies alone may not be sufficient to understand crystalline nature of the crystallites. Thus the polarized Raman imaging corresponding to the peak intensities of allowed vibrational modes throughout different crystal planes, may help us to predict the crystalline nature of the material. We report, the polarized Raman spectra of a single AlGaN sub–micron sized hexagonal crystallite for two different crystallographic orientations in the far–field configuration in the Chapter 4 of the thesis. There are only few reports available for the crystalline orientation dependent photoluminescence (PL) studies of group III nitrides, which show the variations in optical properties with respect to the orientations of crystallographic planes without any physical insight.[40,41] The present investigations include the crystal orientation dependent polarized PL studies to understand and elucidate the effect of crystalline orientation on the optical properties of the AlGaN crystallite as described in the Chapter 4.

1.2 Optical properties of group III nitride nanostructures

The *n*– and *p*– type doping in nanostructures and its hetero–structures have enabled the scientific community to tailor the properties of nanostructures for different photonic and optoelectronic device based applications. The major types of these applications include LEDs, photovoltaic cells, high electron mobility transistor (HEMT) and photo–detectors. The tailoring and arrangements of 1D nanostructures strongly influence the optical properties, which are explicitly related to the efficiency and the performance of the photonic device. In general, the optical characterization of semiconductor nanostructures is described as the study of the interaction between materials with the photon of the *em* radiations. The light–matter interaction can occur in different ways, such as absorption, reflection, transmission, refraction, luminescence, elastic and inelastic scattering as shown in the schematic sketch (Fig. 1.3).[42,43] The physical dimensions of the nanostructures show significant contributions to the optical properties when their size in any direction is comparable to the de Broglie wavelength of e^{-}s or comparable with the exciton Bohr radius.

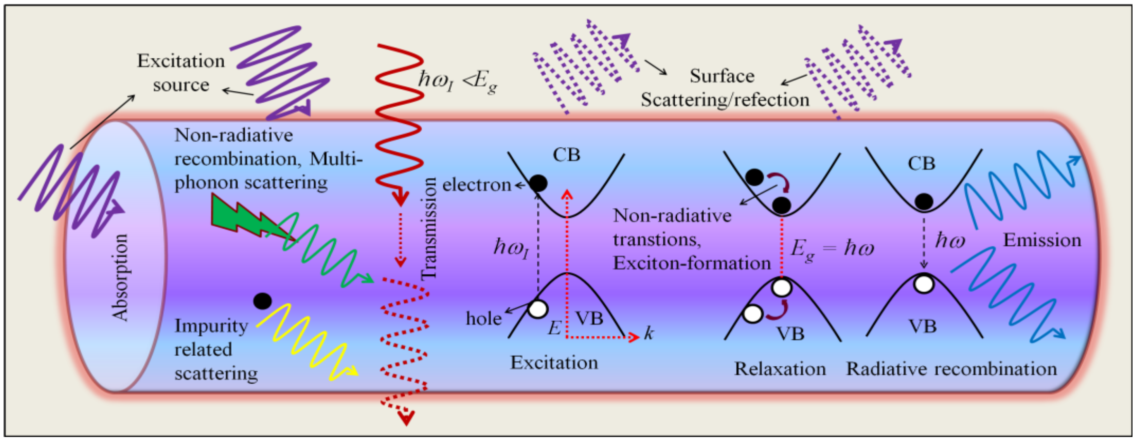

Figure 1.3 The schematic sketch for the light–matter interaction for the semiconductor nanostructures.

The constraints (confinement) can originate from one (1D), two (2D), and three (3D) dimensions of the nanostructures.[44,45]

1.2.1 One dimensional (Nanowires, Nanorods)

The NWs are 1D structure with diameters in the nanometer scale and lengths ranging from several hundreds of nanometers to a few numbers of micrometers. Owing to their nanoscale dimensions in the radial direction; they exhibit the bidirectional confinement effects and unidirectional transport properties that can generate novel optoelectronic properties as compared to that of the bulk materials.[44,45] The 1D geometry of NWs provides an extremely high surface area with a nanoscale radius of curvature.[42] Furthermore, it also provides anisotropic properties with respect to the light–matter interactions along the radial and axial directions, which is an interesting topic from the point of view of nano–science and technology.[46-48] The NW length can be up to several micrometer scales, makes them easy to give electrical connectivity and manipulations for device fabrication. In addition to the unique aspects of their physical, chemical, and mechanical properties, the NWs can be used to handle light on a nanometer scale and thus can be used as building blocks for advanced nano–

optoelectronics.[1-5,42] The properties of light handling and manipulations at nanoscale regime mainly include Fabry–Perot mode stimulated emission, wave guiding of photons, random lasing action, highly efficient luminescence, and extremely sensitive photo–detection and so on.[42] The concept of light manipulations at nanoscale are used in the development of many advanced NW–based optoelectronic devices including LEDs, lasers, optical sensors, photo diodes, and photovoltaic cells.[1-5,42] In addition to that, the major advantage of 1D geometry of NWs is the reduction of defect density such as threading and screw dislocations, generated by the lattice and thermal mismatching with substrates or epitaxial layers.[25-27] Scientific researchers developed various 1D nanostructures such as nanotubes, NWs, and nanocones for the III–nitrdes.[1-5] The optical properties of NWs can be influenced by its physical and chemical states. Furthermore, the length and diameter of NWs as well as their alignment also affect the emission and absorption properties.[42] In addition to that, the composition, impurity or doping level, defect concentration, crystal structure, growth direction, and nature of the facets are also critical to the spontaneous emission and/or stimulated emission and absorption.[42,45,49] The study of the optical properties of an ensemble of NWs (Chapter 3) as well as diffraction limited single NW (Chapter 6) is also included in the present dissertation.

1.2.2 Two dimensional (Thin films, Quantum wells)

The QWs are the 2D structures with a thickness in the nanometer scale. Similarly, the QWs may exhibit the unidirectional confinement effects and bidirectional transport properties those can be applicable in the various optoelectronic properties.[44,45] An analogue to the crystallography, the superlattice (SL) is termed as a 'lattice of lattices'. Thus, any regular pattern or sequence of semiconductor layered hetero–structures can be considered as a SL. A QW is a hetero–structure of two or more semiconductor material in which one thin 'well' layer is sandwiched by two other ‘barrier’ layers. Consequently, the difference in electronic configurations in the semiconductor materials generates a finite ‘potential well’ in which charge carriers posses discrete energy levels instead of a continuum, as compared to that of the bulk. If the SL possesses a significant wave function penetration between the adjacent wells due to the tunnelling effects, then the structure is called as a multi–QW (MQW).[49-52] Similarly, an analogous to the ‘bands’ in the crystal structure, if the QWs are arranged very close to each other with a thickness of the order of a few nanometers, then the significant wave function penetration between the QWs may lead to the creation of overlapping states representing the allowed continuum called as ‘mini–bands’ in the SL structures and are used for current conduction in 2D. A few number of mini–bands generated in the SL injection regions are forbidden for e^- occupancy and are called ‘mini–gaps’.[49-52]

Generally, the *c*–plane oriented AlGaN/GaN or AlGaN/AlN hetero–structures create some fixed charges at the hetero–interfaces due to discontinuities of P^{SP} and P^{PZ} between consecutive layers. The presence of sheet charges behaves as a 2D electron gas (2DEG) when the AlGaN layer has suitable thickness. In the case of electronic devices, the polarization effects are beneficial as they give rise to 2DEG sheet charges. The typical value of the e^- concentration in the 2DEG is of the order of 10^{13} cm^{-2} for the commonly used $Al_{0.30}Ga_{0.70}N$/GaN HEMT structures and hetero–junction field effect transistors.[25] In contrast, for MQW based LEDs, the fixed sheet charges at the hetero–interfaces produce high intrinsic electric fields (order of ~1 MV.cm^{-1}) and deteriorates its quantum efficiency and performance. The SLs and MQWs of AlGaN/GaN with different Al percentages are used as active region, buffer layers, carrier confining and electron blocking layers (EBL) to improve the internal and external quantum efficiency of blue, UV and deep–UV LEDs and LDs.[1-5,25]

1.2.3 The surface and interface optical phonon modes

The remarkable scope of applications and importance of group III nitrides, as mentioned earlier, motivated the researchers to establish almost all the characteristic features of these materials including the detailed study of the phonon modes. The reduction of size in the materials up to nanometre scale reduces the degrees of freedom for phonons leading to the spatial confinement of the bulk phonon modes.[44,45] It may also change significantly the density of phonon states, responsible for the origin of surface and interface (IF) related phonon modes.[52-54] The frequency of such surface lattice vibrations are found in between the transverse optical ($TO_{q=0}$) and longitudinal optical ($LO_{q=0}$) phonon modes observed at Brillouin zone center (wave vector, $q=0$).[52-54] The vibration of surface atoms, with amplitudes confined near to the surface, decrease exponentially with depth and is named as surface optical (SO) phonon modes,[52-54] also known as Fröhlich modes.[55] The effect of surface–modulation–assisted e^-–phonon scattering is recommended for the major appearance of SO phonon modes.[53-59] The SO modes are observed because of the breakdown of translational symmetry of the surface potential due to the surface roughness or creation of periodic structures. Similarly, the IF modes are observed owing to the formation of grating in the surface of nanostructures.[53-59] The breakdown of translational symmetry of surface potential corresponding to the periodicity leads to an additional crystal momentum that allows the generation of some phonon modes away from zone centre (non–zone centre, $q\neq0$). The identification of such SO phonon mode is difficult to be detected in the case of bulk materials because of the constraint in the conservation of momentum due to their perfect crystalline symmetry.[53-59] Therefore, the nanorods (NRs) with surface perturbations may increase in the intensity of SO mode frequency compared to that of the bulk crystals.[53-59] It is also well reported that, the SO phonon mode frequency depends on the dielectric constant of the surrounding medium (ε_m) as well as the shape, size, periodicity of saw tooth edges, density and diameter modulation of the nanostructures.[53-60] In the Chapter 5, we report the Raman spectroscopic investigation of the SO phonon modes in 1D $Al_{0.97}Ga_{0.03}N$ NRs using surrounding medium of different dielectric constants. The SO phonon mode frequencies are calculated from the theoretically simulated dispersion curve of $Al_{0.97}Ga_{0.03}N$ NRs in the presence of different dielectric media of air and CCl_4 to match with the experimentally observed $q \neq 0$ phonon modes in the Raman spectra. The Fourier component of the surface potential, responsible for the formation of SO modes, are accounted due to the presence of periodic surface modulations due to the presence of sharp edges at the corners of well–faceted 1D $Al_{0.97}Ga_{0.03}N$ hexagonal crystallites along with an array of row and column arrangement of NRs in the sample.

Similarly, the approximation of negligible crystal–momentum transfer for the backscattered waves, as in the case of bulk crystal, may not be true for certain phonon modes of SLs or MQWs with a larger periodicity. Moreover, the semiconductor SLs, single–QW structures, and MQWs are famous 2D systems because of the confinement of phonons and charge carriers within a plane where the degree of phonon confinement is 1D, as the confinement is restricted along one direction which is perpendicular to the SL plane.[44,45,50 52,61,62] However, the behavior of the different optical phonon modes at the interface of MQW structures and SLs are very exciting and speculating topic for the current scientific research area of group III nitride polar wurtzite structures. Owing to the boundary conditions for the optical modes in the MQWs and the nature of parallel and perpendicular component of frequency dependent dielectric constants in the quantum confined layers, the solutions of

Maxwell equations can take different mathematical functional forms leading to four types of optical phonon modes, namely, confined modes, IF modes, propagating modes and half–space modes.[61,62] The e^- confinement in the MQW structures also can influence the structural and optical properties of the materials.[44,45] The additional momenta generated for creating non–zone centre interface optical (IO) phonons can be absorbed by the periodic structure of the lattices in terms of quantized units of $2\pi/\lambda$, where λ is the periodicity of the SLs or MQWs.[53,63-65] Therefore, the nanomaterials such as 1D NWs, 2D MQWs and SLs with a large surface area contribute significantly towards the SO or IO phonon signal as compared to that for the bulk crystals.[63-65] In the Chapter 5, we also investigated the behavior of IO phonon modes in the Raman spectra of $[AlN/GaN]_{20}$ and $[Al_{0.35}Ga_{0.65}N/Al_{0.55}Ga_{0.45}N]_{20}$ MQW structures originating from the breakdown of translational symmetry of the surface potential because of the presence of multiple periodic structures and IFs of MQWs. The q value was calculated in accordance with the wavelength (λ) originated from the periodicity of MQWs for the IO phonons and the corresponding required edge lengths (L) of 2D plates were investigated using a theoretical simulation of the dispersion relation in the 2D MQW structures. We also studied the change in IO phonon frequency in the observed spectra with respect to the difference in dielectric constant of the surrounding medium for MQWs and bi–layer thin film.

1.3 Light–matter interactions in the sub–diffraction regime

1.3.1 Spontaneous and stimulated emissions of nanostructures

A photon can be absorbed by a valence e^-, which then gets excited into the CB by leaving a hole (h) in the VB in a process termed as absorption (Fig. 1.4a). Statistically e^-s in excited states has a natural tendency to de–excite and lose their excess energy. Thus the natural emission of a photon by means of the de–excitation of the system is known as the spontaneous process. The corresponding emission of *em* radiation of light therefore called spontaneous emission (Fig. 1.4b). In contrary, in the case of an absorption process, the e^-s are promoted to an excited state by absorbing a photon with a quantum of specific energy. It is not a spontaneous process, as an e^- cannot jump to the excited state without the existence of an external stimulus. The process of PL involves the absorption of incident photons which results in the generation of an e^-–h pair and the emission of a photon with different energy after the recombination of the e^-–h pair. The incident photons excite the e^-s from the VB to the CB by obeying the conservation of total energy and momentum (with negligible photon momentum compared to that of e^-s).[42,45]

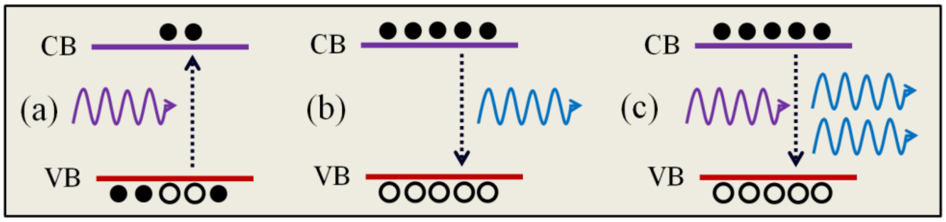

Figure 1.4 Schematic diagram of (a) stimulated absorption, (b) spontaneous emission, and (c) stimulated emission in a semiconductor.

The recombination processes which yield the emission of photons are termed as radiative recombination. If this process occurs without the aid of any other *em* field density, then it is called spontaneous emission (Fig. 1.4b) or in other words, the transition probability of spontaneous emission does not depend on the presence of other photons. In contrary, if the e^-–h pairs are recombined to produce a photon emission in the presence of an additional *em* field density of a suitable frequency, then it is termed as stimulated emission (Fig. 1.4c) in which the frequency, polarization, phase, energy and direction of propagation are consistent with the stimulating photon. Therefore, the intensity of stimulated emission is proportional to the electric field strength and photon population or in other words, the transition probability of stimulated emission depends on the presence of other photons with the same energy. The photon generated through stimulated emission goes on to amplify the *em* wave up to the external pump source exist. If a recombination process that does not produce photons is termed non–radiative recombination, in which the energy is exchanged with the lattice in the form of heat through phonon emissions. Stimulated emission is the basis of laser operation, as the name 'laser' implies the "light amplification by stimulated emission of radiation".[42,49] The stimulated emission occurs only in the presence of high photon densities needed for lasing action cannot be maintained easily except in a waveguide cavity. Single–NW lasing action is similar to that of a conventional Fabry–Perot cavity lasing except the cavity length of NW is in the order of a few micrometer scales. The coupling efficiency of spontaneous emission of NW and hence the light amplification of NWs depend on the size, shape, diameter, and its different facet reflectivity. In general, the geometrical shapes suitable for the optical amplification in the single–NW are hexagonal, triangular, or rectangular cross–sectional areas. The particular shape of the NWs support to exhibit a specific set of sustainable guided modes inside the NWs which may help for the optical amplifications.[42,49]

The criteria to attain the optical amplification by means of stimulated emission leading to lasing action from the NWs are;[42]

i. The total output intensity of the emission spectra with respect to the external pump power would show a superlinear increase above a threshold

ii. The probability of the observation of sharp lasing peaks in the emission spectra above the threshold

iii. The observation of the linear dependence of Δυ (mode spacing, the difference in frequencies between the two adjacent modes) with 1/*l* (length of the NW)

iv. The observation of the diffraction patterns showing coherence interference of light from the end facets of the NWs

The 'random laser action' is the amplification of multiple scattering photons inside a mirrorless disordered medium. It is reported that an assembled NWs can able to produce a considerable amount of optical amplifications with a sufficient excitation power.[42] Therefore, in the case of a random laser there is no restriction for the well defined facets for the sustainable optical feedback. Furthermore, the optical amplification and lasing characteristics of an ensemble of NWs is also dependent on the refractive index of the surrounding media, dimensions and density of NWs.[42]

1.3.2 Photonic confinement

Imaging a nanostructure or focusing to a dimension in the sub–wavelength limit, using the diffraction limited optical technique is a major achievement in recent times. The nanoscale imaging in the sub–wavelength limit was boosted with the application of plasmonics.[66-70] Surface plasmon resonance (SPR), originating from the coherent oscillation of conduction e^-s of noble metal nanostructures, excited by visible light, facilitates propagation of surface plasmon polaritons (SPP) along metal–dielectric interface.[66-70] The evanescent waves near to the metal–dielectric interface assist the imaging or focusing of nanostructures in the sub–diffraction length scale.[66-70] The rate of interaction of a light emitting material with *em* radiation can also be enhanced by keeping it in a micro–cavity. The spontaneous emission rate is not only a material characteristic but also depends on the photon density (energy density of the fluctuating *em* field) in the surrounding environment. The long lived interactive photons, enhances the photon density leading to increase in emission/absorption of light in the process of Purcell enhancement.[71-74] Tightly confined light or trapped photons in between two semiconductor or dielectric media with sizes comparable to the wavelength of the confined light, increases photon density leading to the enhanced light–matter interaction, enabling a range of non–linear applications.[46-48,75-79]

Two different types of optical feedback mechanism are reported for the optical amplifications, one is coherent and the other one is incoherent feedback. The main difference between them is that the coherent optical feedback preserves the phase information of the scattered light whereas it is not preserved by the incoherent feedback mechanism. In the case of coherent feedback mechanism, the scattered light returns to its original position through a closed–loop path of light by means of several multiple scattering inside a random medium. The stimulated emission is a coherent quantum mechanical effect and hence the photons emitted are in phase with the photons that induce the transitions.[42] It is possible to observe a coherent random lasing from the high–density randomly assembled NWs because of the strong 3D optical confinement. Whereas, in the case of vertically aligned NWs may possess only 2D confinement of optical modes. Therefore, in the case of randomly assembled NWs the overall scattering strength is higher than that of the vertically aligned NW arrays, leading to better optical amplifications.[42] In the Chapter 6, we report the far–field spectroscopic PL imaging of a single semiconductor AlGaN NW using the peak intensity of free excitonic (FE) emission in the sub–wavelength scale. The PL emission intensity from a single NW is observed to be strongly influenced by the proximity of other NWs; even though the separation between the NWs is more than the excitation laser beam diameter. In case of the optical confinement effect, a non–zero non–equilibrium population of long lived photons is envisaged to influence the increased PL emission intensity from the single NW.

Since the size and shape of the NWs affect the polarization anisotropy of optical absorption and emission spectra,[46-48,80] the polarized Raman scattering is known to be one of the most prominent local probes for understanding the lattice dynamics of the crystalline system and its crystallographic anisotropy.[81,82] Raman spectroscopy, as an optical characterization tool with extremely weak scattering cross section, is not a popular technique to analyze scattered signal from a nanostructure with a dimension below the sub–diffraction limit. In this regard, plasmonic assisted characterization tools, namely, surface and tip enhanced Raman spectroscopy are the only relevant tools in the spectroscopic studies of nano–scale objects in the sub–diffraction limit. In a far–field optical configuration, we report the polarized resonance Raman spectra (RRS) of a single AlGaN NW of diameter ~100 nm, using a monochromatic light source with a wavelength (λ) of 325 nm using a near–UV objective of magnification 40X having a numerical aperture (N.A.) of 0.50. As per the Abbe's diffraction limit (λ/2N.A.), thus it is not possible to focus an object below ~325 nm in the above mentioned optical configuration. The optical confinement of polarized light, which may enhance the light–matter interaction between two semiconductor or dielectric media along with strong e^-–phonon coupling in the polarized RRS are proposed to understand the crystallographic orientations in the sub–diffraction length scale. The Raman studies of a single NW in the sub–diffraction limit using confinement of polarized light are also presented in the Chapter 6.

1.3.3 Plasmonic confinement of light

A plasma system in metal consists of a fixed lattice of +ve ions coexisting with a gas of free e^-s, which exactly cancels the charge of the ions. The +ve ions at the lattice site will exert a restoring force to oppose the displacement of the e^- cloud. As a result, the whole e^- gas oscillates back and forth with respect to the fixed +ve ions. These oscillations are called 'plasma oscillations'. Quantized unit of plasma oscillations are called as 'plasmons'.[44,63-65] The light–matter interaction in metallic nanostructures have opened to a new branch of surface plasmon (SP) based photonics, called plasmonics.[44,63-65] The SPs are originated due to the collective oscillation of the free e^-s at a frequency equal to the frequency of quantized harmonic oscillation of e^-s, ω_p $(=(n_e e^2/m_{eff}\varepsilon_0)^{½}$, where, n_e is the carrier density, m_{eff} is the effective mass, e is the charge of an e^- and ε_0 is the permittivity of free space) about the fixed +ve charge centers at the surface of metal nanostructures.[83-86] The coupling of the incident *em* waves to the coherent oscillation of free e^- plasma near the metal surface is known as SPP and it is a propagating surface wave at the continuous metal–dielectric interface.[83-86] The *em* field perpendicular to the metal surface decays exponentially and is known as evanescent waves providing sub–wavelength confinement near to the metal surface. Matching of the incident excitation frequency (ω) of *em* wave with the plasmon frequency (ω_p) of the e^-s in metal nanostructures, leads to an enhanced light–matter interaction, known as SPR.[83-86] In the Chapter 6, we also studied the light–matter interaction of an isolated metallic Au nanoparticles (NP; diameter ~10–150 nm) in the near–field regime by using the near–field scanning optical microscopy (NSOM) technique with a laser excitation of 532 nm.

1.3.4 Light at near–field regime

The light–matter interaction at the near–field regime in the vicinity of nanostructures is a very interesting as well as challenging task in the scientific community. The Abbe's diffraction limit prevents conventional optical microscopes to possess a spatial resolution beyond the value of ~λ/2, with a maximum N.A. value of unity for the probing objective.[87] Thus, even for the visible light of λ=400 nm cannot image nanostructures of size below 200 nm. The NSOM assisted with the help of plasmonics is a unique tool to understand the light–matter interaction in the near–field regime for optical imaging of nanostructures in the sub–diffraction limit.[87-90] The light passing through the metal coated tip of NSOM probe with a circular aperture of a few nanometers at the apex is capable of surpassing the diffraction limit. In the near–field regime, the confined light with evanescent field components emanating from the NSOM probe with higher momenta *i.e.*, lower wavelength and velocity compared to that of the normal light is not diffraction limited. Hence, it facilitates optical and spectroscopic imaging of objects with nanometer scale spatial resolution.[87-90]

The properties of nanostructure are quite sensitive due to its large surface to volume ratio. Even though, the semiconductor NWs can be synthesized as single crystals, the NWs may still contain many defects such as impurity atoms and surface states. Furthermore, it is very difficult to understand the native defect states are distributed all over the NWs uniformly or not. If the defect distribution is not homogeneous, the localized physical and optoelectronic properties would be modified. Since the NW dimension is in the sub–diffraction limit, the inhomogeneity must be investigated by a characterizing technique, which is able to record the signals with a high spatial resolution. Near–field probes, specially designed for luminescence characterization are suitable for the research on inhomogeneity in a single 1D semiconductor

NWs. The NSOM is such a local probe technique based on optical excitation. In NSOM, the diffraction limit can be overcome by proximal excitation. When the excitation light source is very close to the sample surface, the diffraction limit is not established due to the formation of near–field evanescent waves.[42,91-93] In order to generate the evanescent waves at near–field regime, the incident light is generally guided to a position very close (order of few nanometers) to the sample surface by using an optical fiber with a sub–wavelength sized aperture. For an apertured–NSOM, the spatial resolution is determined by the size and geometry of the aperture, not by the excitation wavelength. In NSOM, since the incident light strongly interacts with the local region of the sample, there is the strong dependence of luminescence intensity on aperture–to–sample distance.[42,91-93] By considering the importance of AlGaN nanostructure in the optoelectronic applications as well as semiconductor industries, it is also very important to understand the interaction of the AlGaN NW with the visible light. We also studied the light–matter interaction of an isolated single AlGaN NW (diameter ~120 nm) grown *via* VLS mechanism along with metallic Au NP catalysts (diameter ~10–150 nm) in the near–field regime by using the NSOM technique with a laser excitation of 532 nm, which is included in the Chapter 6. In order to understand the light–matter interaction of AlGaN NW, we invoked the semiconductor band picture by analysing the different energy states related to native defects with the help of PL measurement from a single AlGaN NW.

1.4 Objective of the thesis

The prime objective of the thesis entitled as the ‘optical properties of AlGaN nanostructures’ in a nutshell is listed below,

i. Synthesis and characterization of 1D AlGaN nanostructures using the chemical vapor deposition technique *via* catalytic assisted VLS as well as self catalytic VS growth mechanism.

ii. Investigations of orientation dependent polarized Raman and photoluminescence studies on hexagonal AlGaN crystallites.

iii. Identification and analysis of the surface and interface optical phonon modes in AlGaN 1D nanorods and 2D MQW structures probed by the Raman spectra.

iv. Study of the light–matter interactions of sub–diffraction limited semiconductor and metallic nanostructures with the help of proximity induced photonic confinement and the near–field scanning optical microscopy assisted evanescent waves.

1.5 References

[1] S. Nakamura, T. Mukai and M.Senoh, *Appl. Phys. Lett.* **1994**, 64, 1687

[2] S. Zhao, H. P. T. Nguyen, M. G. Kibria and Z. Mi, *Prog. Quantum Electron.* **2015**, 44, 14

[3] A. Khan, K. Balakrishnan and T. Katona, *Nat. Photon.* **2008**, 2, 77

[4] H. Yoshida, Y. Yamashita, M. Kuwabara and H. Kan, *Nature* **2008**, 2, 551

[5] P. J. Pauzauskie, and P. Yang, *Mater. Today* **2006**, 9, 36

[6] R. Yan, D. Gargas and P. Yang, *Nat. Photon.* **2009**, 3, 569

[7] Q. Wang, A. T. Connie, H. P.T. Nguyen, M. G. Kibria, S. Zhao, S. Sharif, I. Shih, and Z. Mi, *Nanotechnology* **2013**, 24, 345201

[8] M.T. Hardy, D.F. Feezell, S.P. DenBaars and S. Nakamura, *Mater. Today* **2011**,14,408

[9] S. Nakamura, *Science* **1998**, 281, 956

[10] S. Nakamura, M. Senoh, T. Mukai, *Appl. Phys. Lett.* **1993**, 62, 2390

[11] H. Baek, C. H. Lee, K. Chung, and G. C. Yi, *Nano Lett.* **2013**, 13, 2782

[12] A. C. Tamboli, E. D. Haberer, R. Sharma, K. H. Lee, S. Nakamura, and E. L. Hu, *Nat. Photon.* **2007**, 1, 61

[13] C. Tessarek, R. Röder, T. Michalsky, S. Geburt, H. Franke, R Schmidt–Grund, M. Heilmann, B. Hoffmann, C. Ronning, M. Grundmann and S. Christiansen, *ACS Photonics* **2014**, 1, 990

[14] Y. Zhang, Z. Ma, X. Zhang, T. Wang, and H.W. Choi, *Appl. Phys. Lett.* **2014**, 104, 221106

[15] K. Chung, H. Beak, Y. Tchoe, H. Oh, H. Yoo, M. Kim, and G. C. Yi, *APL Mater.* **2014**, 2, 092512

[16] Y. Dong, B. Tian, T. J. Kempa, and C. M. Lieber, *Nano Lett*. **2009**, 9, 2183

[17] L. Caccamo, J. Hartmann, C. Fàbrega, S. Estradé, G. Lilienkamp, J. D. Prades, M. W. G. Hoffmann, J. Ledig, A. Wagner, X. Wang, L. L. Conesa, F. Peiró, J. M. Rebled, H. H. Wehmann, W. Daum, H. Shen, and A. Waag, *ACS Appl. Mater. Interfaces*, **2014**, 6, 2235

[18] Q.Wang, Q. Sun, P. Jena, and Y. Kawazoe, *ACS Nano* **2009**, 3, 621

[19] D. Wang, A. Pierre, M. G. Kibria, K. Cui, X. Han, K. H. Bevan, H. Guo, S. Paradis, A. R. Hakima, and Z. Mi, *Nano Lett.* **2011**, 11, 2353

[20] M. G. Kibria, F. A. Chowdhury, S. Zhao, B. AlOtaibi, M. L. Trudeau, H. Guo and Z. Mi, *Nat. Commun.* **2015**, 6, 6797

[21] A. Patsha, P. Sahoo, S. Amirthapandian, A. K. Prasad, A. Das, A. K. Tyagi, M. A. Cotta, and S. Dhara, *J. Phys. Chem. C.* **2015**, 119, 21251

[22] D. K. T. Ng, M. H. Hong, L. S. Tan, Y.W. Zhu and C. H. Sow, *Nanotechnology* **2007**, 18, 375707

[23] Z. W. Song, R. Z. Wang, W. Zhao, B. Wang, and H. Yan, *J. Phys. Chem. C.* **2012**, 116, 1780

[24] J. Piprek, *Nitride Semiconductor Devices; Principles and Simulation*, **2007**, WILEY–VCH Verlag GmbH & Co. KGaA, Weinheim, ISBN: 978–3–527–40667–8

[25] T. Paskova, *Nitrides with Nonpolar Surfaces: Growth, Properties, and Devices*, **2008**, WILEY–VCH Verlag GmbH & Co. KGaA, Weinheim, ISBN: 978–3–527–40768–2

[26] H. Morkoç, *Hand book of Nitride Semiconductors and Devices. Vol. 1. Materials Properties, Physics and Growth*, **2008**, WILEY–VCH Verlag GmbH & Co. KGaA, Weinheim, ISBN: 978–3–527–40837–5

[27] B. Gil, *Physics of Wurtzite Nitrides and Oxides: Passport to Devices*, **2014**, Springer Series in Materials Science 197, DOI: 10.1007/978–3–319–06805–3

[28] R. Agrawal, and H. D. Espinosa, *Nano Lett.* **2011**, 11, 786

[29] X. Xu, A. Potié, R. Songmuang, J. W. Lee, B. Bercu, T. Baron, B. Salem, and L. Montès, *Nanotechnology* **2011**, 22, 105704

[30] O. Ambacher, B. Foutz, J. Smart, J. Shealy, N. Weimann, K. Chu, M. Murphy, A. Sierakowski, W. Schaff, and L. Eastman, *J. Appl. Phys.* **2000**, 87, 334

[31] H. D. Espinosa, R. A. Bernal, and M. Minary–Jolandan, *Adv. Mater.* **2012**, 24, 4656

[32] M. M. Jolandan, R. A. Bernal, I. Kuljanishvili, V. Parpoil, and H. D. Espinosa, *Nano Lett.* **2012**, 12, 970

[33] V. Yu. Davydov, Yu. E. Kitaev, I. N. Goncharuk, A. N. Smirnov, J. Graul, O. Semchinova, D. Uffmann, M. B. Smirnov, A. P. Mirgorodsky and R. A. Evarestov, *Phys. Rev. B* **1998**, 58, 12899

[34] C. Bungaro, K. Rapcewicz and J. Bernholc, *Phys. Rev. B* **2000**, 61, 6720

[35] T. Azuhata, T. Sota, K. Suzuki, S. Nakamura, *J. Phys.: Condens. Matter.* **1995**, 7, L129

[36] H. Harima, *J. Phys.: Condens. Matter.* **2002**, 14, R967

[37] A. K. Sivadasan, A. Patsha, and S. Dhara, *Appl. Phys. Lett.* **2015**, 106, 173107

[38] M. Tanaka and R. J. Young, *J. Mater. Sci.* **2006**, 41, 963

[39] K. Filintoglou, M. Katsikini, J. Arvanitidis, D. Christofilos, A. Lotsari, G. Dimitrakopulos, N. Vouroutzis, A. Ajagunna, A. Georgakilas, and N. Zoumakis, *J. Appl. Phys.* **2015**, 117, 075302

[40] Z. Bryan, I. Bryan, M. Bobea, L. Hussey, R. Kirste, Z. Sitar, and R. Collazo, *J. Appl. Phys.* **2014**, 115, 133503

[41] S. Schulz, T. J. Badcock, M. A. Moram, P. Dawson, M. J. Kappers, C. J. Humphreys, and E. P. O'Reilly, *Phys. Rev. B* **2010**, 82, 125318

[42] G. C. Yi, *Semiconductor Nanostructures for Optoelectronic Devices: Processing, Characterization and Applications*, **2012**, Springer–Verlag Berlin Heidelberg, DOI:10.1007/978–3–642–22480–5

[43] P.Y. Yu and M.Cardona, *Fundamentals of semiconductors*, **2010**, Springer–Verlag Berlin Heidelberg, DOI:10.1007/978–3–642–00710–1

[44] M. Fox, *Optical properties of Solid*, **2001**, Oxford University Press, New York, ISBN: 978–0–19–850613–3

[45] H. Morkoç, *Hand book of Nitride Semiconductors and Devices. Vol. 2. Electronic and Optical Processes in Nitrides*, **2008**, WILEY–VCH Verlag GmbH & Co. KGaA, Weinheim, ISBN: 978–3–527–40838–2

[46] H. E. Ruda, A. Shik, *Phys. Rev. B* **2005**, 72, 115308

[47] H. E. Ruda, A. Shik, *J. Appl. Phys.* **2006**, 100, 024314

[48] J. Wang, M. S. Gudiksen, X. Duan, Y. Cui, C. M. Lieber, *Science* **2001**, 293, 1455

[49] H. Morkoç, *Hand book of Nitride Semiconductors and Devices. Vol. 3. GaN–based Optical and Electronic Devices*, **2008**, WILEY–VCH Verlag GmbH & Co. KGaA, Weinheim, ISBN: 978–3–527–40839–9

[50] D. A. Miller, *Optical physics of quantum wells*, **1996**, Institute of Physics, London

[51] T. Ruf, *Phonon Raman Scattering in Semiconductors, Quantum Wells and Superlattices*, **1998**, Springer–Verlag, Berlin

[52] A. K. Arora, M. Rajalakshmi and T. Ravindran, *Encyclopedia of Nanoscience and Nanotechnology* **2004**, 8, 499

[53] R. Gupta, Q. Xiong, G. D. Mahan, and P. C. Eklund, *Nano Lett.* **2003**, 3, 1745

[54] S. Dhara, P. Sahoo, A. K. Tyagi and B. Raj, *Nanowires–Implementation and Applications* Ed. Abbas Hashim, Intech Open Access, Croatia, **2011**, http://www.intechopen.com/articles/show/title/surface–optical–modes–in–semiconductor–nanowires

[55] I. M. Tiginyanu, A. Sarua, G. Irmer, J. Monecke, S. M. Hubbard, D. Pavlidis, and V. Valiaev, *Phys. Rev. B* **2001**, 64, 233317

[56] H. Zhu, J. Q. Ning, C. C. Zheng, S. J. Xu, S. M. Zhang and H. Yang, *Appl. Phys. Lett.* **2011**, 99, 113115

[57] S. E. Wu, Y. W. Huang, T. H. Hsueh, S. Dhara, Y. F. Lai, C. Y. Wang and C. P. Liu, *J. Raman Spectrosc.*, **2009**, 40, 2044

[58] S. Sahoo, M. S. Hu, C. W. Hsu, C. T. Wu, K. H. Chen, L. C. Chen, A. K. Arora and S. Dhara, *Appl. Phys. Lett.*, **2008**, 93, 233116

[59] S. Sahoo, S. Dhara, A. K. Arora, P. Chandramohan, M. P. Srinivasan and R. Krishnan, *Appl. Phys. Lett.*, **2010**, 96, 103113

[60] R. Mata, A. Cros, K. Hestroffer, and B. Daudin, *Phys. Rev. B,* **2012**, 85, 035322

[61] S. M. Komirenko, K. W. Kim, M. A. Stroscio and M. Dutta, *Phys. Rev. B* **1999**, 59, 5013

[62] J. J. Shi, *Phys. Rev. B* **2003**, 68, 165335

[63] Q. Xiong, J. Wang, O. Reese, L. C. Lew Yan Voon and P. C. Eklund, *Nano Lett.*, **2004**, 4, 1991

[64] C. H. Ho, P. Varadhan, H. H. Wang, C. Y. Chen, X. Fang and Jr–H. He, *Nanoscale*, **2016**, 8, 5954

[65] S. Bhattacharya, A. Datta, S. Dhara and D. Chakravorty, *J. Raman Spectrosc.*, **2011**, 42, 429

[66] A. Polman, *Science* **2008**, 322, 868

[67] E. Ozbay, *Science* **2006**, 311, 189

[68] P. Andrew, W. L. Barnes, *Science* **2004**, 306, 1002

[69] J. B. Pendry, *Phys. Rev. Lett.* **2000**, 85, 3966

[70] [N. Fang, H. Lee, C. Sun, X. Zhang, *Science* **2005**, 308, 534

[71] M. Boroditsky, R. Vrijen, T. F. Krauss, R. Coccioli, R. Bhat, E. Yablonovitch, *J. Lightwave Technol.* **1999**, 17, 2096.

[72] K. J. Vahala, *Nature* **2003**, 424, 839

[73] J. M. Gerard, B. Gayral, *J. Lightwave Technol.* **1999**, 17, 2089

[74] S. J. Yoo, Q. H. Park, *Phys. Rev. Lett.* **2015**, 114, 203003

[75] J. Li, D. Fattal, M. Fiorentino, R. G. Beausoleil, *Phys. Rev. Lett.* **2011**, 106, 193901

[76] B. Piccione, C. O. Aspetti, C. H. Cho, R. Agarwal, *Rep. Prog. Phys.* **2014**, **77**, 086401

[77] G. S. Wiederhecker, C. M. B. Cordeiro, F. Couny, F. Benabid, S. A. Maier, J. C. Knight, C. H. B. Cruz, H. L. Fragnito, *Nat. Photon.* **2007**, 1, 115

[78] T. Tanabe, M. Notomi, E. Kuramochi, A. Shinya, H. Taniyama, *Nat. Photon.* **2006**, 1, 49

[79] R. F. Cregan, B. J. Mangan, J. C. Knight, T. A. Birks, P. S. Russell, P. J. Roberts, D. C. Allan, *Science* **1999**, 285, 1537

[80] L. Rigutti, M. Tchernycheva, A. de Luna Bugallo, G. Jacopin, F. H. Julien, F. Furtmayr, M. Stutzmann, M. Eickhoff, R. Songmuang, and F. Fortuna, *Phys. Rev. B* **2010**, 81, 04541

[81] P. J. Pauzauskie, D. Talaga, K. Seo, P. Yang, and F. Lagugné–Labarthet, *J. Am. Chem. Soc.* **2005**, 127, 17146

[82] T. Livneh, J. Zhang, G. Cheng, and M. Moskovits, *Phys. Rev. B* **2006**, 74, 035320

[83] W. L. Barnes, A. Dereux and T. W. Ebbesen *Nature*, **2003**, 424, 824

[84] M. Li, S. K. Cushing and N. Wu, *Analyst*, **2015**, 140, 386

[85] J. Zhang, L. Zhang, and W. Xu, *J. Phys. D: Appl. Phys*., **2012**, 45, 113001

[86] M. Kauranen and A. V. Zayats, *Nat. Photon.* **2012**, 6, 737

[87] S. Kawata, Y. Inouye and P. Verma, *Nat. Photon.* **2009**, 3, 388

[88] H. J. Lezec, A. Degiron, E. Devaux, R. Linke, L. Martin–Moreno, F. Garcia–Vidal, T. W. Ebbesen, *Science* **2002**, 297, 820

[89] C. Genet and T. Ebbesen, *Nature* **2007**, 445, 39

[90] N. Rotenberg and L. Kuipers, *Nat. Photon.* **2014**, 8, 919

[91] M. Lucas and E. Riedo, *Rev. Sci. Instrum.* **2012**, 83, 061101

[92] A. Zayats and D. Richards, *Nano–Optics and Near–Field Optical Microscopy*, **2009**, ARTECH HOUSE, INC., ISBN–13: 978–1–59693–283–8

[93] L. Novotony and B. Hecht, *Principles of Nano–Optics*, **2006**, Cambridge University Press, New York, USA

CHAPTER 2

EXPERIMENTAL TECHNIQUES

"*It doesn't matter how beautiful your theory is, it doesn't matter how smart you are. If it doesn't agree with experiment, it's wrong*" ...Richard P. Feynman

2.1 Introduction

The present chapter includes a brief report of the experimental techniques used for the synthesis of AlGaN NWs and their characterizations to investigate the morphological, crystallographic, structural, elemental, and optical properties. The 1D AlGaN NWs were synthesized using the atmospheric pressure chemical vapor deposition (APCVD) system through two different routes; catalyst assisted vapor–liquid–solid (VLS) as well as self catalytic vapor–solid (VS) mechanisms. The depositions of Au catalyst thin films or islands were carried out by physical vapor deposition (PVD) technique by means of an electrical thermal evaporation system. The 2D multi–QW (MQW) structures of AlGaN were grown with the help of plasma assisted molecular beam epitaxy (PAMBE). The electron microscopy techniques, especially field emission scanning electron microscopy (FESEM) and transmission electron microscopy (TEM) were used for morphological and structural studies of the as–prepared nanostructures. Furthermore, the elemental analysis of the samples was performed by electron energy loss spectroscopy (EELS) and X–ray photoelectron spectroscopy (XPS) techniques. The optical properties of AlGaN NWs were studied using Raman and PL spectroscopy techniques. In addition, the piezoelectric domains of the AlGaN hexagonal crystallites were studied using the piezoresponse force microscopy (PFM) technique. Moreover, as an advanced technique for nano–science and nano–optics, the scanning probe microscopy (SPM) consisting of atomic force microscopy (AFM) and near–field scanning optical microscopy (NSOM) were used to study the topography and near–field light–matter interactions of the semiconductor NWs as well as metallic NPs.

2.2 Synthesis techniques

2.2.1 Physical vapor deposition techniques

2.2.1.1 Thermal evaporation technique

The thermal evaporation and subsequent deposition of material under consideration (mainly metals) on the substrate is one of the important techniques among the PVD methods.[1] The three major steps involved in this technique are the generation, transport, and condensation of vapor phase of metals on the substrate under high vacuum ($\sim 10^{-6}$ mbar).[1] The schematic diagram of a typical vacuum thermal evaporation system with necessary components is shown in the figure 2.1.

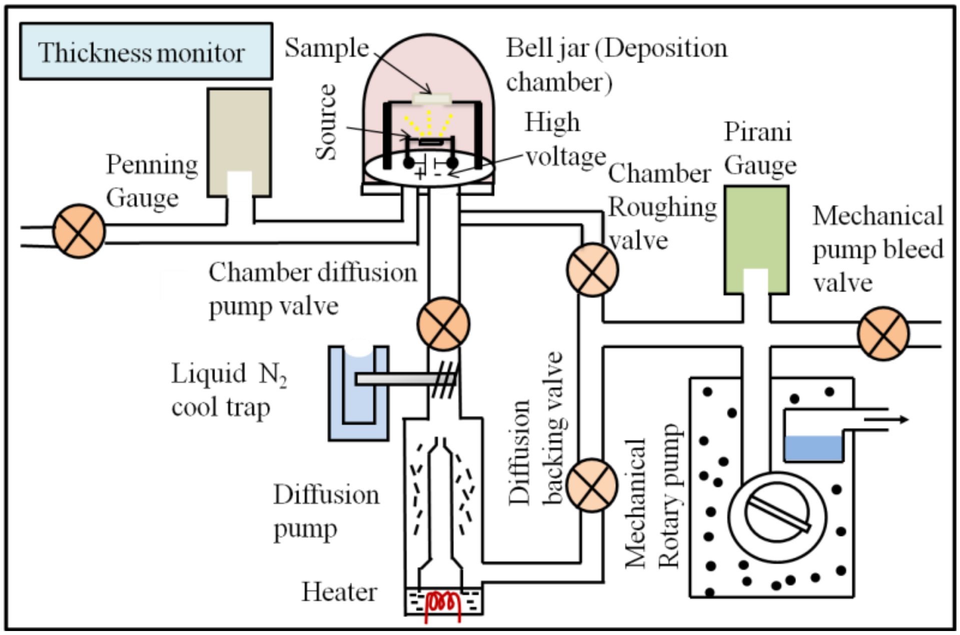

Figure 2.1 Schematic view of a typical vacuum thermal evaporation system.

The evaporation of the metal is carried out at high temperature through electrical resistive heating. Sufficiently high temperature can be generated by a heating element of W filament or Mo boat by applying high voltage to the electrodes connected to the heating elements in the high vacuum chamber. The Au catalyst metal film depositions for all the synthesis procedures based on the VLS mechanism reported in this thesis were carried out in the high vacuum thermal evaporation system (HINDHIVAC Vacuum Coater–12A4D) with the multi–source evaporation and *in–situ* thickness monitor facilities. The important components of the system are listed below.

A. Vacuum chamber: Bell jar type
B. Substrates: Si(100) and *c*–sapphire
C. Vacuum pumping system:
    a) Rotary pump (ED–15, 250 L. min^{-1}, 1 × 10^{-3} mbar)
    b) Diffusion pump (OD–114D, 280 L. s^{-1}, 1 × 10^{-6} mbar)
    c) Vacuum gauges (Pirani and Penning Gauges); Maximum vacuum: 1 × 10^{-6} mbar.
    d) Primary current (Maximum): 100 Å
D. Digital thickness monitor:
    a) Quartz crystal thickness monitor, 0.1 Å. s^{-1} resolution,
    b) Optimized thickness of the Au films used for VLS mechanism; 2 and 4 nm.

2.2.1.2 Plasma–assisted molecular beam epitaxy

The MBE is a vapor phase epitaxy synthesis method where solid or gas precursor materials are heated and evaporated using Knudsen effusion cells. A beam of atoms produced from effusion cells were bombarded and subsequently deposited on the substrate, which could be rotated and heated to appropriate optimized growth temperatures as shown in the schematic figure 2.2. In order to achieve the mean free path of the effused atoms larger than the dimensions of the chamber and to obtain the deposited films with high purity, ultra–high vacuum (10^{-9} Torr) is required in the deposition chamber.[2,3] The growth temperatures of 600–800°C are good enough to grow very thin layers which can fall in the quantum confined region with fine control of composition.

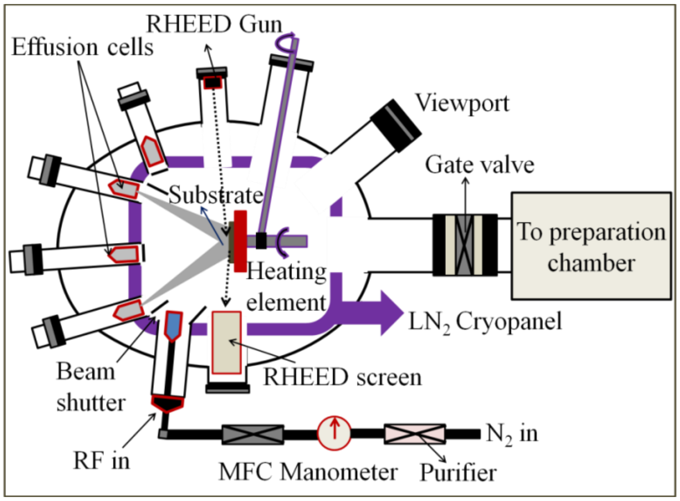

Figure 2.2 Schematic view of the PAMBE system used for growth of AlGaN MQW structures.

The precision of MBE technique depends upon the lower deposition rates of precursors and *in–situ* monitoring of reflection high energy electron diffraction (RHEED) detector to control the thickness of the film up to one atomic monolayer. The basic principle of RHEED is relied on the wave nature of electron (e^-). The interaction of e^-s with the sample specimen according to the crystal structure and the inter–atomic spacing at the sample surface leading to a specific diffraction pattern is generated on the RHEED screen. The observed electron diffraction pattern allows us to analyze the crystallography of the sample surface. Standard effusion cells are used as sources of Ga and Al elements and plasma N_2 sources are normally employed as a precursor for N. The plasma environment created in the plasma assisted MBE (PAMBE) by the radio frequency (RF) sources are used to energize the N_2 molecules, which then helps in their dissociation. Atomic N is highly reactive enough to create compounds with evaporated metal atoms of group III elements from effusion cells in the PAMBE system. The main sequential steps involved in the PAMBE deposition process are adsorption, desorption, surface diffusion, incorporation and decomposition.[3]

The major components of the PAMBE system are listed below.

A. PAMBE system (VEECO Gen 930)
B. Effusion cells (for Al and Ga sources); Heating elements and substrate (*c*–sapphire)
C. Substrate degassing: Background vacuum level; ~10^{-9} Torr, at a temperature of 500 ^{o}C for 48 h.
D. Beam equivalent pressures (BEP) for Al and Ga; 4.7 $\times 10^{-8}$ and 4.6 $\times 10^{-7}$ Torr, respectively.
E. Temperature for the nitradation of sapphire substrate and growth : 800 ^{o}C
F. Growth rate : 45 Å/min
G. RF plasma source power: 350 W for growth and 400 W for nitradation of substrate
H. Nitrogen flow rate: 1.7 sccm
I. Reflection high energy electron diffraction (RHEED) detector
J. Number of layers deposited for MQW structures in the present study : 20

2.2.2 Atmospheric pressure chemical vapor deposition

The desired material can be synthesized and deposited on the substrate by using CVD, after a chemical reaction prior to the deposition. The main processes involved in the CVD method are the generation, transport, absorption and chemical reactions of vapor phase species on the substrate surface.[4] Prior to the chemical reactions inside the CVD chamber, the transport of the reactant vapor is created by the evaporation and decomposition of the precursors which may be in the form of gas, liquid or solid phases. The transport of vapor phase species is usually carried out by means of carrier gases, mostly inert gases or by the self movement of reactive gaseous precursors. A schematic for the experimental setup of custom–built APCVD system, used for the growth of AlGaN NWs or hexagonal crystallites reported in the present thesis, is depicted in the figure 2.3 and its major components are listed below,

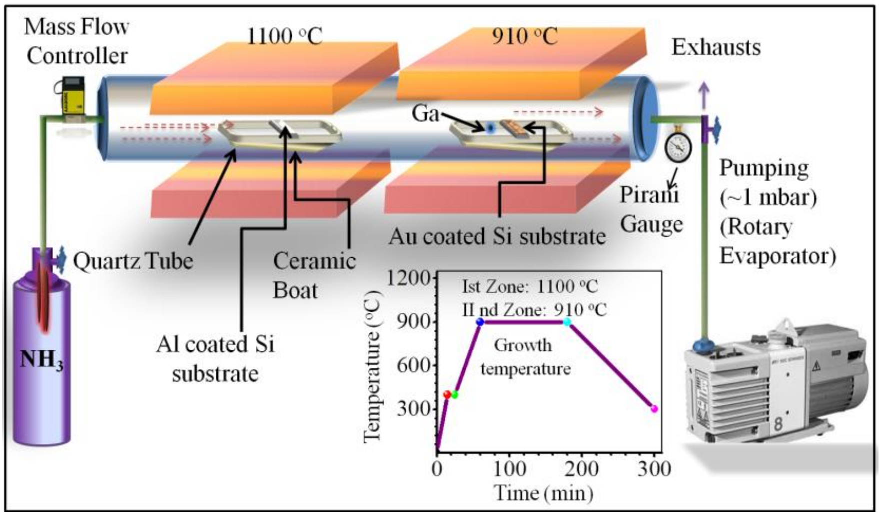

Figure 2.3 Schematic view of the APCVD system used for growth of AlGaN NWs.

A. High temperature two split zone vacuum tube furnace: (MTI–OTF–1200X–III)

  a) Heating elements: Fe–Cr–Al Alloy doped by Mo

  b) Maximum temperature: 1200 °C

  c) Optimized growth temperatures:

    910 °C (substrate) and 1100 °C (source; Al thin film)

  d) Temperature controllers: PID automatic control; Temperature accuracy: ±1°C

B. Vacuum pumping system:

a) Rotary pump (Edwards, RV12, 1 × 10^{-3} mbar)

c) Vacuum gauges (Pirani Gauges); Maximum vacuum: 2 × 10^{-3} mbar.

C. Gas delivery system:

a) Reactant gas: NH_3

b) Mass flow controllers (Aalborg, MKS)

c) Optimized flow rate of NH_3: 50 sccm

2.3 Morphological analysis: Field emission scanning electron microscopy

The electron microscopy is a field of science in which e^- beam is used to form a magnified image and more precise diffraction pattern of the material as compared to that of the conventional light microscopes. The electron microscopy utilizes the advantage of significantly short wavelength of the e^-s which can be focused with the help of electromagnetic lenses. The wavelength of an e^- can be calculated by,

$$\lambda = \frac{h}{\sqrt{2m_0eV\left(1+\frac{eV}{2m_0c^2}\right)}} \qquad \text{……..............……………..} \quad (2.1)$$

Where, h is Plank's constant, m_0 is the rest mass of the electron, e is the charge of the e^- and V is the applied electric potential. The quantity $\left(1+\frac{eV}{2m_0c^2}\right)^{\frac{1}{2}}$ is the relativistic correction term applied when the incident e^- energy is ≥ 100 keV.[5] An accelerated beam of e^-s with a high potential difference impinges on the target material under consideration. The bombarding of accelerated e^- beam on the surface of the sample specimen results in a several number of consequent elastic and inelastic interactions (Fig. 2.4a).[5] The deflection of e^-s from the nucleus or by outer shell e^-s of target atoms with similar energy results in the elastic scattering. The elastically backscattered electrons (BSEs), which are emitted through an angle more than 90^o posses energy comparable to the primary e^- beam. By convention, if the energy of the emitted e^- is greater than ~50 eV, then it is considered as BSE. Whereas, in the case of the inelastic scattering, a little amount of energy of primary e^- beam is transferred to the target atom. If the energy transferred to the target atom exceeds the work function of the material, then it can knock out additional e^-s, which can escape from the solid surface and are termed as secondary electrons (SE). The energy of this SEs is less than ~50 eV. Most of the emitted SEs are produced within the first few nm scale of the surface.

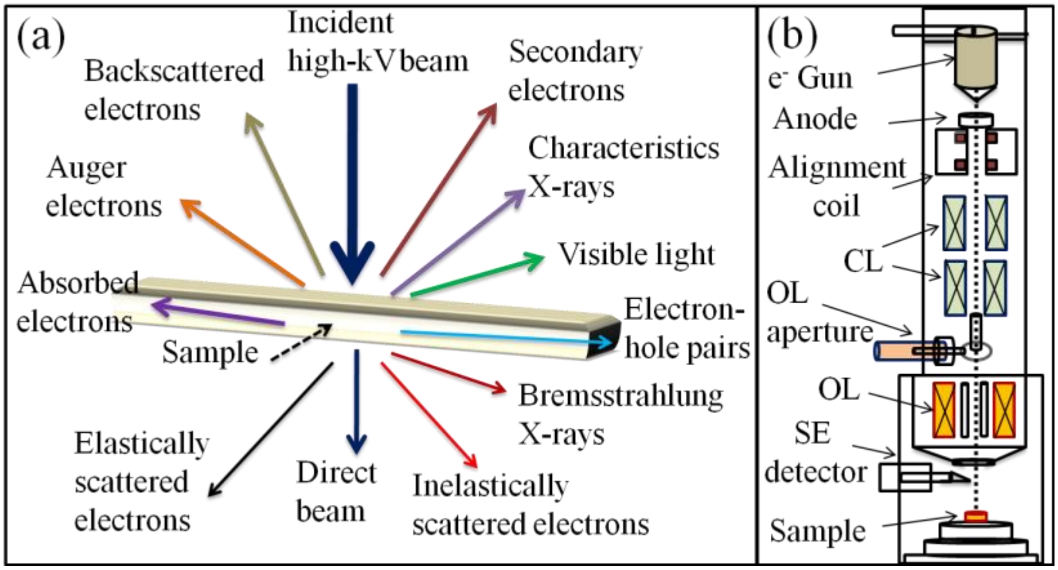

Figure 2.4 (a) Schematic view of the several interactions occurs in a material due to the incidence of high energy e^- beam. (b) Block diagram of a FESEM showing the major parts of the system.

By detecting and scanning the BSE and SE, the image formation can be carried out for the topography and Z–contrast variations in the sample. The major components of a SEM are also shown (schematic view, Fig. 2.4b). The morphological studies of the AlGaN NWs and crystallites reported in the present thesis were carried out using FESEM (SUPRA 55 Zeiss) with 30 kV source from a tungsten field emission tip.

2.4 Structural analysis

2.4.1 X–ray diffraction

When an electromagnetic (*em*) radiation of wavelength (λ) incident on a crystalline material with a periodic lattice structure, then the diffraction of *em* wave occurs. Generally, the X–rays possess a λ (normally Cu–K_α =1.54056 Å), which is comparable to the dimensions of the inter–planar spacing (*d*) of a crystal. Therefore, the X–rays are the commonly used *em* waves to produce the characteristic diffraction pattern of material for the phase identifications. The Braggs diffraction criterion for obtaining the interference pattern from the consecutive set of lattice planes of the material is,[6]

$$2d\, sin\theta = n\lambda \quad \text{……………………………………} \quad (2.2)$$

where, θ is the angle of incidence and n is the integer representing the order of diffraction. The each characteristic peak in the resultant diffraction pattern can be correlated to a set of planes in a crystal lattice. The glancing incidence X–ray diffraction (GIXRD) is a technique used to record the diffraction pattern of thin films, with a minimum contribution from the substrate. In GIXRD, the penetration depths of the X–rays are restricted to ~10–100 Å by keeping the angle of incidence of X–ray at a very small value ($<5^o$). The XRD pattern obtained from the sample was compared with the powder diffraction file collected from JCPDS–ICDD standards. In the present study, the as–prepared samples were analyzed with GIXRD mode using the Bruker D8 Discover (Germany).

2.4.2 Transmission electron microscopy

The TEM is capable of displaying magnified images of a thin specimen, typically with a magnification of the order of 10^3 to 10^6. In principle, the TEM exploits three different interactions of e^- beam with the target specimen; they are unscattered e^-s (transmitted/direct beam), elastically scattered e^-s (diffracted beam) and inelastically scattered e^-s (Fig. 2.5).[5] The transmission of unscattered e^-s without any interaction with the sample is inversely proportional to the specimen thickness. The thicker regions of the sample specimen leading to the transmission of less number of unscattered e^-s and the corresponding area of the sample may appear as dark; conversely the thinner areas may transmit more number of e^-s and the image may appear as bright.

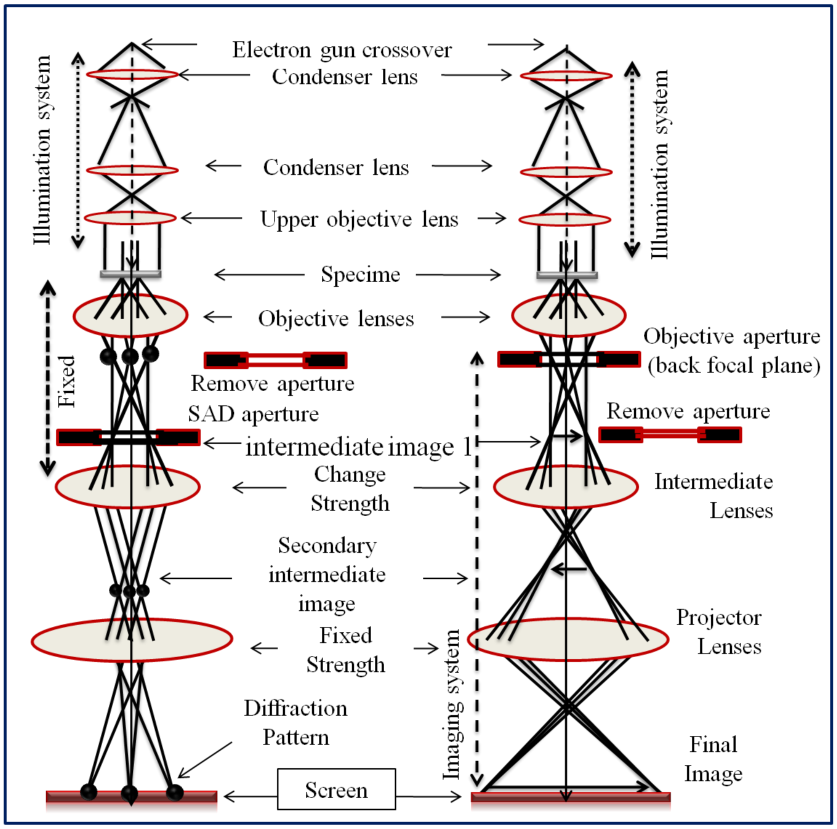

Figure 2.5 The ray–diagram of a typical TEM showing the diffraction mode operation (left side) and standard imaging mode operation (right side).

Another part of the incident e^-s that are elastically scattered by the atoms in the specimen are then transmitted through the remaining portions of the specimen. All the diffracted e^-s follow the Bragg's law (Eqn. 2.2), where d being the atomic spacing, θ being the angle between incident e^-s and atomic planes of the specimen, λ being the wavelength of incident e^-s and n is an integer. By selecting the diffracted beam from a selected area on the specimen, selected area electron diffraction (SAED) pattern can be obtained. The SAED pattern is equivalent to an X–ray diffraction pattern. A single crystal leads to a well arranged spot pattern on the screen; a poly–crystal constitutes a ring pattern. Whereas, a glass or amorphous material produces a series of diffuse halos. The major components of the TEM can be categorized into the illumination system, the objective lens/stage, and the imaging system. By adjusting these three components of TEM and selecting the appropriate scattered e^- beams from the specimen, several types of TEM images can be obtained. General analysis of the samples can be carried out by the different modes of the TEM, such as the bright field and dark field images, SEAD patterns, high resolution TEM (HRTEM) and fast Fourier transform (FFT) images. Most of the structural studies of the AlGaN NWs reported in the present thesis were carried out using HRTEM (LIBRA 200FE Zeiss) with 200 kV FE electron source.

2.5 Elemental analysis

2.5.1 Electron energy loss spectroscopy and energy filtered TEM

The EELS involves the measurement of the energy distribution of e^-s that can interact with a sample specimen and loose its characteristic amount of energy due to the inelastic scattering.[7] The inelastic scattering of incident e^-s leads to several interactions in the specimen such as inter– and intra–band transitions, plasmon interactions, ionization of core shell e^-s (K, L, M,

N) and plural scattering. In order to observe the characteristic energy loss of incident e^-s (typically 100 keV), the transmitted e^- beam is directed into a high–resolution e^- spectrometer (Fig. 2.6). The spectrometer separates the e^-s according to their kinetic energy and shows an e^- energy loss spectrum with the number of e^-s (scattered intensity) as a function of the decrease in kinetic energy (KE, ~0–1500 eV).[7] The EELS spectrum is divided into two regions, low– and high–loss interaction regions. The low–loss interaction regions possess typically 0–50 eV energy loss, which consist of a zero–loss peak (0 eV), inter– and intra–band transitions (2–20 eV) and plasmon interactions (5–30 eV).

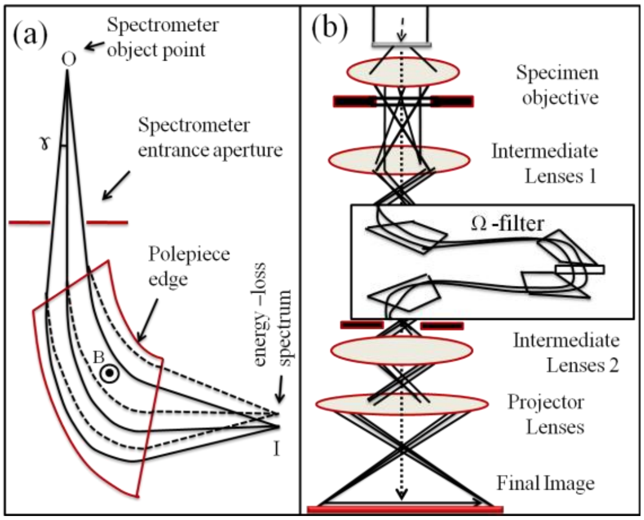

Figure 2.6 (a) Ray–diagram of a magnetic prism in a plane perpendicular to the magnetic field. Solid lines represent zero–loss e^-s (E=0); dashed lines represent the e^-s lost energy during transmission through the specimen. (b) Block diagram of a TEM–EELS system having in–column second order corrected omega energy filter.

Whereas, the high–loss interaction region (>50 eV energy loss) consists ionization edges of core shells, energy–loss near–edge structure (ELNES) and extended energy–loss fine structure (EXELFS). The EELS is preformed using a spectrometer based on magnetic prism (Fig. 2.6a) attached to the TEM. A highly uniform magnetic field (B = 0.01 T) produced between two parallel faces of an electromagnet in the magnetic prism, exerts a force $F = evB$ on each e^- and bend the e^-s into circular paths of radius $R = (m/e)(1/B)v$, where e, m and v are e^- charge, speed, and relativistic mass, respectively. Depending on the kinetic energy (*KE*) of the e^-s entered into the magnetic prism, e^-s are dispersed and collected by the detector to produce an EELS spectrum. Instead of recording the energy–loss spectrum from a particular region of the specimen, a magnified image of the specimen (or its diffraction pattern) can be displayed at a selected energy loss. This can be carried out by filtering the e^-s either by using a narrow slit inserted at the spectrum plane or by changing the spectrometer current, to form an EFTEM image. The major components for the EELS and EFTEM imaging in a TEM system with in–column imaging filter are shown in a schematic view (Fig. 2.6b). The EELS and EFTEM studies of the AlGaN NWs reported in the present thesis were carried out using a TEM (LIBRA 200FE Zeiss) with 200 kV FE e^- source and in–column second order corrected omega energy filter type spectrometer with an energy resolution of 0.7 eV.

2.5.2 X–ray photoelectron spectroscopy

The XPS works based on the process of photoemission (Fig. 2.7a) in which e^- is ejected from a core level of an atom in the specimen by an incident X–ray photon of energy $h\nu$.[8] The energy of the emitted photoelectrons is then analyzed by the e^- spectrometer and the results are plotted as a graph with intensity (counts or counts/s) versus e^- energy. The discrete *KE* of the photoelectrons ejected is given by the relation,

$$KE = h\nu - BE - \phi \qquad \ldots\ldots\ldots\ldots\ldots\ldots (2.3)$$

Where, $h\nu$ is the quantum of energy of the incident photon, *BE* is the binding energy of the e^- and ϕ is the work function of the material. The photon absorption is an instantaneous process and takes place within the time span of 10^{-16} s. If the quantum energy of incident light; $h\nu$ is less than *BE* +ϕ, no photoemission process will be initiated. As the *BE* decreases, the *KE* energy of the photoelectron increases. The intensity of the photoelectron emission is proportional to the intensity of incident photons. By analyzing the *KE*s of the photoelectrons, the *BE* of the photoelectrons and corresponding energies of the electrons orbitals can be calculated. Since the energies of various orbitals are characteristic feature of an element, based on the *BE*s of the emitted photoelectrons, one can identify the elements present in the material.

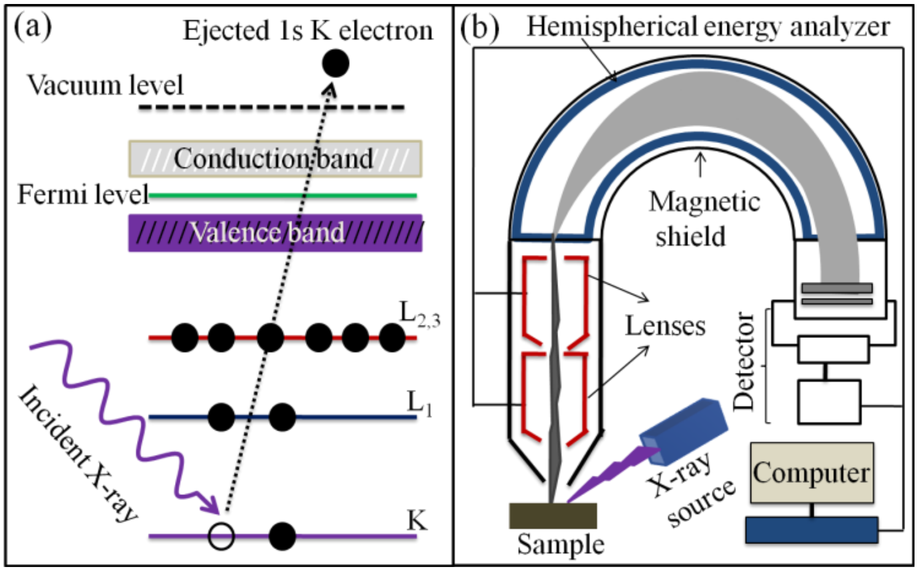

Figure 2.7 (a) Schematic view of the X–ray induced photoelectron emission process. (b) Block diagram of the XPS setup with major components.

The major components of an XPS system are shown in the schematic (Fig. 2.7b). In the present thesis, XPS studies on AlGaN crystallites were carried out using an X–ray source of Al–K_α (1486.6 eV) along with a hemispherical electron energy analyzer, and the *BE* values were measured by referencing with respect to the C 1*s* peak. The spectra were processed by applying the Shirley type background and curve fitted with a mixture of the Gaussian–Lorentzian line shape.

2.6 Optical characterization techniques

2.6.1 Raman spectroscopy

The Raman scattering is an inelastic scattering of the light by elementary excitations such as phonons and plasmons present in the materials or molecules. When a beam of light with a frequency of ω_I is impinging on a material, most of the light gets scattered elastically (without change in energy).[9,10] A small fraction of light is scattered inelastically (with change in energies) with frequencies $\omega_I \pm \omega_m$, where ω_m are the characteristic vibrational frequencies of the e^- cloud in the material (phonon frequency).

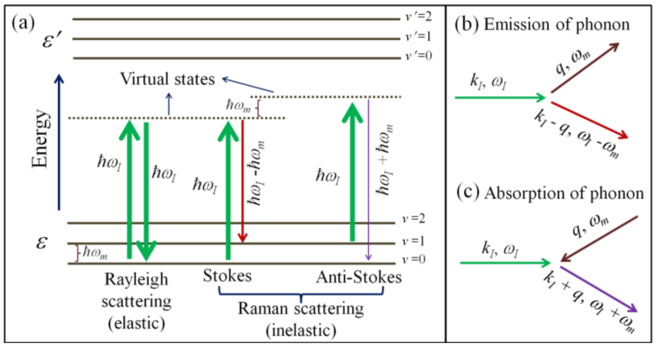

Figure 2.8 Schematic view of (a) the elastic and inelastic scattering of incident light with the material (b) Emission (Stokes) and (c) Absorption (Anti–Stokes) of phonon.

The spectral bands with frequencies $\omega_I - \omega_m$ are called Stokes Raman modes, whereas the spectral bands with frequencies $\omega_I + \omega_m$ are called anti–Stokes Raman modes. Thus, the energy differences between the incident and the Raman scattered photons are equal to the frequencies (ω_m) of lattice vibrations or phonons.

2.6.1.1 Quantum theory of Raman spectroscopy

The quantized lattice vibrations are called phonons. There exist a several discrete excited states (Fig. 2.8a) above the ground state corresponding to the different vibrational modes of a material. When an incident photon with energy $\hbar\omega_I$ and momentum $\hbar k_I$ undergoes inelastic scattering, a phonon of energy $\hbar\omega_m$ and momentum $\hbar q$ is either emitted or absorbed in the lattice of the material. However, the total energy and momentum before and after the scattering is conserved. At the stage of the creation of a phonon (Fig. 2.8b), the lattice goes to a higher excited vibronic state from the ground state by the absorption of energy from the incident photon. Conversely, in the phonon absorption process (Fig. 2.8c), lattice returns to the ground state from the vibronic excited state by releasing energy. The energy and momentum conservation demands the following conditions for the above mentioned light scattering processes,[9-11]

$$\hbar\omega_S = \hbar\omega_I \pm \hbar\omega_m\,;\ \hbar k_S = \hbar k_I \pm \hbar q \qquad \ldots\ldots\ldots\ldots\ldots\ldots\ldots\ldots (2.4)$$

where, $\hbar\omega_S$ and $\hbar k_S$ are the scattered photon energy and momentum, respectively. Moreover, the +ve sign in the equation 2.4 indicates a phonon absorption (anti–Stokes, $k_S=k_I+q$, $\omega_S=\omega_I+\omega_m$) whereas, the –ve sign indicates a phonon emission (Stokes, $k_S=k_I-q$, $\omega_S=\omega_I-\omega_m$). The magnitude of the scattering vector q depends on the scattering angle (Fig. 2.8b and 2.8c);[9-11]

$$|\vec{q}| = \left|\vec{k}_I - \vec{k}_s\right|;\ |\vec{q}| = 2\left|\vec{k}_I\right|\sin\left(\frac{\theta}{2}\right) \qquad \ldots\ldots\ldots\ldots\ldots\ldots\ldots\ldots (2.5)$$

where θ is the scattering angle. Thus, for a Raman scattering measurement performed in the back scattering geometry, $|\vec{q}| = 2\left|\vec{k}_I\right|$. Hence, the maximum value of q that can be achievable in Raman scattering (for UV–visible, IR light) is $|\vec{q}| = 2\left|\vec{k}_I\right|$, which is of the order ~10^5 cm^{-1}. This value of q is very small compared to that of the dimension of the Brillouin zone boundary in a typical crystal (~10^8 cm^{-1}). Moreover, the momentum transfer from a photon to a phonon is comparatively negligible. Therefore, only the zone–center phonons will be Raman active (first–order Raman scattering, q = 0) or in other words the Raman scattering is capable to probe only the near zone–center phonons. However, the reduction in the dimension of material, especially in the case of nanostructures, the momentum conservation is often relaxed. In such situations, the non–zone centered ($q \neq 0$) phonons can be Raman active (e.g. surface and interface optical phonon modes). The relaxation of Raman selection rule may also lead to the higher–order Raman scattering. The higher–order Raman scattering related to the continuum of phonon density of state and the specific higher–order scattering process *e.g.*, overtone and combination modes. Generally, Raman scattering intensity I can be expressed as:

$$I(\omega_I) \propto \omega_s^4 \left|\hat{e}_I . R . \hat{e}_S\right|^2 \left| \sum_{\alpha\beta} \frac{1}{(E_\alpha - \hbar\omega_I)(E_\beta - \hbar\omega_\beta)} \right|^2 \qquad \ldots\ldots\ldots\ldots\ldots\ldots\ldots (2.6)$$

where, E_α and E_β are the energy of the intermediate states available *e.g.*, band gap energy, exciton, impurity state levels and others. R is the Raman tensor with respect to the scattered ($\hat{e}_S$) and incident ($\hat{e}_I$) lights polarization vectors, respectively. In the equation 2.6, the first term represents the radiation due to dipole transition; the middle term is related to the change of polarizability and the crystal symmetry, while the last term contributes to the resonance effects. Moreover, from a quantum mechanical theory, the ratio of the intensities of Stokes to anti–Stokes scattering events are given by [9]

$$\frac{I_S}{I_{AS}} = \frac{(\omega_I - \omega_m)^4}{(\omega_I + \omega_m)^4} \exp\left(\frac{\hbar\omega_m}{k_B T}\right) \qquad \ldots\ldots\ldots\ldots\ldots\ldots\ldots (2.7)$$

where k_B is the Boltzmann constant and T is the temperature in Kelvin. Therefore, it is obvious from equation 2.7 that the population of phonons in a material in the ground state is much larger than the first excited vibronic state and hence the Stokes bands are more intense than the anti–Stokes bands, at ambient conditions.

2.6.1.2 Polarized Raman spectroscopy

Generally, the spectroscopy is a measure of the light–matter interaction. Among them, the polarized Raman spectroscopy is capable to provide crucial information about the crystal structure of the sample specimen. When the light is incident on the matter, the overall interactions of phonon mode are the resultant of the cumulative effect of all the *em* polarization states. When a material is exposed to linearly polarized light, the interactions may differ from that of with the depolarized light with respect to the material orientation relative to the polarized light axis. A typical polarization experiment includes the investigations of the interactions of the sample specimen with linearly polarized light. The two major steps included in the polarization measurements are, the collection of a spectrum with the light polarized along one axis, and then a subsequent recording of a second spectrum with the linearly polarized light rotated perpendicular to the first axis. The Porto notation depicts the configurations for the incident and scattered propagation as well as electric polarization vectors, respectively. Essentially, the Porto notation consists of four terms as follows:[11,12]

$$k_I(e_I e_S)k_S \quad ; \quad \begin{array}{l} k_I = \text{direction of propagation of the incident laser} \\ e_I = \text{direction of electric polarization of the incident laser} \\ e_S = \text{direction of electric polarization of the scattered Raman} \\ k_S = \text{direction of propagation of the scattered Raman} \end{array} \qquad \text{....(2.8)}$$

The terms outside the parentheses (Eqn. 2.8) define the propagation direction of the incident laser beam and the outgoing Raman scattered signals. Whereas, the terms inside the parentheses indicate the electric polarization direction of the incident and Raman scattered light. In case of the isotropic sample specimen, the recording of just two polarization measurements is sufficient enough to analyze the crystallographic information of the material,

1. Analyzer aligned parallel to the laser electric polarization axis, $Z(XX)\bar{Z}$ or $Z(YY)\bar{Z}$
2. Analyzer perpendicular to the laser electric polarization, $Z(XY)\bar{Z}$ or $Z(YX)\bar{Z}$

Whereas, in case of the anisotropic sample specimen, there are four polarization tensors for analyze to get crystallographic information with a Raman microscope. They are,

1. $Z(XX)\bar{Z}$; laser polarized parallel to an *X* axis; analyzer set to pass *X* polarized light
2. $Z(YY)\bar{Z}$; laser polarized parallel to a *Y* axis; analyzer set to pass *Y* polarized light
3. $Z(XY)\bar{Z}$; laser polarized parallel to an *X* axis; analyzer set to pass *Y* polarized light
4. $Z(YX)\bar{Z}$; laser polarized parallel to a *Y* axis; analyzer set to pass *X* polarized light

Therefore, in the case of an anisotropic or unknown sample, it is recommended to record the Raman spectra with all the above mentioned four polarization configurations. A 3D frame of reference can be used to describe the orientation of incident light with respect to that of the target sample specimen. The electric field component of the *em* light can be resolved into three mutually perpendicular orientations namely E_x, E_y, and E_z. Similarly, the polarization vectors of the sample can be resolved into P_x, P_y, and P_z to describe the dipole induced by the light in the target material. The electric field and polarization vectors are related by a 3×3 matrix called the polarization tensor,[9,12-15]

$$\begin{bmatrix} P_x \\ P_y \\ P_z \end{bmatrix} = \begin{bmatrix} \alpha_{xx} & \alpha_{xy} & \alpha_{xz} \\ \alpha_{yx} & \alpha_{yy} & \alpha_{yz} \\ \alpha_{zx} & \alpha_{zy} & \alpha_{zz} \end{bmatrix} \begin{bmatrix} E_x \\ E_y \\ E_z \end{bmatrix} ; \qquad \begin{aligned} P_x &= \alpha_{xx}E_x + \alpha_{xy}E_y + \alpha_{xz}E_z \\ P_y &= \alpha_{yx}E_x + \alpha_{yy}E_y + \alpha_{yz}E_z \\ P_z &= \alpha_{zx}E_x + \alpha_{zy}E_y + \alpha_{zz}E_z \end{aligned} \quad \text{……… (2.9)}$$

where α_{xx} is the component of poalrizability for an incident x polarized light and the molecule polarization along the x axis. Similarly, the other coefficients in the tensor represent the respective poalrizability components along other possible orientations. From the above equation 2.9, it is obvious that the induced dipole in one direction depends on all the three components of electric field vectors. An oscillating dipole can radiate the *em* waves, but it cannot scatter light along the same axis of the dipole oriented itself. Therefore, if the Raman signals are collected with backscattering geometry (along z–axis), then it can be considered as $E_z = 0$ for the different polarization configurations. Moreover, the light scattered due to P_x and P_y are only collected by the detector. Therefore, in the backscattered configuration of Raman spectrometer, the equation 2.9 can be reduced to:[9,12-15]

$$P_x = \alpha_{xx}E_x + \alpha_{xy}E_y \quad ; \qquad P_y = \alpha_{yx}E_x + \alpha_{yy}E_y \qquad \ldots\ldots\text{. (2.10)}$$

Moreover, the corresponding intensity of scattered light is proportional to the square of the induced dipole along the respective directions as,

$$I_x \infty \alpha_{xx}^2 E_x^2 + \alpha_{xx}\alpha_{xy}E_xE_y + \alpha_{xy}\alpha_{xx}E_yE_x + \alpha_{xy}^2 E_y^2 \,; I_y \infty \alpha_{yx}^2 E_y^2 + \alpha_{yx}\alpha_{yy}E_xE_y + \alpha_{yy}\alpha_{yx}E_yE_x + \alpha_{yy}^2 E_y^2 \quad \text{....(2.11)}$$

Similarly, if the excitation laser is linearly polarized along one axis, the corresponding term goes to zero. Thus, for a y–polarized laser: $E_z = 0$, $E_x = 0$, and $E_y \neq 0$, equations. (2.11) reduce to the following (along with the corresponding Porto notations):[9,12-15]

$$I_x \infty \alpha_{xy}^2 E_y^2 \;\; (\mathrm{Z}(YX)\bar{Z}) \quad ; \qquad I_y \infty \alpha_{yy}^2 E_y^2 \;\; (\mathrm{Z}(YY)\bar{Z}) \qquad \ldots\ldots\ldots\ldots\ldots\text{. (2.12)}$$

On the other hand, if the excitation laser polarization is flipped into the x axis, then $E_z = 0$, $E_y = 0$, and $E_x \neq 0$, and then equation. 2.11 reduced to the form of

$$I_x \infty \alpha_{xx}^2 E_x^2 \;\; (\mathrm{Z}(XX)\bar{Z}) \quad ; \qquad I_y \infty \alpha_{yx}^2 E_y^2 \;\; (\mathrm{Z}(XY)\bar{Z}) \;\; \ldots\ldots\ldots\ldots\ldots\text{. (2.13)}$$

Therefore, the equations 2.12 and 2.13 constitute the possible four polarization measurements available in the Raman microscopic system used in the present study.

2.6.1.3 Depolarization ratio

The ratio of the intensities of Raman modes in the perpendicular to the parallel polarization configuration is known as the depolarization ratio.[9,12-15] The depolarization ratios for a light polarized along either the *y*– or *x*–axis and propagating along *z*–axis are given below,

$$E_z = 0,\ E_x = 0,\ \text{and}\ E_y \neq 0; \qquad \rho = \frac{I_\perp}{I_{||}} = \frac{I_x}{I_y} = \frac{\alpha_{xy}^2 E_x^2}{\alpha_{yy}^2 E_y^2}$$

……………..(2.14)

$$E_z = 0,\ E_y = 0,\ \text{and}\ E_x \neq 0; \qquad \rho = \frac{I_\perp}{I_{||}} = \frac{I_y}{I_x} = \frac{\alpha_{yx}^2 E_y^2}{\alpha_{xx}^2 E_x^2}$$

Therefore, it is necessary to measure the depolarized (non–polarized) spectrum to completely analyze the crystalline nature of the sample specimen. It is well known that, for a depolarized (non–symmetric) vibrations, $\rho = {}^3/_4$. Whereas, in the case of polarized vibrations (totally symmetric), it is $0 \leq \rho \leq {}^3/_4$.[9,12-15] The normal and polarized Raman scattering studies on AlGaN nanostructures, reported in this thesis, are carried out using a micro–Raman spectrometer (inVia, Renishaw). All the major components are reported below along with available facilities of the system assisted with the block diagram (Fig. 2.9).

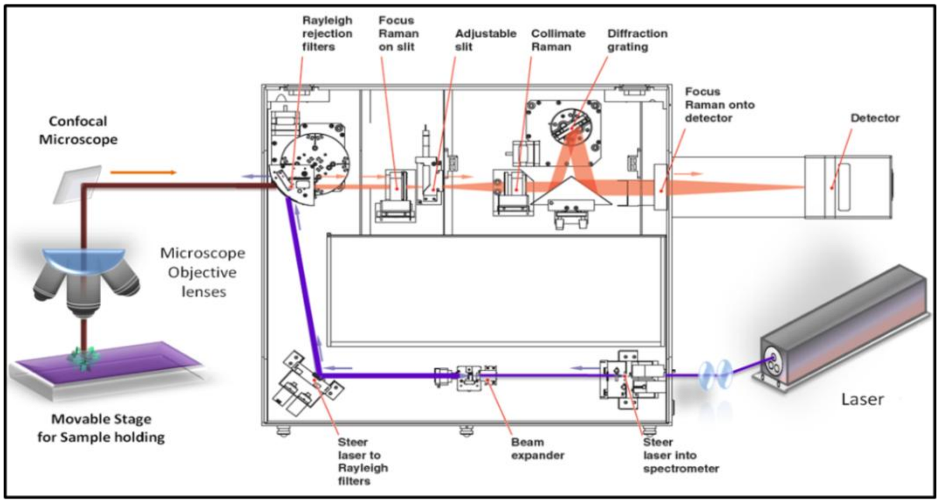

Figure 2.9 Block diagram of a typical Raman setup with major parts, used in the present studies.

The major components of a Raman spectrometer are listed below,

A. Lasers: Ar^+ laser with 514.5 and 488 nm (Total power ~ 150 mW), He–Cd Laser (UV–325 nm, Power 50 mW), and 785 nm NIR laser.

B. Microscope and lenses (Leica): Backscattering configuration, standard and confocal mode, ×5, ×20, ×50, ×100, ×15 (UV), and ×40 (UV) lenses

C. Rayleigh rejection filter: Edge filter

D. Monochromator: Gratings; 600, 1800, 2400, and 3000 $gr.mm^{-1}$

E. Detector: Thermoelectrically cooled CCD and InGaAs detectors

F. Additional facilities: Liquid N_2 stage (Linkam THMS 600) for low temperature measurements, motorized XYZ stage with 100 nm XY step size resolution (Renishaw, MS20), for imaging and sample movements. The polarized Raman imaging was performed by integrating intensities corresponding to the allowed Raman modes with respect to the different scattering polarization configurations. The collected intensity is essentially the peak intensity distribution of a particular wave number corresponding to the allowed Raman modes collected over a predefined area and grid resolution.

2.6.2 Photoluminescence spectroscopy

The PL is a process of re–emission of light by a material after the absorption of photons ($\hbar\omega_I$) with higher energy than the band gap ($E_g=\hbar\omega$) of a semiconductor.[10,16] The PL is a radiative recombination process of e^-s and holes (h) or excitons (e^-–h pair) in the semiconductor which continues for a period of the external optical excitation process. If the excitation photons of energy is higher than that of the E_g of the semiconductor, then the e^-s get excited from the ground state (valence band, VB) to a higher energy state (conduction band, CB) through the absorption of photons (Fig. 2.10). After some energy loss by means of non–radiative transitions (relaxation), the excited e^{-}s returns to the ground state with an emission of photons (recombination) of energies lower than the excitation photons (Fig. 2.10).

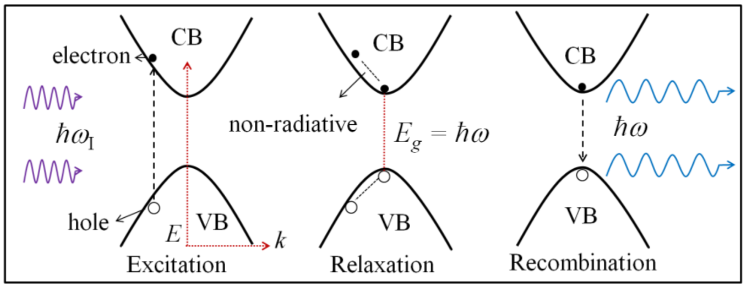

Figure 2.10 Schematic view of the PL processes in a direct band gap semiconductor.

The momentum conservation of the radiative recombination process of e^{-}s and holes or excitons demands $\vec{k}_e - \vec{k}_h = \vec{k}_{photon} \approx 0$, where, $\vec{k}_e, \vec{k}_h$ and $\vec{k}_{photon}$ being the wavevetors of e^{-}s, holes and photons, respectively. The long range Coulombic interaction between the e^{-}s and holes creates an exciton which travels through the crystal lattice with a wave vector value of $\vec{K} = \vec{k}_e + \vec{k}_h$. The maximum light–matter interaction in terms of the exciton and radiation field occurs only when the value of exciton polariton momenta $\vec{K}$ is comparable to that of $\vec{k}_{photon}$. Therefore, if the semiconductors satisfy the condition $\vec{K} \approx \vec{k}_{photon}$ then the exciton in the crystal can couple efficiently to the photons of *em* field and give light outside the crystal. Moreover in the case of wurtzite group III nitrides, when an exciton polariton propagate other than the [0001] direction, there are possible observations of some crystal orientation dependent effects linked to the birefringence of wurtzite structure.[10,16]

The luminescence property of a semiconductor material also can be affected by the presence of native defects, impurity, dopants and absorbed molecular species. In the case of a direct band gap semiconductor with low carrier density, the PL intensity can be expressed as,[10,16]

$$I_{PL} = (\hbar\omega_I - E_g)^{\frac{1}{2}} \exp\left(-\frac{\hbar\omega_I - E_g}{k_B T}\right) \qquad \ldots\ldots\ldots\ldots\ldots\ldots (2.15)$$

where the first term arises from the joint density of states in the interband transition and the second factor corresponding to the Boltzmann distribution of the e^-s and holes in the solid. The luminescence efficiency of direct band gap semiconductors is relatively higher compared to that of indirect band gap materials. The PL studies on AlGaN structures, reported in this thesis, are carried out using the same setup used for the micro–Raman measurements (inVia, Renishaw) (Fig. 2.9), by choosing the He–Cd laser source (325 nm), long pass filter for rejecting the source wavelength, 2400 gr.mm^{-1} grating and a CCD detector.

2.7 Scanning probe microscopy

2.7.1 Atomic force microscopy

The AFM is one of the members of SPM systems used for the study of topography related information of a sample with an order of atomic scale spatial resolution. The AFM probes consist with a sharp tip of the order of 100 Å used for probing the tip–sample interactions.[17] There are several interactions possible to contribute the deflection/natural frequency of an AFM cantilever. The common force associated with AFM interaction is inter atomic force called as the van der Waals force and it varies with distance between the tip and the sample (Fig. 2.11a). The three modes of operations, available in the AFM setup (contact, non–contact and intermittent), can be selected by choosing the three different regimes of forces between tip and sample.[17] The major components commonly involved in the SPM systems are shown (schematic, Fig. 2.11b)

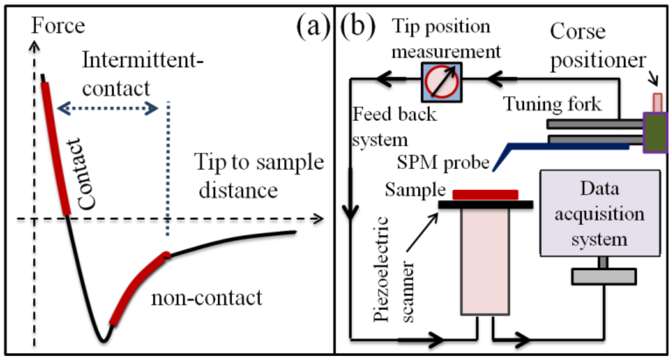

Figure 2.11 (a) Interaction force Vs distance between tip and sample. (b) Block diagram of general SPM system with major components.

The AFM used for the studies on AlGaN NWs, reported in the present thesis, is from a SPM system (Nanonics, MultiView 4000; Multiprobe imaging system). The MultiView 4000 uses normal force tuning fork technology with a high Q–factor and phase feedback to allow the control of probe/sample separation. Tuning forks in normal force mode with phase or amplitude feedback permit high performance and ease of operation for AFM imaging in intermittent mode. The AFM tips are glass–based probes. Unlike standard piezo scanners that keep probes separated, the 3D flat scanner with excellent AFM resolution, large vertical (axial) displacement of up to 100 μm for sample scanning and up to 30 μm for tip scanning, is used in this system.

2.7.2 Piezo–response force microscopy

In order to measure the piezoelectric properties of the ferroelectric or piezoelectric materials using contact mode PFM, a conductive AFM tip was employed. The schematic represents the PFM measurement set up (Fig. 2.12a). The working procedure of it includes two main steps. The first step is the polarization in a predefined area of the sample by using a DC bias voltage, and the second step is to detect the magnitude of the piezoelectric response by means of AC electric fields. In the second step, to detect the magnitude of the induced piezoelectric response, the AFM tip was connected to a lock–in amplifier with PFM configuration. An external DC (V_{dc}) bias and an AC voltage [$V_{ac}cos(\omega t)$] were then applied between the cantilever and the grounded substrate for activating the piezoelectric domains and probing the feedback, respectively. As a result, cantilever displacement occurs due to the piezoelectric effect as governed by the relations given below

$$V = V_{dc} + V_{ac}\cos(\omega t)\ ; \qquad \Delta Z = \Delta Z_{dc} + \Delta Z_{ac}\cos(\omega t + \varphi)\ \ldots\ldots\ldots\ldots\ldots..\ (2.15)$$

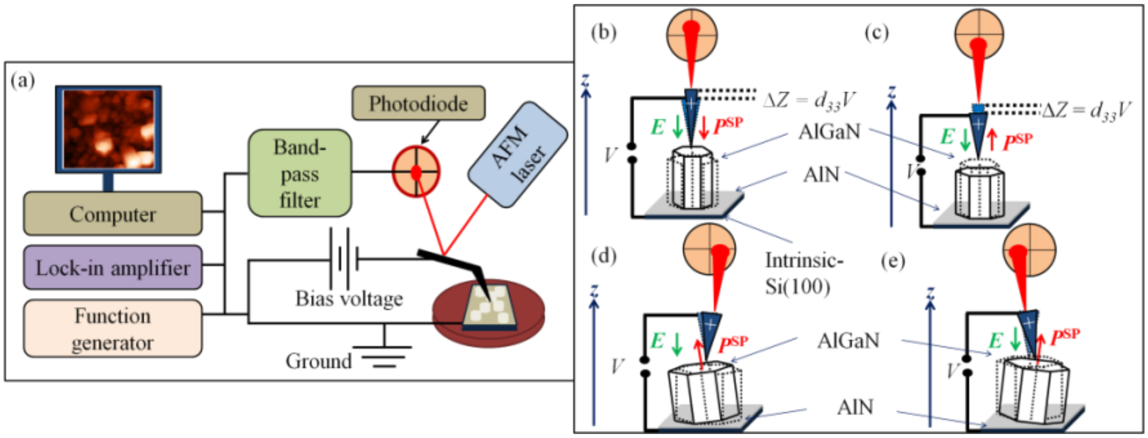

Figure 2.12 (a) The schematic representation of a typical PFM measurement setup. The different polarization configurations with respect to the crystalline orientations for (b) E parallel to P^{SP} (c) E anti–parallel to P^{SP} (d) and (e) E making an angle with P^{SP}.

By applying the voltage between the sample surface and the AFM tip, an external electric field was setup across the sample. The sample would locally enlarge or contract according to the electric field due to the electrostriction, as an 'inverse piezoelectric' effect. When the initial spontaneous polarization (P^{SP}) of the electrical domain of the measured sample is perpendicular to the sample surface, and parallel to the applied electric field (E); the domains experience a vertical expansion. Since the AFM tip is in contact with the sample surface, the increase in domain size bends the AFM cantilever and pushes it up. It results in the increase of tip deflection compared to the position before applying the electric field (Fig. 2.12b). On the contrary, when the domain contracts and it results in a decreased cantilever deflection if the initial domain polarization is anti–parallel to the applied electric field (Fig 2.12c). The magnitude of change in cantilever deflection, in such situation, is directly related to the amount of expansion or contraction of the sample electric domains, and hence it is proportional to the applied electric field.[18,19] Thus, the amplitude of the PFM response is proportional to the strength of the piezo–response and the phase signal is the representative of the polarization direction of the samples below the probe tip (Figs. 2.12d and 2.12e).

In the present study, a pre–defined 10 × 10 μm^2 area was selected for PFM imaging and an external bias voltage of +5 V and −5 V were applied between the tip and the bottom substrate. A diamond like carbon (DLC) coated stiff cantilever with a resonant frequency of 256 KHz and a stiffness constant of 11.5 $N{\cdot}m^{-1}$ was used as an AFM tip (with a cantilever dimension of 100 × 35 × 2 μm) in the contact mode for inducing the polarization in AlGaN microrods. The deformations in the crystal surfaces are detected by the AFM tip through the optical laser beam path and with the help of a four–quadrant photodetector. The lock–in amplifier deconvolutes the induced signal on the cantilever to measure the amplitude and phase difference (φ) with respect to the input AC voltage.

2.7.3 Near–field scanning optical microscopy

The near–field scanning optical microscopy (NSOM) or SNOM is a microscopic technique used to investigate the light–matter interaction of nanostructures in the sub diffraction regime by using the advantages of evanescent waves (or confined light) which surpass the conventional far–field resolution limit. The production of evanescent waves can be achieved with the help of either by plasmonics or by the use of sub–wavelength apertures coated with noble metals such as Au, Ag or combination of both. The evanescent waves emanated from the apertures/probe with higher momenta *i.e.*, lower wave lengths and velocities compared to that of normal light can be used for achieving the high resolution by placing the detector very close (near–field regime, smaller than wavelength λ) to the sample specimen surface. This allows us to record the light–matter interactions with high spatial, spectral and temporal resolution.[20,21] In this technique, the resolution of the image is determined by the size and geometry of the aperture probe and not by the λ of the excitation light. The NSOM provides simultaneous measurements of the topography and optoelectronic properties of nanostructures with high spatial resolution in the sub–wavelength regime. The detailed schematic of experimental set up used for recording the light–matter interaction of AlGaN single NW is shown (Fig. 2.13). The NSOM (MultiView 4000; Nanonics, Israel) imaging of nanostructures was used to understand the interaction with 532 nm laser (~ 2.33 eV).

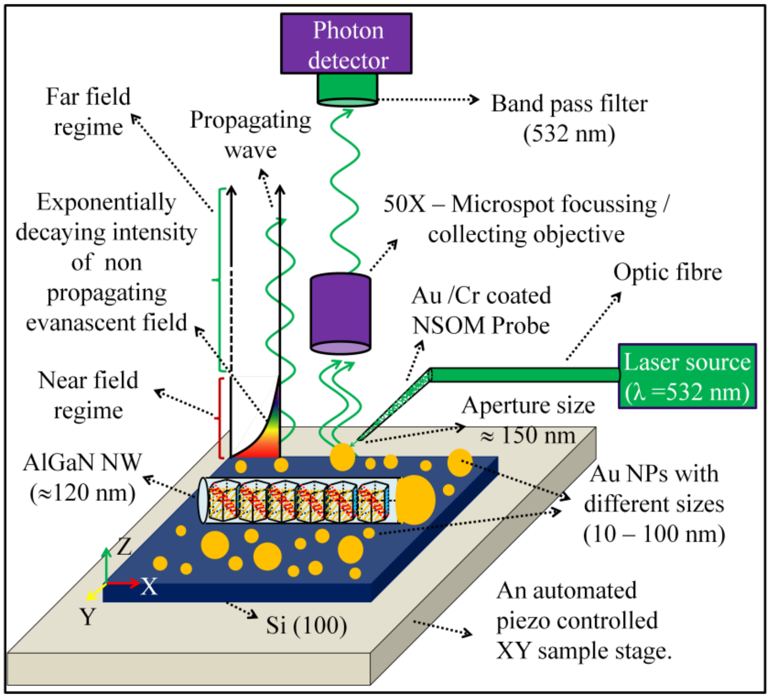

Figure 2.13 The schematic experimental setup for NSOM imaging of AlGaN NW and Au NPs with the near–field excitation and far–field collection configuration.

In order to perform an NSOM/SNOM experiment, with near–field excitation and far–field collection configuration (Fig. 2.13), a point light source emanated through the probe at the near–field regime would be scanned over the surface of the sample specimen with proper feedback and the propagating optical signal emitted from the sample surface due to the dipole radiation would be detected at the far–field. A band pass filter (532 nm) was employed to extract the excitation laser after the light–matter interaction and before reaching the light to the detector in the far–field configuration. We used an optical fiber with a circular aperture and metal (Au/Cr) coated probe with a tip apex (aperture) diameter of 150 nm for near–field excitation of laser light. The optical fiber coated with Cr and Au to avoid leakage of optical power, was used to enhance the optical transmission and confine the light to the sample surface. The scanning was performed either by using the NSOM probe or motorized XY sample stage with very precise special resolution controlled with the help of inbuilt sensors and piezo–drivers. The same probe was used as an AFM tip for simultaneous scanning to record topography along with the NSOM image of the sample with the tuning fork feedback mechanism. The major components commonly involved in the NSOM systems are shown (schematic, Fig. 2.13)

2.8 Summary

The APCVD, PAMBE and vacuum thermal evaporation systems, used for the growth of nanostructures, are described. The experimental techniques, utilized for the study of AlGaN nanostructures reported in this thesis, are also described briefly with the basic principle, major components of the apparatus, and their technical specifications with schematic or block diagrams.

2.9 References

[1] K. L. Chopra, *Thin film phenomena*, **1969**, 1st Ed., McGraw–Hill

[2] R. F. C. Farrow, *Molecular beam epitaxy: applications to key materials*, **1995**, Elsevier

[3] H. Morkoç, *Hand book of Nitride Semiconductors and Devices. Vol. 1. Materials Properties, Physics and Growth*, **2008**, WILEY–VCH Verlag GmbH & Co. KGaA, Weinheim, ISBN: 978–3–527–40837–5

[4] X. T. Yan and Y. Xu, *Chemical vapor deposition: an integrated engineering design for advanced materials*, **2010**, Springer Science & Business Media

[5] B. D. Cullity and S. R. Stock, *Elements of X–ray Diffraction*, **2001**, Prentice Hall, Upper Saddle River

[6] D. B. Williams and C. B. Carter, *Transmission electron microscopy: a textbook for materials science*, **2009**, 2nd Ed., Springer

[7] R. F. Egerton, *Electron energy–loss spectroscopy in the electron microscope*, **2011**, Springer Science & Business Media

[8] J.F. Watts and J. Wolstenholme, A*n introduction to surface analysis by XPS and AES*, **2003**, Wiley–VCH

[9] J. Ferraro, K. Nakamoto, C.W. Brown, *Introductory Raman spectroscopy*, **2003**, 2nd Ed., Academic Press, ISBN: 978–0–12–254105–6

[10] M. Fox, *Optical properties of Solid*, **2001**, Oxford University Press, New York, ISBN: 978–0–19–850613–3

[11] M. Cardona, *Light Scattering in Solids,* **1975**, Springer, Berlin, DOI:10.1007/978–3–540–37568–5

[12] P. Vandenabeele, *Practical Raman Spectroscopy: An Introduction*, **2013**, First Edition, John Wiley & Sons, Ltd.

[13] T. C. Damen, S.P.S. Porto, B. Tell, *Phys. Rev.* **1966**, 142, 570

[14] M. Tanaka and R. J. Young, *J. Mater. Sci.* **2006**, 41, 963

[15] P. Hendra, C. Jones, and G. Warnes, *Fourier Transform Raman Spectroscopy: Instrumentation and Chemical Applications*, **1991**, Ellis Horwood Ltd.: Chichester, England

[16] P.Y. Yu and M.Cardona, *Fundamentals of semiconductors*, **2010**, Springer–Verlag Berlin Heidelberg, DOI:10.1007/978–3–642–00710–1

[17] R. Howland, L. Benatar, *A Practical Guide: To Scanning Probe Microscopy*, **1998**, DIANE Publishing Company

[18] O. Ambacher, B. Foutz, J. Smart, J. Shealy, N. Weimann, K. Chu, M. Murphy, A. Sierakowski, W. Schaff, and L. Eastman, *J. Appl. Phys.* **2000**, 87, 334

[19] H. D. Espinosa, R. A. Bernal, and M. Minary–Jolandan, *Adv. Mater.* **2012**, 24, 4656

[20] A. Zayats and D. Richards, *Nano–Optics and Near–Field Optical Microscopy*, **2009**, ARTECH HOUSE, INC., ISBN–13: 978–1–59693–283–8

[21] L. Novotony and B. Hecht, *Principles of Nano–Optics*, **2006**, Cambridge University Press, New York, USA

CHAPTER 3

GROWTH OF AlGaN BY CHEMICAL VAPOR DEPOSITION TECHNIQUE

“*Building art is a synthesis of life in materialised form. We should try to bring in under the same hat not a splintered way of thinking, but all in harmony together*” ... Alvar Aalto

3.1 Introduction

The 1D NWs of AlGaN with high aspect ratio lead to strain relaxation without formation of dislocation in the material, which finds enormous utility in a variety of optoelectronics applications.[1-3] Along with NWs, the sub–micro and microstructures are also used for the development of room–temperature continuous wave emitters *via* high–Q whispering gallery modes (WGM) which are applicable for LDs.[1,3-5]

Therefore, by considering the importance of 1D III–nitride nanostructures, the present chapter describes the growth process of wurtzite AlGaN NWs with various size and shape using atmospheric pressure chemical vapor deposition (APCVD) technique *via* a vapor–liquid–solid (VLS) mechanism. The role of distribution in Au catalyst nanoparticles (NPs) on the size and shape of NWs is investigated. The optimization of flow rate for reactant gas (NH_3) and decomposition temperature on the morphology of NWs during the growth process are also discussed. Furthermore, the description of self–catalytic growth of NWs, as well as hexagonal shaped nano, sub–micro and microrods *via* a vapor–solid (VS) mechanism are included.

3.2 Vapor–liquid–solid mechanism: Growth of nanowires

The VLS growth mechanism,[6-10] involved in the present study is described as follows. The two independent zones of the reaction chamber were maintained at optimized temperatures of 1100 and 900 °C, respectively. The evaporation of Al and participation of Au as catalyst in the growth process took place in the respective subsequent reaction zones (Fig. 3.1).

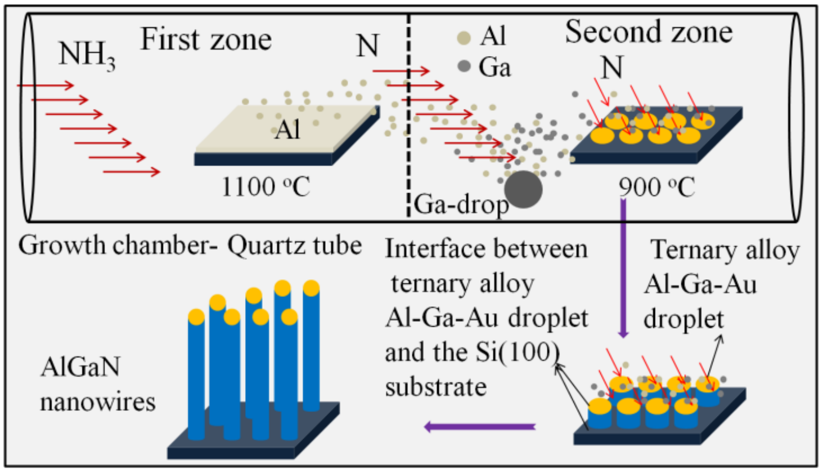

Figure 3.1 The schematic diagram for the Au catalytic VLS growth mechanism of the AlGaN NWs.

A thin film with an average Al metal thickness of 50–100 nm was used as the source for Al. The Au coated on Si(100) substrate was used as catalyst for the growth of NWs in the VLS process. The Ga precursor was also kept in the zone with a constant temperature maintained at 900 °C. At the optimized growth temperatures, the metallic Al evaporated from the first zone and Ga metal evaporated from the second zone interacted with molten Au catalyst NPs to form ternary liquid Al–Ga–Au alloy droplets. Similarly, the atomic N liberated from the decomposed NH_3 reacted with the constituent elements present in the ternary Al–Ga–Au liquid alloy leading to the phase formation of AlGaN.[6-10] Once the alloy system reached its solubility limit by N incorporation, the supersaturated AlGaN phase was precipitated at the interface of Au NP–Si(100) substrate driving the 1D growth of NWs.[6-10]

3.2.1 Effect of number density of Au NP catalyst in the VLS growth

The differences in morphology of NWs were achieved by varying the number density distribution of Au NPs on the Si(100) substrate. The subsequent morphological investigations of different types of as–grown NWs are shown in the figure 3.2. Well dispersed sample (Fig. 3.2a), was synthesized on Si(100) substrate with Au catalysts coated with an evaporation time of 5 min. Moreover, a uniform size with an average diameter of 100(±10) nm was also observed for the NWs. The mono–dispersed NWs with smooth morphology are spread all over the substrate and the size of the Au catalysts NPs is marginally higher than the diameter of the NWs (outsets of Fig. 3.2a). Furthermore, the Au NPs which took part in the VLS growth process of the NWs were well separated and were having a uniform size of ~120 nm. However, some of the Au NPs with smaller diameters did not participate in the VLS growth process (outsets of Fig. 3.2a). The low magnification image of the NWs synthesized on Si(100) substrate with Au catalysts coated with an evaporation time of 10 min is shown in the figure 3.2b. The dense and non–uniform size distributions of NWs are clearly observed all over the substrate. The high resolution image of the non–uniform NWs with diameters in the range of 50–150 nm is shown at the outsets of figure 3.2b. Moreover, a dense distribution of Au catalyst NPs with diameters in the range of 10–100 nm, used for the VLS growth of AlGaN NWs, is shown in the inset of one of the magnified FESEM images. It is obvious that all the Au catalyst NPs participated in the growth process leading to the dense distribution of NWs all over the Si(100) substrate. Furthermore, NWs were found to grow with triangular shape in cross–section. The high resolution FESEM images of the NWs show very smooth surface morphology with Au catalyst NP at the tip. The size of the triangular shaped NWs is higher than the size of the Au NPs observed at the tip.

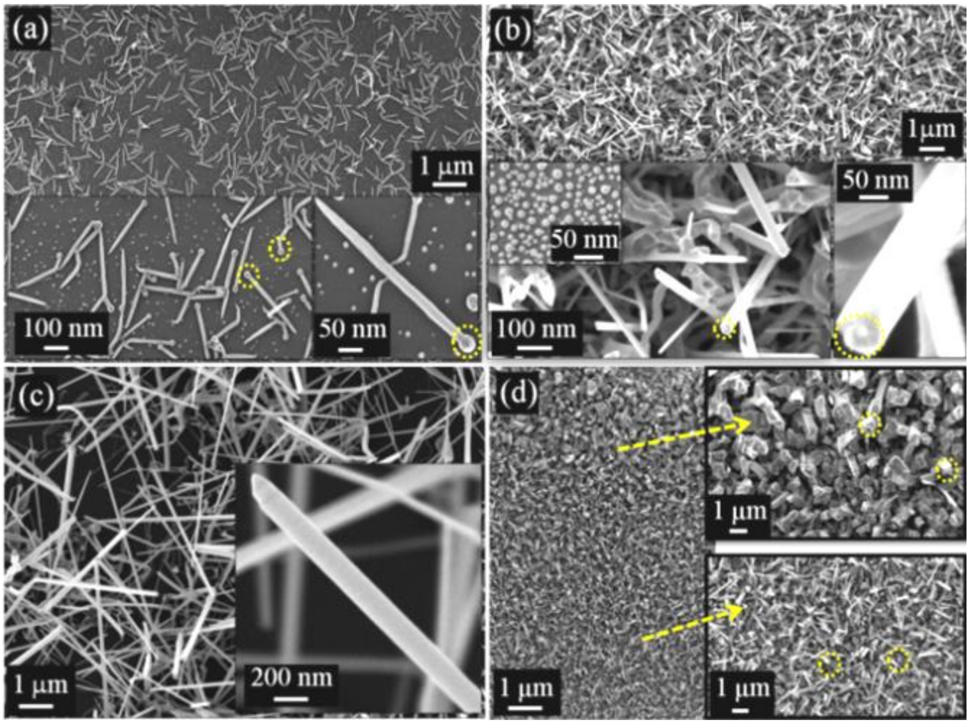

Figure 3.2 NWs synthesized with Au catalysts coated on Si(100) substrate with an evaporation time of (a) 5 min, the outsets showing high resolution images of the cylindrically shaped NW with Au NP at the tip of the NW as indicated by dotted circles. Along with these NWs, size of the Au NPs visible in this high resolution image itself. (b) 10 min, the outsets showing high resolution images of the triangular shaped NW with Au NP at the tip of the NW as indicated by dotted circles. The size and shape of the Au NPs also shown in the inset of one of the high resolution images. The NWs synthesized with Au CNPs as catalysts coated on Si(100) substrate (c) uniformly distributed Au CNPs, inset showing the high magnification image of NW with triangular shape (d) A gradient of distribution of Au CNPs leading to the distribution of NWs in the same substrate from nearly cylindrical shape to triangular ones. Outsets showing the high resolution images for the NWs from different regions of the substrate (as indicated by arrows) – triangular and cylindrically shaped NWs with Au NPs observed at the tip indicated by dotted circles.

The NWs synthesized with the help of uniformly dispersed Au colloidal NPs (CNPs, 20 nm) as catalyst particle is shown in the figure 3.2c. The inset figure shows the high magnification images of triangular shaped NW with diameters in the range of 50–150 nm. Moreover, in order to understand the dependence of size and shape of NWs with respect to the arrangement of Au catalyst CNPs over the substrate, we made a gradient of the distribution of CNPs from low to dense on the same Si(100) substrate. This was achieved by the drop casting of uniform Au CNPs (20 nm) dispersed in the water medium on the Si(100) and subsequent infra–red lamp heating to evaporate the water. Furthermore, in order to achieve the gradient in the number density of Au CNPs, the substrate is slightly tilted while drop casting. Subsequently, the Au CNPs drop casted on Si(100) substrate was used for the VLS growth of NWs. The growth led to the formation of NWs with different size and shape in the same substrate (Fig. 3.2d). We observed a gradient of size and shape distribution of NWs from cylindrical (lower part) to triangular (upper part) shapes. The high resolution FESEM images (outsets Fig. 3.2d) show triangularly shaped and almost cylindrical shaped NWs with circular cross section conceived from upper and lower portions of the substrate, respectively as indicated by dashed arrows in figure 3.2d.

The size and shape of the 1D NWs are determined by the size of the catalyst NPs used for the VLS growth purpose. Thermodynamically, the minimum radius required for a liquid Au catalyst droplet to form a eutectic alloy is,[6,10]

$$R_m = \frac{2V_l}{RT\ln(S)}\sigma_{lv} \quad \text{……………………………………(3.1)}$$

where V_l is the molar volume of the droplet, σ_{lv} is the liquid–vapor surface energy, and S is the degree of supersaturation of the vapor. Thus, a higher degree of supersaturation of atomic N, which is energetically difficult to achieve in practical purpose, is required for smaller catalyst sizes. The chemical potential of the constituents in the metal–alloy catalyst turn out to be high, as the size of the catalyst NPs diminishes due to the Gibbs–Thompson effect:[6,10]

$$\Delta\mu = \frac{2\gamma}{r} \quad \text{…………...…………………………(3.2)}$$

where $\Delta\mu$ is the chemical potential difference of the component species in the liquid droplet, γ is the surface energy, and r is the radius of curvature of the droplet. The Gibbs–Thompson effect predicts that the reduction of the size of Au NPs increases the difficulty in dissolving of vapor particles in the molten Au droplet to form a eutectic alloy.[6,10] Hence, it will increase the degree of complexity to achieve supersaturation states that adequately promote the growth of NWs. Ostwald ripening occurs between NPs at high temperature because of the bigger particles are energetically favorable. In other words, if the temperature is high enough to stimulate the diffusion of metal components then Ostwald ripening is a spontaneous process such that NPs tends to transform into large particles to achieve a lower energy state. The presence of Ostwald ripening leads to the development of metal catalyst droplets, which may take part in the growth of 1D structures.[6-10] Thus, the probability of agglomeration of Au NPs at high temperature are very high for the second (10 min deposited) sample with higher Au thickness as compared to that of the first (5 min deposited) case. Therefore, the second sample leads to the dense distribution of the NWs with almost all NPs participating in the VLS growth mechanism. Whereas, in the case of the first sample, the number density of Au NPs is low and therefore the possibility of Ostwald ripening is very limited. Therefore, it leads to the formation of uniformly distributed NWs with almost similar sizes and shape. Furthermore, the growth of NWs with a uniform radius is associated with a steady state growth, in which material vapors are transported to the Au NP–NW interface.[6-10] Consequently, an evolution of constant NW diameter is possible, if the incorporation of material in the vapor phase is directed exclusively on the Au NP–NW interface where incorporation from the sidewalls is prohibited. However, the catalyst particle may be able to affect the size of NW either by matching of the size of NW or else by some mechanism involving the curvature of the particle, in which strain and lattice matching play a role.[6-10] In the case of the third set of samples with Au CNPs (Figs. 3.2c and 3.2d), we made a gradient of Au NPs distribution in such a way that almost all catalyst NPs participated in the growth process leading to the formation of NWs with different diameters. The Au NPs are likely to form smaller size in the area with a lower number density than that for the area with higher number density. Consequently, the shape of the NWs varies from circular to triangular in cross–section for NWs grown with small to large diameter of Au NPs, respectively (Fig. 3.2d). Therefore, it is very important that the Au metal NPs have to be carefully aligned and separated from each other during the preparation of substrates before heating in the furnace for the growth of 1D nanostructure.

3.2.1.1 Single–prong growth mechanism: Mono–dispersed and cylindrical NWs

In order to understand the uniformity in size and controlling the density of NWs, there are two major types of VLS growth kinetics which can be envisaged. The first one is single–prong growth mechanism to control the uniformity in the growth of 1D NWs (Fig. 3.3).[8,10]

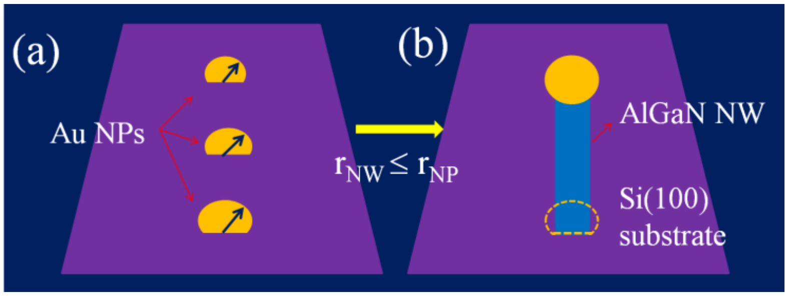

Figure 3.3 Schematic of single–prong growth mechanisms (a) before and (a) after growth

In the single–prong growth, there is a one–to–one correspondence between Au NPs and NWs. Moreover, the radius of the NW (r_{NW}) is usually observed (Fig. 3.3) to be almost equal or marginally smaller than the radius of the catalytic Au NPs (r_{NP}) participated in the initial growth process. Therefore, a single–prong growth mechanism can be envisaged for the case of the first sample (dispersed NWs) with $r_{NW} \leq r_{NP}$ (outsets of Fig. 3.2a).

3.2.1.2 Multi–prong growth mechanism: Ensemble of triangular NWs

In another model, a multi–prong growth mechanism is invoked where growth density of the NWs can be understood. In the multi–prong growth, more than one NW grows from a single catalyst particle.[8,10] Since NWs with comparatively smaller size are growing from a single bigger sized Au NP, the size of the individual NWs will be less than the size of the initial catalyst NP, i.e., $r_{NW} < r_{NP}$. However, after the complete growth process, it is possible to observe the distribution of NWs with smaller sized Au NPs at the tip compared to the individual NW (Fig. 3.4). In multi–prong growth process, r_{NW} is not determined directly by $r_{NP,}$ however it may be related to other structural factors such as the curvature of the growth interface and lattice matching between the Au catalytic NPs and the NW due to localized stress.[8,10] The FESEM image for the second sample (outsets of Fig. 3.2b) shows that the NWs are grown with triangular shape with $r_{NW} > r_{NP}$, indicating a multi–prong VLS growth mechanism.

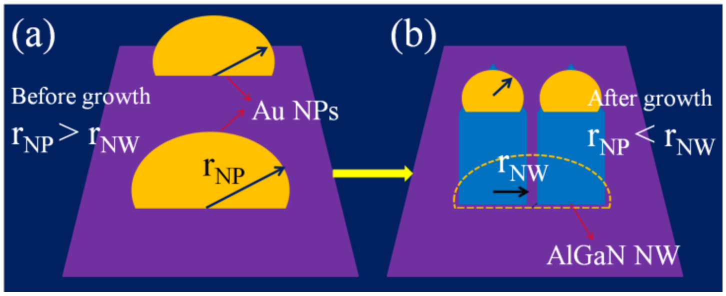

Figure 3.4 Schematic of multi–prong growth mechanisms (a) before and (b) after growth.

The sample grown with graded Au NP number density again confirms that the lower portion of the sample follows single–prong growth mechanism with cylindrical NWs (outset of Fig. 3.2d). On the other hand the upper layer follows the combination of single–prong and multi–prong growth mechanism leading to the triangular shaped dense NWs (outset of Fig. 3.2d). Thus, the size and shape of the 1D NWs are determined by the size of the catalyst NPs as well as the curvature of the Au NPs participated in the growth process. The bigger sized Au NP participated in the multi–prong mechanism leads to the triangular shaped NWs. Whereas Au NPs participated in the single–prong mechanism leading to the cylindrical NWs.

3.2.2 Growth of AlGaN NWs with the Al+Ga thin film as a precursor for Al

The morphological analysis of as–grown NWs *via* Au catalyst assisted VLS growth mechanism with Al+Ga thin film (50–100 nm) as a precursor for Al are shown (Fig. 3.5). Essentially, two types of samples were prepared using Au NPs (10 min evaporation time) and Au CNPs (20 nm) as catalysts and were shown for its surface morphology in a set of figures 3.5a–c and 3.5d–f, respectively.

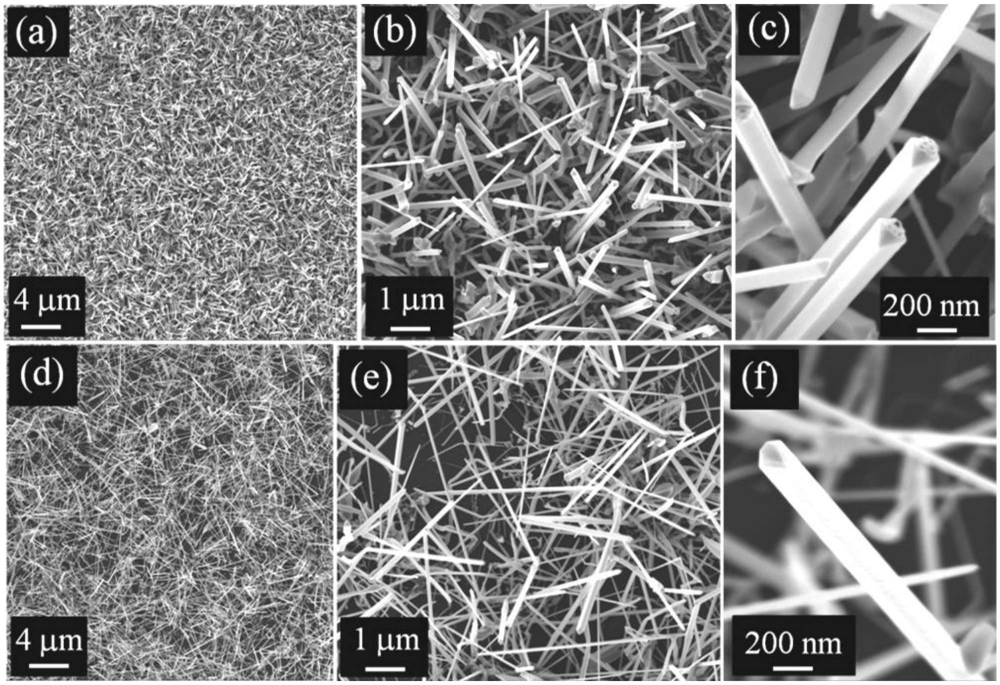

Figure 3.5 The low, medium and high magnification FESEM images of NWs *via* catalyst assisted VLS growth mechanism with Al+Ga thin film (50–100 nm) as a precursor for Al. Images of NWs synthesized with (a)–(c) Au NPs (10 min evaporation time) and (d)–(f) Au CNP (20 nm).

The FESEM analysis of NWs synthesized using Au NPs shows the distribution with high number density (Fig. 3.5a), lengths in the range of 2–4 μm (Fig. 3.5b) and triangular shape with sizes in the range of 120–150 nm (Fig. 3.5c), which are similar to the NWs grown with the Al thin film used as a precursor for Al (Fig. 3.2b). The aspect ratios of NWs, grown with the help of Au NPs, are found to vary in between the values of 16–27. Similarly, The FESEM images of the NWs synthesized with the help of Au CNPs shows the distribution of NWs with a number density slightly different from the previous case (Fig. 3.5d), the lengths in the range of 3–6 µm (Fig. 3.5e), and well faceted triangular shape with diameters in the range of 100–120 nm (Fig. 3.5f). The average aspect ratios of NWs, grown with the help of Au CNPs (20 nm), can be found to vary in between the values of 30–50. However, the morphological observations of the samples are similar to the NWs grown with the Al thin film used as a precursor for Al (Figs. 3.2c and 3.2d).

3.2.3 Optimization of NH_3 flow conditions in AlGaN NW growth

3.2.3.1 Effect of NH_3 flow rate

The morphological analysis of as–grown samples synthesized *via* Au catalyst assisted VLS growth mechanism with Al thin film (50–100 nm) as a precursor for Al along with different NH_3 gas flow rate are shown in the figure 3.6. Essentially, three types of samples were prepared by varying three different NH_3 flow rates of 30, 50 and 70 sccm. The FESEM analysis of sample grown with a NH_3 flow rate of 30 sccm shows (Fig. 3.6a) that the Si(100) substrate is coated with random islands of microstructures and there is no signature of the NW formation in the sample. Whereas, in the case of sample grown with a NH_3 flow rate of 50 sccm shows the high dense and uniform distribution of NWs all over the substrate (Fig. 3.6b). However, the ensemble of NWs contains a mixture of cylindrical as well as triangular shaped 1D structure (Fig. 3.6b) with diameters in the range of 150–200 nm (inset Fig. 3.6b).

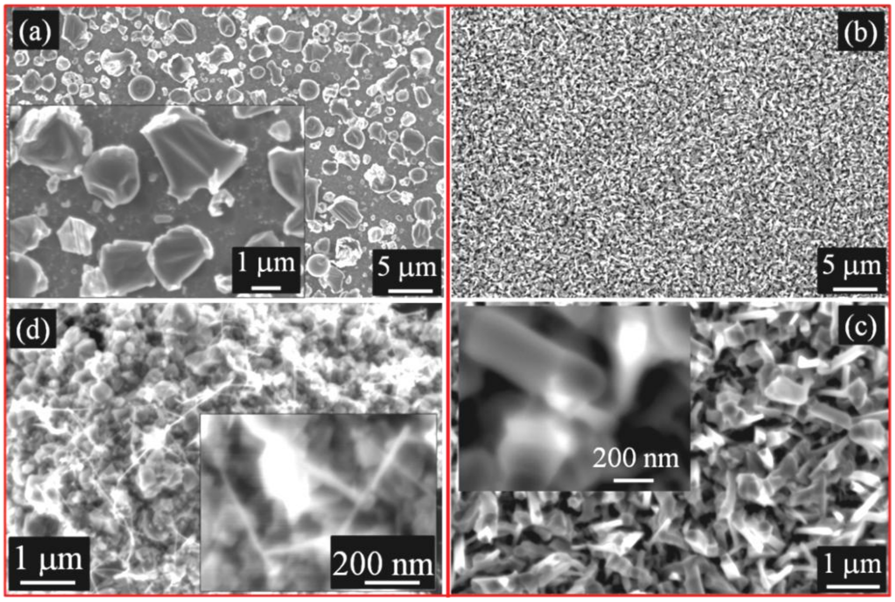

Figure 3.6 The morphology of samples grown with different NH_3 flow rates (a) 30 sccm, islands of microstructures, inset showing the high magnification images of microstructures (b) 50 sccm, low magnification image of an ensemble of NWs with high number density (c) High magnification image of the same sample with cylindrical and triangular NWs, the inset figure showing the higher magnification image of NW (d) 70 sccm, cluster of microstructures along with NWs, inset showing the high magnification images of microstructures with NWs lying over it.

Moreover, the irregular microstructures as well as deterioration in the number density of NW formation (Fig. 3.6c) are observed in the sample grown at a high NH_3 flow rate of 70 sccm. Therefore, the NH_3 gas flow rate suitable for 1D NW growth is optimized as 50 sccm.

3.2.3.2 Effect of NH_3 cracking temperature

The morphological features of samples synthesized by the VLS growth mechanism with different NH_3 gas cracking temperature are shown in the figure 3.7. The experiments were carried out for four different on–set temperatures for the NH_3 gas flow at 700, 750, 800 and 850 ^{o}C. The FESEM analysis of sample grown with a NH_3 flow started at 700 ^{o}C (Fig. 3.7a) shows that the substrate is completely covered with spaghetti like NWs. The inset of figure 3.7a shows NWs possessing a cylindrical shape with diameters in the range of 50–70 nm. The sample grown with a NH_3 flow started at 750 ^oC (Fig. 3.7b) shows dense distribution of NWs with circular cross section and diameters in the range of 100–120 nm (inset Fig. 3.7b) all over Si(100) substrate.

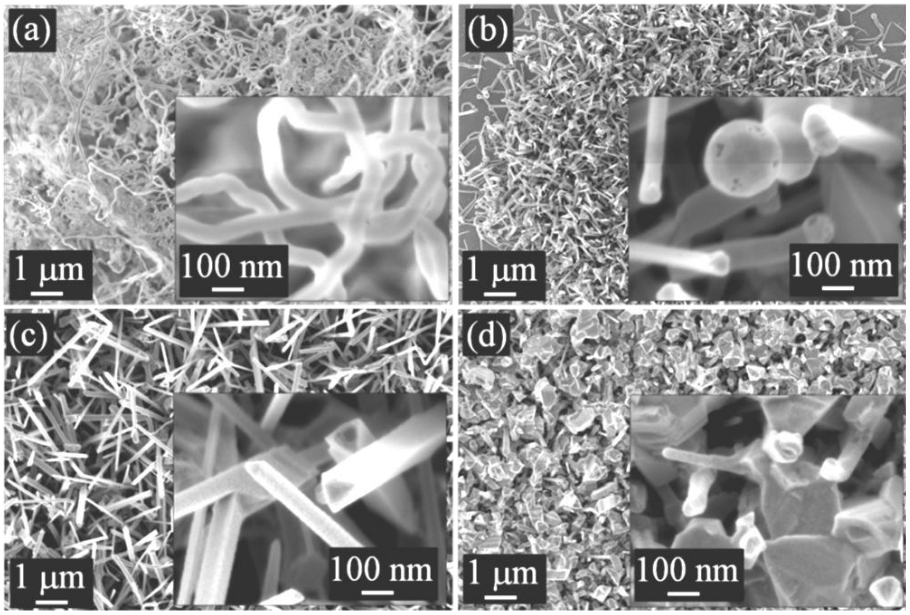

Figure 3.7 The 1D nanostructures grown with different starting temperature of the NH_3 gas flow for (a) 700 ^oC, spaghetti like NWs (b) 750 ^oC, with high number density and cylindrically shaped NWs (c) 800 ^oC, with high number density and triangular shaped NWs (d) 850 ^oC, cluster of nanostructures with different shapes. Inset of all the figures showing the high magnification images of nanostructures.

Interestingly, the shape of NW transformed from circular (Fig. 3.7b) to triangular (Fig. 3.7c) in shape, while changing the NH_3 flow starting temperature from 750 to 800 ^oC. Moreover, the inset figure 3.7c shows the well faceted and triangular in cross–section of NW with diameters in the range of 100–150 nm. Whereas, the last sample synthesized with 850 ^oC, as a starting temperature for the NH_3 flow, shows an ensemble of NWs containing a mixture of different shapes including triangular and hexagonal (Fig. 3.7d) 1D structures with diameters in the range of 150–200 nm (inset Fig. 3.7d). Therefore, in the present study, the starting temperature for the NH_3 gas flow, appropriate for 1D NW growth is optimized as 750 and 800 ^oC for cylindrical and triangular NWs, respectively.

3.2.4 Structural analysis: Transmission electron microscopy

A typical cylindrically shaped NW from the mono–dispersed sample with a diameter of 100(±10) nm (Fig. 3.8a) is used for the structural analysis. The HRTEM image (Fig. 3.8b) is analyzed to show the interplanar spacing of 2.78 Å, which corresponds to *m*–plane (1-100) of the wurtzite phase indicating the growth direction of the single crystalline GaN (JCPDS # 00–050–0792) NW along *m*–plane [1-100].

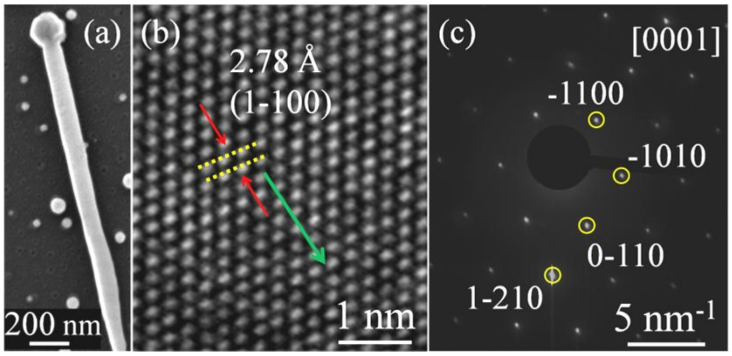

Figure 3.8 (a) A low magnification FESEM image of typical mono–dispersed NW used for TEM analysis. (b) SAED pattern of NW indexed to the wurtzite phase of AlGaN with zone axis along [0001]. (c) HRTEM image of the AlGaN NW showing the growth direction along [1-100].

The SAED pattern (Fig. 3.8c) is indexed to the wurtzite phase of crystalline GaN with zone axes along [0001].

Similarly, a typical low magnification TEM micrograph is shown (Fig. 3.9a) for a triangular shaped single NW. The SAED pattern of the triangular NW (Fig. 3.9b) is also indexed to wurtzite phase of single crystal GaN with zone axes along [0001]. HRTEM image (Fig. 3.9c) shows interplanar spacing of 2.76 Å corresponding to (1-100) *m*–planes of GaN. Moreover, the inverse fast Fourier transformed (IFFT) image (Fig. 3.9d) of the selected area (squared) of the HRTEM image (Fig. 3.9c) also shows an interplanar spacing of 2.76Å indicating the growth direction of the NW along [1-100], which is normal to the non–polar *m*–plane of wurtzite GaN. A HRTEM image of Au NP–NW interface is also shown (Fig. 3.9e).

An interplanar spacing of 2.37 Å, observed for the NP, corresponds to (111) plane of cubic Au phase. Similarly, in the case of NW region, it shows an interplanar spacing of 2.77 Å corresponding to (10-10) of GaN (JCPDS # 00–050–0792).

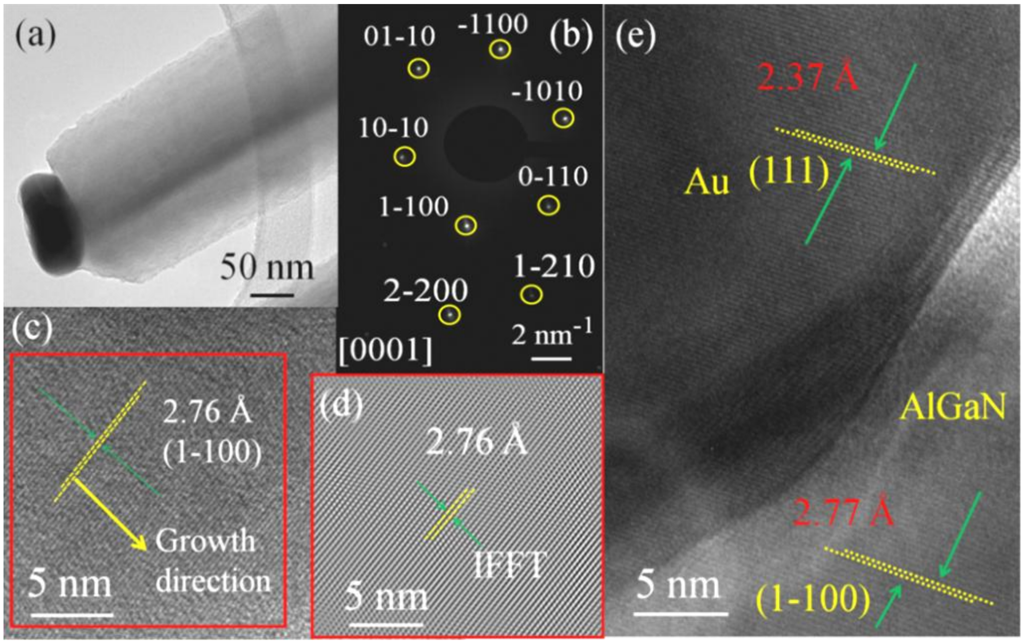

Figure 3.9 (a) A low magnification TEM image of a typical triangular shaped NW. (b) SAED pattern of the NW indexed to the wurtzite phase of AlGaN with zone axis along [0001]. (c) HRTEM image of the AlGaN NW showing the growth direction along [1-100]. **(**d) IFFT image of the selected (squared) portion of the HRTEM image. (e) The HRTEM image of Au NP–AlGaN NW interface.

Therefore, the structural analysis confirms presence of wurtzite GaN phase along with the involvement of Au NPs in the VLS growth process of NWs. Moreover, the crystallographic orientation and growth direction of cylindrical as well as triangular NWs are similar to each other irrespective of its surface morphology.

3.2.5 Elemental analysis: Electron energy loss spectroscopy

In order to confirm the existence of Al in the as–grown AlGaN NWs, we recorded EELS spectra to detect the presence and distribution of atomic Al along the NW. Since the percentage of Al incorporated in the AlGaN NW is very less compared to other two components of Ga and N, the typical Al–*K* edge spectrum (Fig. 3.10a) collected from single AlGaN NW shows very low intensity. The Ga–$L_{2,3}$ and N–*K* edges are shown in figures 3.10b and 3.10c, respectively.

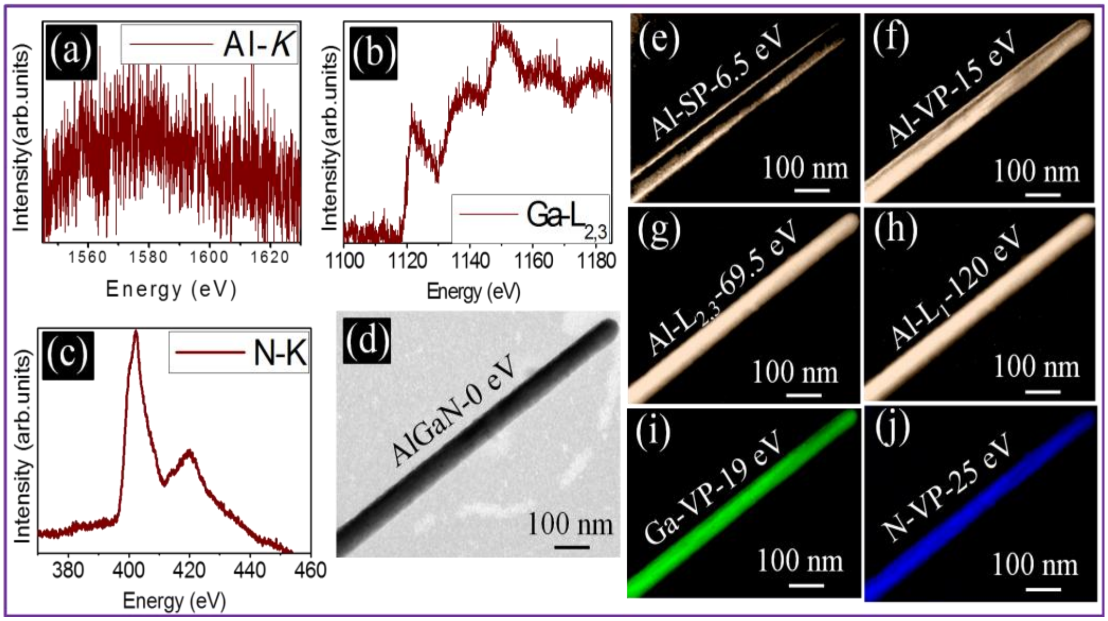

Figure 3.10 EELS spectra collected from single typical AlGaN NW for (a) Al–*K* (b) Ga–$L_{2,3}$ (c) N–*K* edges. The EFTEM images of the same AlGaN NW for (d) the zero loss. (e) 6.5 eV corresponding to SP energy of Al. (f) 15 eV corresponding to the VP energy of the Al (g) 69.5 eV corresponding to the $L_{2,3}$ edge of Al. (h) 120 eV corresponding to the L_1 edge of Al. (i) 19 eV corresponding to the VP of Ga. (j) 25 eV corresponding to the VP of N. The pseudo colors depicted in the EFTEM image chosen for describing the presence of different elements of Al (golden), Ga (green) and N (blue) in the NW.

Apart from EELS study, the energy filtered transmission electron microscopy (EFTEM) measurements were performed for further confirmation of Al in the NWs. Figure 3.10d (gray color) depicts the typical zero–loss EFTEM image of AlGaN. Using the EFTEM technique, the successive images of NW recorded for surface plasmon (SP), volume plasmon (VP), $L_{2,3}$ edge, and L_1 edge of the elemental Al and the corresponding images with golden pseudo color are represented in the figures 3.10e–h, respectively showing uniform distribution of Al. In the similar way, figure 3.10i represents the EFTEM image (green pseudo color) for energy of 19 eV corresponding to the VP of the Ga. Finally, figure 3.10j represents EFTEM image with blue pseudo color for an energy 25 eV corresponding to the VP of the N. Therefore, the EFTEM imaging study of AlGaN NW is an additional confirmation for the presence of Al in sample grown in the VLS assisted APCVD technique.

3.2.6 Optical properties of ensembled NWs

3.2.6.1 Vibrational properties: Raman spectroscopy

A typical Raman spectrum for the ensemble of mono–dispersed AlGaN NWs is shown in the figure 3.11. The first–order phonon Raman scattering is caused by phonons with wave vector $k \sim 0$ (Γ point) because of a momentum conservation rule in the light scattering process. There are six optical modes of A_1(TO), A_1(LO), E_1(TO), E_1(LO), E_2^L and E_2^H, which can be active in the first–order Raman scattering of wurtzite structured polar materials.[10-13] Essentially, the different modes observed for an ensemble of VLS grown mono–dispersed NWs are centered at the peak positions of around 140, 255, 420, 535, 558, 567, 668, 724 and 745 cm^{-1} (Fig. 3.11a). The corresponding symmetry assignments for observed modes are tabulated (Table 3.1).

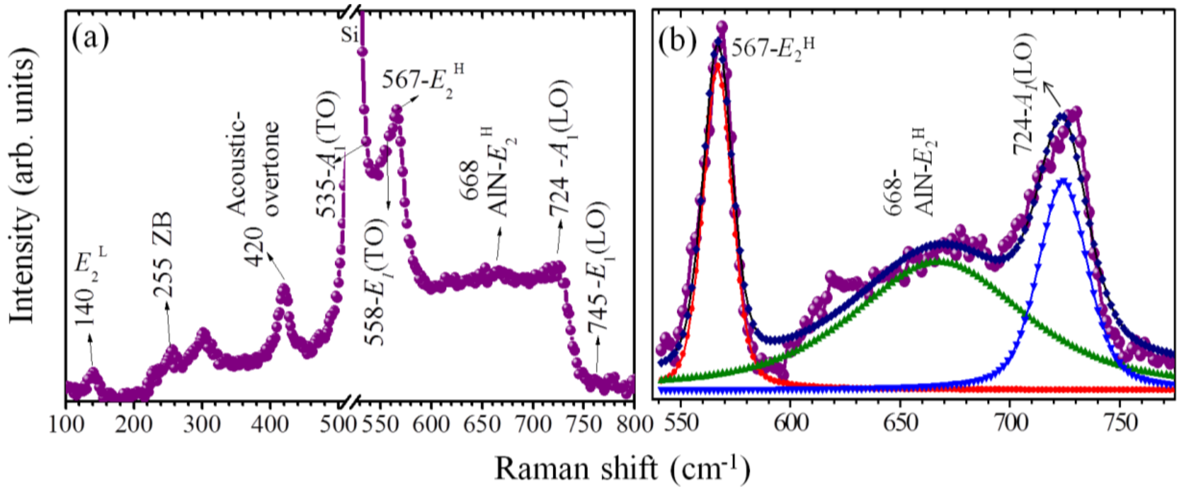

Figure 3.11 The observed Raman spectra for (a) An ensemble of mono–dispersed AlGaN NWs (b) Lorentzian fitted peaks in between the regions 540–775 cm^{-1}.

It is reported that the Raman A_1(TO), E_1(TO), E_2^L and E_2^H phonon modes obey two–mode behavior of random alloy, meanwhile the E_1(LO) and A_1(LO) modes follow the one–mode phonon behavior.[10-13] However, the presence of E_2^H modes (E_2 symmetry) of GaN and AlN at ~567 and ~668 cm^{-1}, respectively in the same Raman spectrum (Fig. 3.11b) shows the two–mode behavior of random alloy. It confirms again the presence of Al in the as–prepared NWs and it supports strongly the EFTEM analysis carried out for the presence of Al in the AlGaN NWs (Fig. 3.10e–h). All other modes, appeared in the Raman spectrum (Fig. 3.11a), correspond to the assigned modes of GaN in the wurtzite phase for the as–prepared sample. The vibrational modes for all other samples synthesized using the VLS growth mechanism, as discussed earlier, also showed very similar Raman modes (not shown in figure).

Table 3.1: Assignments of various phonon modes in the ensemble of mono–dispersed NWs

AlGaN Raman shift (cm^{-1})	**Symmetry Assignments**
140	GaN– E_2^L ; with E_2 symmetry[10-15]
255	GaN–Zone boundary phonon[10-15]
420	GaN–Acoustic overtone[10-15]
535	GaN–A_1(TO) ; with A_1 symmetry[10-15]
558	GaN–E_1(TO)[10-15]
567	GaN– E_2^H [10-15]
668	AlN– E_2^H [10-15]
724	GaN–A_1(LO) [10-15]
745	GaN–E_1(LO) [10-16] (reported to be weak)[16]

3.2.6.2 Luminescence properties: Photoluminescence spectroscopy

An excitation source of UV–laser with a wavelength of 325 nm is used to excite the ensemble of AlGaN NWs. The PL emission spectrum, recorded at room temperature (300 K), is shown for the ensemble of mono–dispersed NWs (Fig. 3.12). On deconvolution, different Gaussian peaks centered at 3.55, 3.49, 3.38, 3.29 and 3.19 eV are observed in the PL spectrum. The band edge peak centered at ~3.55 eV is due to the recombination of free excitons and is found to be blue shifted from the reported value of ~3.47 eV at 300K for GaN.[17] All other peaks are assigned to bound excitons and native defects and are tabulated (Table 3.2). The PL emissions with similar features were also observed for all other VLS grown samples of AlGaN NWs, as discussed in the earlier sections.

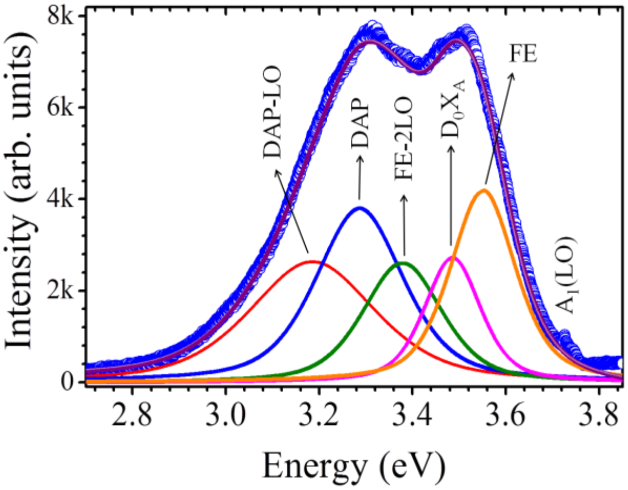

Figure 3.12 Photoluminescence spectrum observed for an ensemble of mono–dispersed AlGaN NWs

Along with the above emission peaks, a peak centered at ~3.73 eV is assigned to A_1(LO) phonon mode of GaN.[10,17-20] The three major factors affecting the blue shift in the band gap of the semiconductor nanomaterials are quantum confinement effect,[21] lowering of the temperature of the material,[22] and alloying with appropriate elements.[2,23,24]

Table 3.2: Assignments of PL peaks in the ensemble of mono–dispersed NWs

Energy (eV)	Symbols	Remarks
3.53–3.55	FE	Free exciton emission for as–prepared AlGaN NW sample arising because of the recombination of electron–hole pair from conduction band minimum to valence–band maximum.[10,17-19]
3.49	D^0X_A	Emission due to recombination of exciton bound to neutral donors. The possible neutral donors being the impurities (Al) forming stable complexes with nitrogen vacancy (V_N) (i.e. Al–V_N).[10,17-19]
3.38	FE–2LO	Free exciton–second order LO phonon coupling arising due to the Fröhlich interactions.[10,17-19]
3.29–3.33	DAP	The recombination of the neutral donor–acceptor pair (DAP; D^0A^0), due to a transition from a shallow donor state of V_N to a deep acceptor state of V_{Ga}. As compared to the V_{Ga}, the V_{Ga}–O_N complex is more stable.[10,17-19]
3.19–3.23	DAP–LO	The phonon replica of neutral donor–acceptor pair observed because of the interaction between first order A_1(LO) phonon with electron present in the DAP.[10,17-19]

It is reported that the exciton Bohr radius for GaN is 11 nm,[25] therefore the role of quantum confinement effect in elevating the band gap for as–prepared AlGaN NWs to ~3.55 eV with diameters in the range of 50–100 nm can be ruled out. The reported band gap of GaN is 3.503 eV at 0 K.[22,23] Thus, the free exciton emission at ~3.55 eV strongly confirms the presence of Al in the as–prepared NW sample (Fig. 3.12). Moreover, the approximate atomic percentage of Al is calculated ([E_g(AlGaN) – E_g(GaN)] / [E_g(AlN) – E_g(GaN)]; where E_g(AlN) ~6.2 and E_g(GaN) ~3.47 eV are the reported and E_g(AlGaN) ~3.55 eV is experimentally observed band gap values at room temperature) as ~3.0% from the band bowing formalism by neglecting the value of *b* in the low doping limit.

3.3 Self–catalytic vapor–solid mechanism

The growth process of AlGaN microrods involves a self–catalytic VS mechanism[6,13] including two concomitant steps, as follows. In the first step, the Al thin film, coated on the intrinsic Si(100) or *c*–sapphire substrates, may react with atomic N at 1100 °C to form very thin AlN islands (base layer), which may act as reactive seeds for promoting the growth process.[6,13,26-28] In the second step, the un–reacted portions in the Al thin film supply the atomic Al for the further growth process. The proposed growth mechanism for AlGaN crystallites *via* VS growth process is depicted schematically in the figure 3.13.

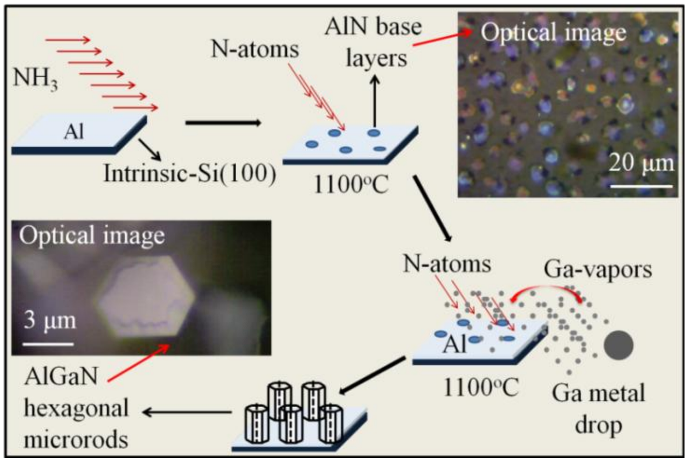

Figure 3.13 The schematic growth process of AlGaN microrods in self–catalytic VS mechanism.

The Ga metal precursor as well as the Al thin film was kept in the single zone furnace at an optimized growth temperature of 1100 °C and the ultra high pure NH_3 with a constant flow rate of 50 sccm was allowed to flow in to the reaction chamber. At this temperature, the high pure NH_3 was decomposed to form reactive atomic N and H (vapor phase). Consequently, the atomic N reacts to some portions on the surface layers of Al thin film and forms a few islands of the AlN base layers over the substrates.[13] The optical image of such AlN base layer is shown in the right top inset of figure 3.13. Continued supply of the metallic Ga vapors and the evaporated Al from the un–reacted portions of the thin film, lead to the further growth process of AlGaN microrods (solid phase) without the aid of any metallic catalytic particles.[6,13,26-28] The optical image of the as–grown AlGaN microrod is also shown in the left bottom inset of figure 3.13. Therefore, the AlGaN microrods grown on the substrate *via* a VS growth mechanism can appear to be well separated and may possess AlN islands as a base layer.[6,13,26-28]

3.3.1 Growth of AlGaN on Al thin film: Hexagonal–crystallites

3.3.1.1 Influence of substrate: Si(100) and *c*–sapphire

The morphological features of samples prepared on the Al (50–100 nm) coated substrates are shown (Fig. 3.14). The sub–micro sized crystallite with distinct separations, grown on Al (50–100 nm) coated Si(100) substrate, are shown in the figure 3.14a.

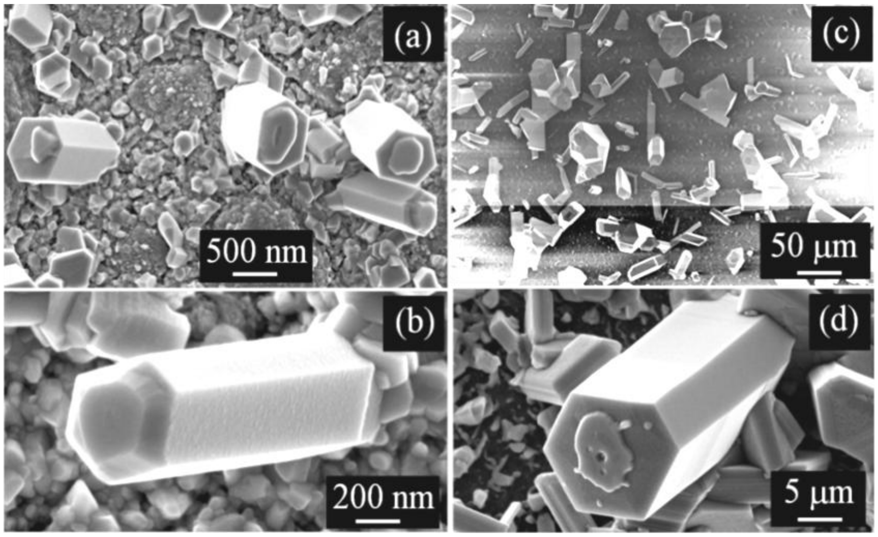

Figure 3.14 The FESEM images of hexagonal shaped crystallites grown on Al (50–100 nm) coated substrates *via* a VS mechanism. (a) Distribution nano to sub–microrods on Si(100) substrate (b) High magnification image of single hexagonal crystallite (c) Distribution microrods on *c*–sapphire substrate (d) High magnification image of single hexagonal microrod.

The high resolution FESEM image of a single hexagonal crystallite shows (Fig. 3.14b) well–faceted and very smooth surface morphology. Moreover, the as–grown crystals show different size distributions with diameters dimensionally varying from nano– to sub–micro regime. The FESEM image of as–prepared sample on Al (50–100 nm) coated *c*–sapphire substrate also shows the perfect hexagonal shaped microrods (Fig. 3.14c). The figure 3.14d shows the high magnification image of a single microrod with perfect planar and morphologically smooth facets. Therefore, in the present study, we were able to synthesize nano– to sub–micro sized hexagonal crystallites on Si(100) substrates, as well as microrods on the *c*–sapphire substrates *via* the VS growth mechanism.

3.3.1.2 Growth of AlGaN on Al+Ga thin film: Elongated NWs

The FESEM images (Fig. 3.15) of the as–prepared sample synthesized *via* the VS growth mechanism show a distribution of flower shaped cluster of NWs. The size of NWs islands (Fig. 3.15a) over the Al+Ga coated substrate is around 80–100 µm.

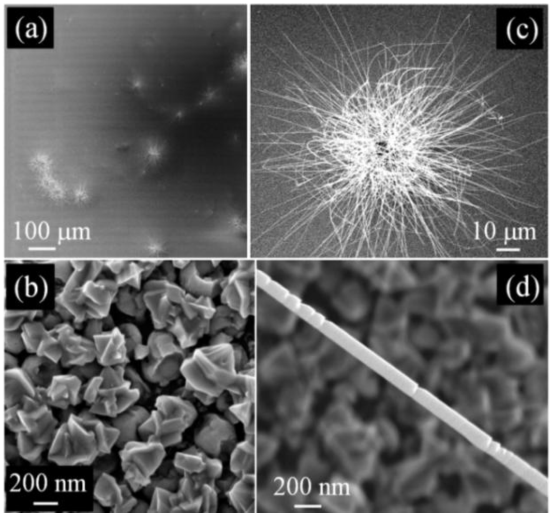

Figure 3.15 The FESEM images of flower shaped cluster of NWs. (a) Low magnification image for the islands of NWs grown on the Al+Ga thin film. (b) High magnification image of nano–crystallites on the film. (c) The magnified image for the cluster of elongated NWs (d) High magnification image of a single NW.

The high magnification image of Al+Ga thin film (Fig. 3.15b) shows the formation of almost hexagonal shaped nano–crystallites with sizes around 300–500 nm. The magnified image for the cluster of NWs shows (Fig. 3.15c) elongated NWs with high aspect ratio and an average length of 50 µm. Cylindrically shaped NW with diameter of ~100 nm was observed, as shown in the high magnification image of a single NW (Fig. 3.15d). More stable and energetically favorable facets of AlGaN nano–crystallites (Fig. 3.15b) in Al+Ga thin film can act as a seed for the VS growth process.[10,13] Therefore, it is observed that nanostructures grown on Al+Ga coated on the Si substrate are formed in the shape of cylindrical NWs. Whereas, in the second case of Al coated substrates yields mainly the hexagonal shaped sub–micro or microrods.

3.3.1.3 Structural analysis: X–ray diffraction (XRD)

Crystallographic structural study of the fully grown substrate with microrods show (Fig. 3.16a) (*hkl*) planes of (100), (002), (101), (102), (110), (103), (200), (112), (201), (004) and (202) at 2θ values of 32.41, 34.53, 36.83, 48.10, 57.77, 63.44, 67.75, 69.10, 70.50, 72.94 and 78.45°, respectively, which correspond to the wurtzite phase of GaN (JCPDS # 00–050–0792). The absence of any peak shift due the presence of Al may be due to low Al content (<5 at%) in the sample. Polycrystalline nature in the XRD pattern indicates the presence of all possible orientations in ensemble of these microrods.

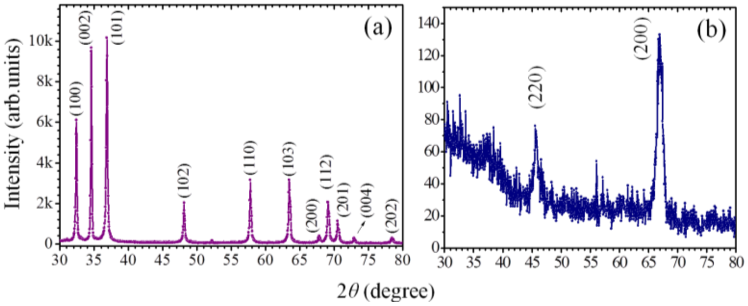

Figure 3.16 The XRD pattern of (a) microrod in the wurtzite GaN phase and (b) cubic AlN phase of base layers on intrinsic Si(100) substrate.

Furthermore, the presence of AlN base layer over the intrinsic Si(100) substrate is confirmed by the XRD analysis (Fig. 3.16b) of annealed AlN thin film at 1100 ^{o}C for 1 hr in presence of NH_3. This additional experiment was performed, as it was difficult to identify AlN base layer in the fully grown substrate in presence of large amount of microrods. The crystallographic structural study shows peaks corresponding to (*hkl*) planes of (200) and (220) at 2θ values of 45.76 and 67.08 degree, respectively, which match with the cubic phase of AlN (JCPDS # 00–046–1200).

3.3.1.4 Elemental analysis: X–ray photoelectron spectroscopy

The XPS mesurements were carried out for the bare AlN thin film, as well as AlGaN microrods grown on an AlN base layer for further elemental analysis of the respective samples. The Shirley type back ground corrected XPS spectra for different elements and their characteristic electronic transitions for each sample are shown in the figure 3.17.

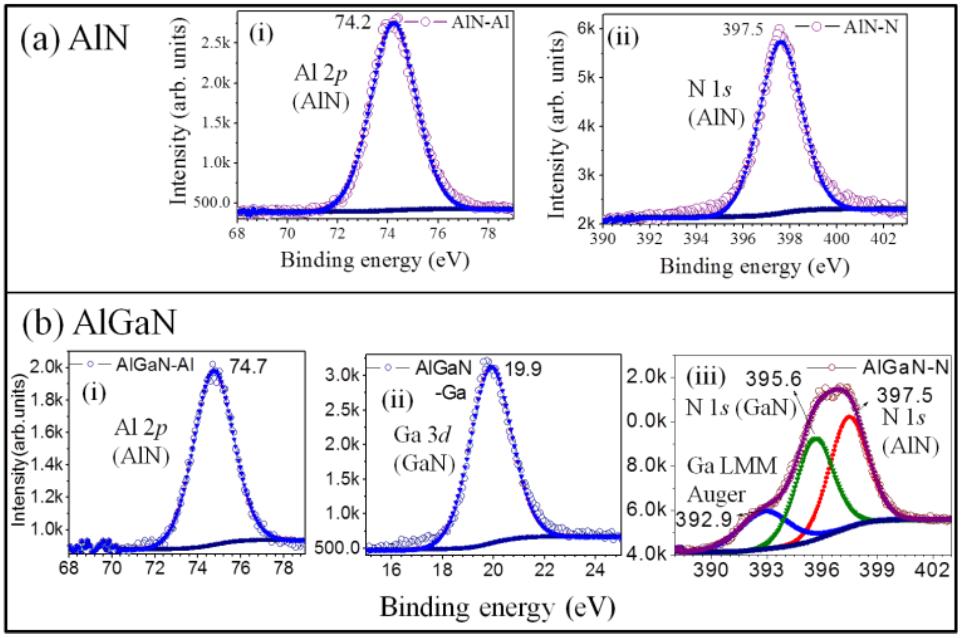

Figure 3.17 Typical XPS spectra for different elements and its characteristic electronic transitions with the corresponding binding energy values of (a) AlN thin film for (i) Al 2*p* and (ii) N 1*s* as well as (b) AlGaN hexagonal microrods for (i) Al 2*p* (ii) Ga 3*d* and (ii) N 1*s*.

In the case of AlN thin film (Fig. 3.17a), the binding energy for Al 2*p* (AlN) level is observed at 74.2 eV (Fig. 3.17a(i)) and N 1*s* (AlN) core level is identified at 397.5 eV (Fig. 3.17a(ii)). Similarly, in the case of AlGaN microrods grown on the AlN base layer (Fig. 3.17b), the Al 2*p* level transition is observed at 74.7 eV (Fig. 3.17b(i)). In this sample, we can expect that the XPS signal may show the cumulative effect of AlN base layer as well as from the AlGaN microrods. Moreover, the presence of an additional peak centered at 19.9 eV corresponding to the Ga 3*d* (GaN) level transitions (Fig. 3.17b(ii)) in the AlGaN sample, as compared to the AlN thin film, further confirms the incorporation of Ga along with Al in the sample. The peak positions of both the Al 2*p* and the Ga 3*d* are well matched with the reported literature values for AlGaN samples.[13,30] The N 1*s* spectrum (Fig. 3.17b(iii)) of AlGaN sample is very broad along with the presence of the Ga Auger peak. The N 1*s* peak is deconvoluted into two distinct peaks (Fig. 3.17b(iii)); the peak observed at 397.3 eV is due to the contribution from the N 1*s* (AlN) level transitions and the other peak centered at 395.6 eV appears due to the N 1*s* from GaN or AlGaN level transitions. The peak at around 392.9 eV in the N 1*s* spectrum is due the Ga LMM Auger transition.[13,18,29-31] Therefore, the XPS study provides a supportive and substantiating evidence for the incorporation of Al in the proposed VS growth mechanism. The mean free path of the photoelectrons of Al 2*p*, N 1*s* and Ga 3*d* is approximately 2 nm and the corresponding depth information is around 6 nm. However, the XPS spectra were recorded from the whole area of the sample, so the spectral intensity was influenced, not only from the microrods but also from the AlN base layer. Therefore, we cannot estimate the Al content of single AlGaN microrod from the above spectra.

3.3.2 Optical properties of samples grown *via* VS mechanism

3.3.2.1 Vibrational properties: Raman spectroscopy

In order to confirm the phase of the as–prepared hexagonal shaped crystallites, the vibrational modes were probed using Raman spectroscopy (Fig. 3.18) by focusing the laser beam with a spot size of ~1 μm, very precisely and exactly on a single and isolated microrod (size ~3 μm).

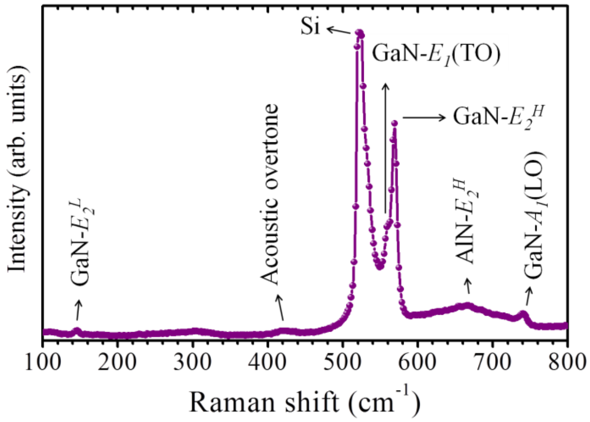

Figure 3.18 Typical Raman spectra of an AlGaN single crystal hexagonal microrod.

The spectral lines centered at 146, 425, 559, 569 and 741 cm^{-1} (Fig. 3.18) are assigned to the symmetry allowed Raman modes of E_2^L, acoustic overtone, E_1(TO), E_2^H and A_1(LO) modes of wurtzite GaN phase, respectively.[10-13] The presence of an extra peak centered at 667 cm^{-1} is assigned as AlN–E_2^H mode. The simultaneous observation of GaN–E_2^H mode along with the AlN–E_2^H in a single Raman spectrum, recorded from a single hexagonal micro–crystal, indicates the two–mode behavior of the phonons in the random alloy formation of the AlGaN phase.[10-13] Moreover, we observed a significant blue shift in A_1(LO) mode of the AlGaN crystal (~741 cm^{-1}), as compared to that for the pure GaN (~734 cm^{-1}). The percentage of Al in the AlGaN is estimated to be ~3.0 at% using the formula $A_1(\mathrm{LO}) = 734+153x+\mathrm{b}_{A1(\mathrm{LO})}x(1-x)$ with the bowing parameter of $\mathrm{b}_{A1(\mathrm{LO})} = -75$ cm^{-1}.[11-13] Furthermore, similar Raman modes were also observed for the NWs grown *via* VS mechanism.

3.3.2.2 Luminescence properties: Photoluminescence

Room temperature PL spectrum (Fig. 3.19) of a single AlGaN hexagonal microrod shows strong emission peaks centered at ~3.52 and ~3.32 eV. The emission peak centered at 3.52 eV is due to the recombination of the FE from the conduction band minimum to the valence band maximum. The luminescence peak observed at 3.32 eV is originated because of the recombination of the neutral DAP of D^0A^0. This luminescence peak is observed due to a transition from a shallow donor state of V_N to a deep acceptor state of V_{Ga}.[10,13,17-19] Similar to the PL emissions, as observed in the case of NWs grown *via* VLS mechanism, the significant blue shift in the band edge emission compared to pure GaN (~3.47 eV) is also a strong indication for the presence of Al in the sample synthesized *via* VS mechanism.

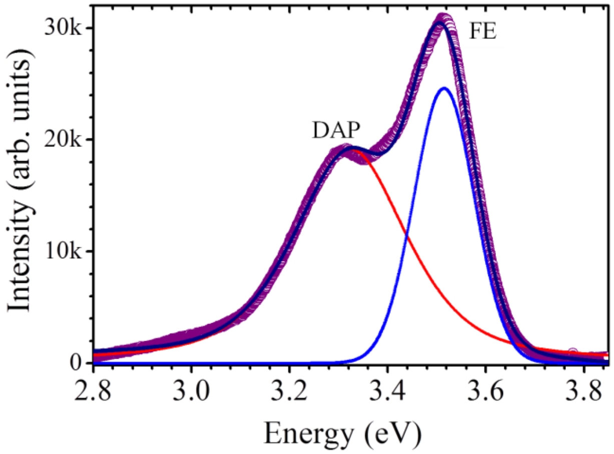

Figure 3.19 Typical photoluminescence spectra of an AlGaN single crystal hexagonal microrod. The peak centered at ~3.52 eV is due to the recombination of free exciton (FE) and the peak observed at ~3.32 eV is originated because of the neutral donor acceptor pair (DAP) recombinations.

From the shift of PL peak in AlGaN microrods compared to that of pure GaN, the approximate percentage of Al in the as–grown sample is found to be ~2.0 at% using the formulation of band bowing with respect to the observed and stoichiometric AlN (E_g ~6.20 eV) and GaN (E_g ~3.47 eV) phases.[2,17] Therefore, the value of the Al content in the sample, as derived from both Raman and PL spectroscopic techniques, matches fairly well with each other. A very high PL intensity, obtained in these crystallites even for low excitation laser power, ensures high optical quality of the material. Moreover, similar PL emission peaks were also observed for the AlGaN NWs grown *via* the VS mechanism synthesized over the Al+Ga coated substrate (not shown in figure).

3.4 Summary

1D nanostructures of ternary wurtzite AlGaN were synthesised *via* Au catalytic assisted VLS and self–catalytic VS mechanisms. The 1D NWs were synthesised, mostly, using APCVD deposition technique by adopting the VLS growth mechanism. The NWs with different size, shape and distribution were grown, *via* altering the number density distribution of Au catalyst NPs. The Ostwald ripening, which plays a key role in the size variation of NWs, is highly probable for dense distribution of Au NPs at higher temperature. The cylindrically shaped and mono–dispersed AlGaN NWs sample is envisaged in a single–prong growth mechanism. Similarly, the growth of an ensemble of triangular shaped NWs is conceived following the multi–prong growth mechanism. The NH_3 flow rate suitable for 1D NW growth was optimized as 50 sccm. Similarly, the on–set temperature of the NH_3 gas flow suitable for 1D NW growth was optimized as 750 and 800 ^{o}C for cylindrical and triangular NWs, respectively. The presence of Al is confirmed by the EFTEM analysis. The growth direction is found to be along [1-100], which is normal to the non–polar *m*–plane for both of the cylindrical and triangular shaped wurtzite AlGaN NWs independent of their surface morphology. The simultaneous presence of Raman modes corresponding to GaN–E_2^H at ~567 cm^{-1} and AlN–E_2^H at ~668 cm^{-1}represent the two–mode behavior of the AlGaN random alloy.

A significant blue shift of the free exciton emission at ~3.55 eV observed in the PL spectrum for AlGaN NW as compared to the GaN band gap of ~3.47 eV at 300 K further confirms the presence of Al in the synthesized samples. The approximate atomic percentage of Al is found as ~3.0% from the band bowing formalism. Moreover, the synthesis of hexagonal microrods and NWs of wurtzite AlGaN *via* a self–catalytic VS mechanism also show the random alloy formation, which is confirmed by the presence of two mode behavior of E_2^H phonons in the Raman spectra and significant blue shift in the PL emission. The approximate Al percentage is estimated ~2.0–3.0% for the samples grown *via* the VS mechanism from the blue shift of the A_1(LO) mode as well as the band edge emission.

3.5 References

[1] S. Zhao, H. P. Nguyen, M. G. Kibria and Z. Mi, *Prog. Quantum Electron.* **2015**, 44, 14

[2] C. He, Q. Wu, X. Wang, Y. Zhang, L.Yang, N. Liu, Y. Zhao, Y. Lu, and Z. Hu, *ACS Nano* **2011**, 5, 1291

[3] S. Chattopadhyay, A. Ganguly, K. H. Chen and L. C. Chen, *Crit. Rev. Solid State Mater. Sci.* **2009**, 34, 224

[4] P. Dogan, O. Brandt, C. Pfüller, J. Lähnemann, U. Jahn, C. Roder, A. Trampert, L. Geelhaar, and H. Riechert, *Cryst. Growth Des.* **2011**, 11, 4257

[5] C. Tessarek, R. Röder, T. Michalsky, S. Geburt, H. Franke, R. Schmidt-Grund, M. Heilmann, B. Hoffmann, C. Ronning, M. Grundmann, and S. Christiansen, *ACS Photonics* **2014**, 1, 990

[6] G. C. Yi, *Semiconductor Nanostructures for Optoelectronic Devices: Processing, Characterization and Applications*, **2012**, Springer–Verlag Berlin Heidelberg, Chapter 1, 1–36, DOI:10.1007/978–3–642–22480–5

[7] C. C. Chen, C. C.Yeh, C.H.Chen, M.Y. Yu, H. L. Liu, J. J. Wu, K. H. Chen, L. C. Chen, J. Y. Peng and Y. F. Chen, *J. Am. Chem. Soc.* **2001**, 123, 2791

[8] K. W. Kolasinski, *Curr. Opin. Solid State Mater. Sci.* **2006**, 10, 182

[9] Y. Wu, P. Yang, *J. Am. Chem. Soc.* **2001**, 123, 3165

[10] A. K. Sivadasan, A. Patsha, S. Polaki, S. Amirthapandian, S. Dhara, A. Bhattacharya, B. K. Panigrahi, and A. K. Tyagi, *Cryst. Growth Des.* **2015**, 15, 1311

[11] V. Y. Davydov, I. Goncharuk, A. Smirnov, A. Nikolaev, W. Lundin, A. Usikov, A. Klochikhin, J. Aderhold, J. Graul, and O. Semchinova, *Phys. Rev. B* **2002**, 65, 125203

[12] H. Harima, *J. Phys.: Condens. Matter* **2002**, 14, R967

[13] A. K. Sivadasan, G. Mangamma, S. Bera, M. Kamruddin, and S. Dhara, *J. Appl. Phys.* **2016**, 119, 174304

[14] K. K. Madapu, S. Dhara, S. Amirthapandian, S. Polaki and A. K.Tyagi, *J. Phys. Chem. C* **2013**, 117, 21930

[15] P. Sahoo, S. Dhara, S.Amirthapandian, M. Kamruddin, S. Dash, B. K. Panigrahi, and A. K. Tyagi, *Cryst. Growth Des.* **2012**, 12, 2375

[16] T. Livneh, J. Zhang, G. Cheng and M. Moskovits, *Phys. Rev. B* **2006**, 74, 035320

[17] A. Patsha, S. Amirthapandian, R. Pandian, S. Bera, A. Bhattacharya, S. Dhara, *J. Phys. Chem. C* **2014**, 118, 24165

[18] A. Patsha, S. Amirthapandian, R. Pandian and S. Dhara, *J. Mater. Chem. C* **2013**, 1, 8086

[19] M. A. Reshchikov and H. Morkoç, *J. Appl. Phys.* **2005**, 97, 061301

[20] S. Dhara, S. Chandra, G. Mangamma, S. Kalavathi, P. Shankar, K. G. M. Nair, A. K. Tyagi, C. W. Hsu, C. C. Kuo, L. C. Chen, K. H. Chen and K. K. Sriram, *Appl. Phys. Lett.* **2007**, 90, 213104

[21] H. Pan and Y. P. Feng, *ACS Nano.* **2008**, 2, 2410

[22] U. Tisch, B. Meyler, O. Katz, E. Finkman, J. Salzman, *J. Appl. Phys.* **2001**, 89, 2676

[23] S. Kurai, F. Ushijima, H. Miyake, K. Hiramatsu, and Y. Yamada, *J. Appl. Phys.* **2014**, 115, 053509

[24] T. Kuykendall, P. Ulrich, S. Aloni and P. Yang, *Nat. Mater.* **2007**, 6, 951

[25] J. C. Johnson, H. J. Choi, K. P. Knutsen, R. D. Schaller, P. Yang, R. J. Saykally, *Nat. Mater.* **2002**, 1, 106

[26] T. Auzelle, B. Haas, A. Minj, C. Bougerol, J. L. Rouvière, A. Cros, J. Colchero, and B. Daudin, *J. Appl. Phys.* **2015**, 117, 245303

[27] M. D. Brubaker, I. Levin, A. V. Davydov, D. M. Rourke, N. A. Sanford, V. M. Bright, and K. A. Bertness, *J. Appl. Phys.* **2011**, 110, 053506

[28] L. Largeau, E. Galopin, N. Gogneau, L. Travers, F. Glas, and J. C. Harmand, *Cryst. Growth Des.* **2012**, 12, 2724

[29] Baur, G. Steinhoff, J. Hernando, O. Purrucker, M. Tanaka, B. Nickel, M. Stutzmann, and M. Eickhoff, *App. Phys. Lett.* **2005**, 87, 263901

[30] F. L. M. Khir, M. Myers, A. Podolska, T. M. Sanders, M. V. Baker, B. D. Nener, and G. Parish, *Appl. Surf. Sci.* **2014**, 314, 850

[31] V. Thakur and S. Shivaprasad, *Appl. Surf. Sci.* **2015**, 327, 389

CHAPTER 4

OPTICAL PROPERTIES: EFFECT OF CRYSTALLOGRAPHIC ORIENTATIONS

"*I bought a crystal ball, and I wanted to use it, but I didn't know how, and I wouldn't use it until I developed a technique to use it that was truthful*" ... Michael Moschen

4.1 Introduction

The III–nitride sub–micro or microrods are attractive for different type of optoelectronic devices for its applications in making coaxial MQW structures.[1] In addition to the optical properties,[2,3] the polar nature of wurtzite crystals also find piezoelectric applications.[4,5] The performances of such optoelectronic devices are dependent on both the crystalline nature as well as the electronic properties of the material.

In the context of understanding the crystalline properties of the sub–micron sized crystallites, the polarized Raman spectroscopy is very efficient tool to investigate the crystallographic orientation in agreement with the selection rules.[5-9] However, the polarized Raman studies recorded from a single spot of the sample alone may not be sufficient to understand crystalline nature of the crystallites. Thus, the polarized Raman imaging corresponding to the peak intensities of allowed Raman modes throughout the different crystal planes may help us to predict the crystalline nature of the material.[8] The non–centrosymmetric wurtzite III–nitrides with a space group of $P6_3mc$ is polar in nature and it shows the direction dependent spontaneous polarization (SP).[10,11] Furthermore, the lattice strain in the sample may generate the electrostatic potential across the crystals, which leads to the piezoelectric (PE) polarization. The spontaneous and piezoelectric polarizations may constitute an intrinsic electric field in the crystal which may affect the optical and electronic properties of the crystallites.[4,5,10,11]

The present chapter describes the polarized Raman spectra of a single AlGaN sub–micron sized hexagonal crystallite for two different crystallographic orientations in the far–field configuration. The crystal orientation dependent polarized photoluminescence (PL) study is also conducted to understand the effect of different crystal planes on the optical properties of the crystallite. Moreover, in order to confirm the existence of an intrinsic electric field in the AlGaN hexagonal crystallites; the investigations are also includes the piezo–response force microscopic (PFM) imaging of single crystal microrods on the AlN base layer to understand the piezoelectric domains as well as piezoelectric coefficient.

4.2 Crystal orientation dependent polarized Raman spectra of hexagonal sub–microrods

4.2.1 Crystallographic orientation of single sub–microrod: Growth direction

The investigation of polarization dependent Raman scattering experiments was performed on a single sub–micron sized AlGaN crystallite for understanding its crystalline orientations. Two different isolated sub–microrod are chosen for the polarized Raman study in such a way that one is vertically aligned (Fig. 4.1a) and other one is horizontally lying (Fig. 4.1b) on the Si(100) substrate. The axis along the hexagonal sub–microrod, which is perpendicular to the *c*–plane is chosen as *Z*–direction. In the first case (Figs. 4.1a and 4.1c), both the incident and the scattered light propagation directions are considered along the *Z*–direction in the back scattering geometry along *c*–axis of the wurtzite crystal, which is perpendicular to the hexagonal facet of the AlGaN crystallite. Whereas, in the second case (Figs. 4.1b and 4.1d), the directions of the incident and scattered light propagation are perpendicular to the *Z*–direction i.e. normal to the *XY* plane. For each case, two different mutually perpendicular polarization conditions for scattered waves are configured (inscribed in Figs. 4.1c and 4.1d) using a half wave plate and a polarizer.[5,6]

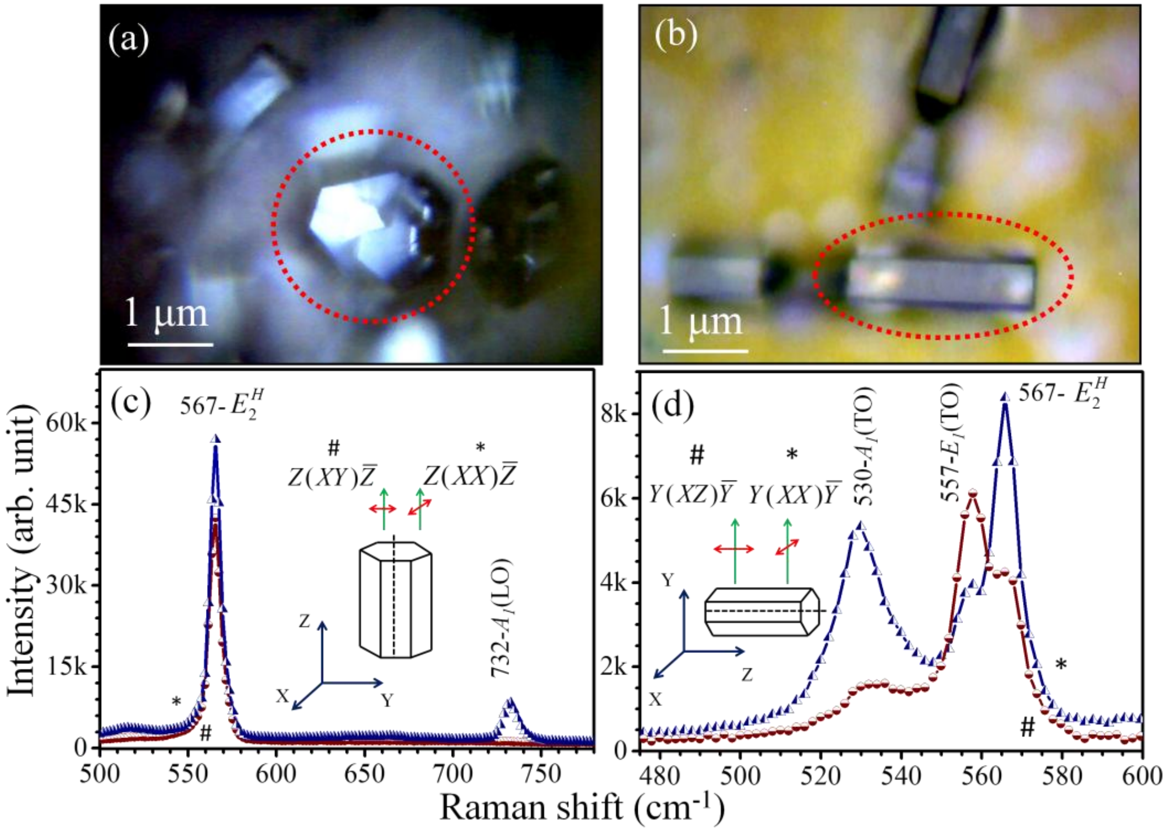

Figure 4.1 The optical images of (a) vertically and (b) horizontally oriented crystallites.The polarized Raman spectra for (c) *c*–plane (d) *m*–plane corresponding to vertically and horizontally aligned AlGaN hexagonal sub–microrod.

The distinct peaks centered at 530, 557, 567 and 732 cm^{-1} in Raman spectra (Figs. 4.1c and 4.1d) are assigned as A_1(TO), E_1(TO), E_2^H and A_1(LO) modes, respectively of wurtzite phase.[12-15] The intense and sharp peaks observed in the Raman spectra ensure the high quality of the crystal suitable for various optoelectronic applications. However, according to the polarization selection rule in the backscattering configuration, the possible configurations and corresponding allowed modes for a wurtzite [0001] oriented AlGaN (Z||[0001]) are given in the Table 4.1.[8,9,15-19]

Table 4.1: The allowed Raman modes for different polarization configurations for a wurtzite crystal

Configurations	*Modes*
$Y(XX)\bar{Y}$	$A_1(\mathrm{TO}), E_2^H$
$Y(ZZ)\bar{Y}$	$A_1(\mathrm{TO})$
$Y(XZ)\bar{Y}$	$E_1(\mathrm{TO})$
$Z(XY)\bar{Z}$	E_2^H
$Z(XX)\bar{Z}$	$A_1(\mathrm{LO}), E_2^H$

From Table 4.1, it is very easy to figure out the possible crystalline orientations from the polarization configurations corresponding to its allowed Raman modes obtained from the different polarization conditions of the incident and scattered waves keeping consistency with the Raman selection rules. For example, from the Table 4.1, it is obvious that the possible configurations for the combinations of Raman modes E_2^H and A_1(LO) in one polarization condition and E_2^H in the cross polarization (Fig. 4.1c) correspond to $Z(XX)\bar{Z}$ and $Z(XY)\bar{Z}$ configurations, respectively. The depolarization ratios (ρ) for E_2^H and A_1(LO) modes are found as 0.75 and 0.15, respectively. Since, the value of $\rho = 0.75$ for E_2^H mode, then the mode may be called as depolarized mode. Moreover, the A_1(LO) mode followed the condition $0 < \rho = 0.15 < 0.75$, then it may be called as highly polarized modes for the corresponding polarization configuration.[6] Similarly, in the case of horizontally lying crystallites, the prominent observed modes in the Raman spectra are A_1(TO) and E_2^H in one polarization and E_2^H alone in the cross polarization. The possible scattering configurations for the corresponding allowed modes are $Y(XX)\bar{Y}$ and $Y(XZ)\bar{Y}$, respectively (Table 4.1). It is obvious that, in this case the incident and scattered wave vector is perpendicular to the *XZ* plane (*m*–plane, (1-100)).The corresponding schematic illustration of the crystal and its polarization configuration is depicted in the inset of figure 4.1d. Similarly, the depolarization ratios for A_1(TO), E_1(TO) and E_2^H modes are calculated as 0.30, 0.64 and 0.51, respectively. Moreover, in the case of second configuration the value of ρ for all the modes falls in between the values of 0 and 0.75, therefore they may be called as polarized modes.[6]

4.2.2 Polarized Raman imaging of AlGaN sub–microrod: Single crystalline nature

In order to understand whether the polarization conditions for different allowed Raman modes would satisfy throughout the entire crystal, we carried out the polarized Raman imaging for each plane such that we could estimate the Raman intensity corresponding to possible polarization modes from a predefined grid area of the crystal (Fig. 4.2). We constructed a 3 × 2 μm^2 rectangular area with a grid resolution of 500 nm for polarized Raman spectra for scanning the top *c*–plane of the single sub–microrod (Fig. 4.2a). Whereas, in the second case, we carried out the same acquisition in a predefined area of 6 × 1 μm^2 (grid resolution of 500 nm), which exactly covered the *m*–plane of the single AlGaN crystallite (Fig. 4.2b).

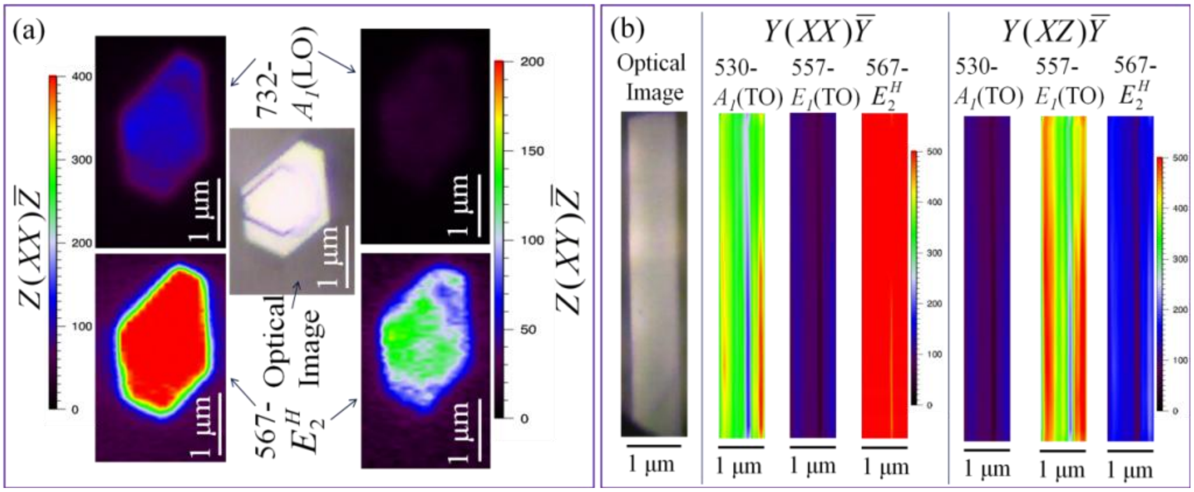

Figure 4.2 The Raman spectral imaging in different polarization configuration as inscribed in the respective figures corresponding to vertically and horizontally aligned single sub–microrods along (a) *c*–and (b) *m*–planes.

In case of *c*–plane imaging of sub–microrod (Fig. 4.2a) both the allowed Raman modes E_2^H and A_1(LO) appeared for the polarization configuration of $Z(XX)\bar{Z}$. Whereas, the intensity distribution is prominent only for E_2^H and it is absent for A_1(LO) mode in the case of cross polarization $Z(XY)\bar{Z}$. Similarly, in the second case of *m*–plane imaging of AlGaN sub–microrod, the allowed Raman modes A_1(TO) and E_2^H appeared with prominent intensities for $Y(XX)\bar{Y}$ configuration. Whereas, the intensity distribution corresponding to E_2^H is more prominent compared to others in the case of cross polarization $Y(XZ)\bar{Y}$. Thus, by comparing the figures 4.1 and 4.2, it is obvious that, the relative intensity variations for different allowed Raman modes for different polarization conditions are consistent with the spectrum from a single spot as well as in the spectral images covering the entire crystalline planes. Therefore, even though the size of the single AlGaN crystal is in the sub–micron regime, it shows the single crystalline nature.

4.3 Crystal orientation dependent polarized PL spectra: Effect of intrinsic electric field of the crystal

The polarization dependent PL studies (Fig. 4.3) are carried out in a similar fashion, as in the polarized Raman studies (Fig 4.1) for a single crystalline AlGaN sub–microrod for understanding the crystal orientation dependent optical properties and polarization anisotropies. We maintained the same polarization configuration for the *c*–plane and *m*–plane oriented crystallites and the corresponding PL spectra are shown in the figure 4.3. We observe a distinct splitting, for the first time, in the PL spectra in the case of *c*–plane oriented crystallite for both polarization conditions (Fig. 4.3a). One of the peaks is centered at 3.32 eV and the other one is at 3.47 eV are assigned to DAP and FE emissions respectively.[12,13]

Whereas, in case of *m*–plane of the same sample, only the peak corresponding to FE emission is more prominent compared to that of DAP emission (Fig. 4.3b).

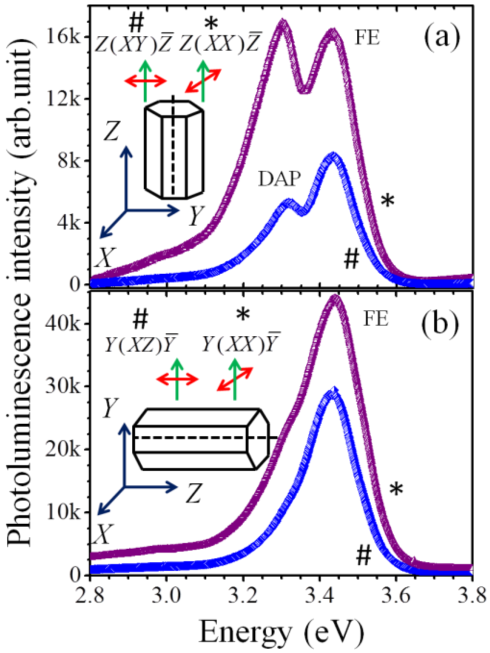

Figure 4.3 The polarized PL spectra for (a) *c*–plane (b) *m*–plane corresponding to vertically and horizontally aligned AlGaN sub–microrod.

The variation in intensity for different polarization configurations or polarization anisotropy is dependent on the material geometry as well as the anisotropic properties of crystalline medium. Thus, the intensity of parallel polarization (I_π) can be different from cross polarization (I_σ). The measure of this polarization anisotropy can be defined in terms of the polarization ratio, $\rho = (I_\pi - I_\sigma)/(I_\pi + I_\sigma)$, which is also known as the degree of polarization.[8,20,21] For the present study, the value of polarization ratios of the PL intensities of FE emission were calculated to be 0.24 and 0.33 corresponding to *c*–plane and *m*–plane oriented crystals, respectively.[8,20,21] The reduction in the PL intensities in σ–polarization with respect that for the π–polarization (Fig. 4.3) is related to the polarization anisotropy of the crystallites.

From the crystalline orientation dependent Raman imaging studies (Fig. 4.2), it is obvious that, the AlGaN sub–microrod shows single crystalline nature and it maintains the high quality along with the compositional homogeneity throughout the crystal. It is well known that the possibility of formation of defects and stacking faults along the *c*–plane is more probable as compared to those in the *m*–plane. In other words, the defect density along *m*–plane is comparatively less than that of *c*–plane.[8,11,22-24] Furthermore, because of the non–centrosymmetric nature of wurtzite crystal, there is a possibility of SP along the *c*–axis of the crystal. Moreover, the effect of strain due to the presence of lattice mismatch with the substrate and defects in the wurtzite crystal may also produce some additional PE field.[11,22-24] The simultaneous presence of spontaneous and piezoelectric polarizations in the sub–microrod develop an intrinsic electric field inside the crystal. Consequently, the interaction of internal crystal fields to the external electric field of the *em* (laser) excitation is likely to influence the PL spectra by enhancing the splitting between the DAP and FE emissions along *c*–plane, as compared to that of *m*–plane (Fig. 4.3).[8] Whereas, the optical properties of a homogenous single crystal along *m*–plane are expected to be comparatively free from SP as well as strain related PE fields exhibiting high optical quality with sharp band edge emissions (Fig. 4.3b).[5-9,11,22-25] Therefore, in the case of III–nitrides, it is advisable that the *m*–plane oriented crystallites are more favorable for making high performance devices than that with the *c*–plane oriented crystals.

4.3.1 Crystal orientation dependent PFM studies: Effect of spontaneous and piezoelectric field

Piezoelectricity linearly relates an external electrical field to mechanical strain of the material, leading to a direct piezoelectric effect ($P_i = d_{\mathrm{ijk}}\, e_{\mathrm{jk}}$) and a converse piezoelectric effect ($\varepsilon_{\mathrm{ij}} = d_{\mathrm{ijk}}\, E_{\mathrm{k}}$), where P is the polarization vector, e_{jk} is the stress tensor, $\varepsilon_{\mathrm{ij}}$ is the strain tensor, E is the electric field vector, and d_{ijk} is the piezoelectric tensor of rank three.[4,5,11,13,26,27] For the

AlGaN/AlN system, the total polarization P arises from SP originated due to the nature of the crystal and the polarity of the interfaces between the hetero–junctions, and the other one is PE polarization due to the lattice strain. The spontaneous electric polarization (P^{SP}) and piezoelectric polarizations (P^{PZ}) generate a built–in electrostatic field all over the sample surface.[11,13,26,27] Eventually, both of the above discussed polarizations and its discontinuity at the inter–junctions lead to a net charge density (σ_{s}).[13,28] The σ_{s} and immobile P^{PZ} charges may play a major role in the interaction of the wurtzite AlGaN with the external electric field as well as the mechanical strain.[13,28,26,27] For AlGaN micro–crystals, the SP is expressed as,

$$\vec{\mathrm{P}}^{\mathrm{SP}} = P^{\mathrm{SP}}.\hat{z} \quad \ldots\ldots\ldots\ldots \; (4.1)$$

where $\hat{z}$ is a unit vector in the [0001] direction.[13,28] For any wurtzite crystal, such as InN, AlN, GaN, and its alloys, *e.g.*, AlGaN, the induced PE field can be written as follows,[13,28]

$$P^{\mathrm{PZ}} = (d_{51}\varepsilon_{31})\hat{x} + (d_{51}\varepsilon_{23})\hat{y} + (d_{31}\varepsilon_{11} + d_{31}\varepsilon_{22} + d_{33}\varepsilon_{33})\hat{z} \quad \ldots\ldots\ldots\ldots \; (4.2)$$

Considering z along the c–axis, ε_{11}, ε_{22} and ε_{33} are the strains along the x, y and z axis, respectively. On the other hand, ε_{23} and ε_{31} are shear strains. Here, d_{31}, d_{33} and d_{51} are known as the PE coefficients found in the wurtzite crystal structure.[13,28] In any 3D coordinate system, each mutually independent element in the PE third rank tensor depends only on the crystallographic structure and orientations of the material. In the converse PE effect, an electric field is applied across the crystal generating strain or deformation in the material.[11,13,26,27] The PE tensor in AlGaN with space group of $P6_3mc$, has three independent constants, d_{13}, d_{15}, and d_{33}. It is reported that, the relation between strain–electric field ($\varepsilon_{ij} = d_{ijk}E_k$) for such kind of PE material with *6mm* point group symmetry can be expressed as follows.[11,13,26,27]

$$\begin{pmatrix} \varepsilon_{11} \\ \varepsilon_{22} \\ \varepsilon_{33} \\ 2\varepsilon_{23} \\ 2\varepsilon_{13} \\ 2\varepsilon_{12} \end{pmatrix} = \begin{pmatrix} 0 & 0 & d_{31} \\ 0 & 0 & d_{31} \\ 0 & 0 & d_{33} \\ 0 & d_{15} & 0 \\ d_{15} & 0 & 0 \\ 0 & 0 & 0 \end{pmatrix} \begin{pmatrix} E_1 \\ E_2 \\ E_3 \end{pmatrix} \quad \text{..} \ (4.3)$$

From the above equation 4.3, the induced strain in presence of the external electric field along different directions is therefore expressed as $\varepsilon_{11} = \varepsilon_{22} = d_{31}E_3$, $\varepsilon_{33} = d_{33}E_3$, $2\varepsilon_{23} = d_{15}E_2$, $2\varepsilon_{13} = d_{15}E_1$, and $\varepsilon_{12} = 0$. Using the PFM set up, the displacement of the cantilever due to the total polarization of the crystal can be measured as in terms of the PE coefficient,

$$\Delta Z = d_{33}V_{dc} + d_{33}V_{ac}\cos(\omega t + \varphi) \quad \text{.......................................} (4.4)$$

The magnitude of the oscillating response is a measure of the magnitude of d_{33} and the phase is sensitive to the polarization direction of the sample.[13,27] The vibrational amplitude is related to the vertical projection of the polarization. The vibration phase lag varies in between –180° to +180°, depending on whether the polarization is pointing up or down (Figs. 2.12b and 2.12c in the Chapter 2), or the angular inclination between the external field and the polarization (Figs. 2.12c and 2.12d in the Chapter 2).

4.3.2 The domain switching in the piezoelectric zones of AlGaN microrod

The topography as well as PFM magnitude images of AlGaN microrods on an AlN base layer over the intrinsic Si(100) substrate are shown in figures 4.4a–e. The possible reason for contrast variation at the interface in the PFM images (Figs. 4.4b and 4.4c) may be due to the variation of surface charge density (σ_s) at the bottom surface of micro–crystals originating from the variation of crystalline orientation with respect to the AlN base layer.

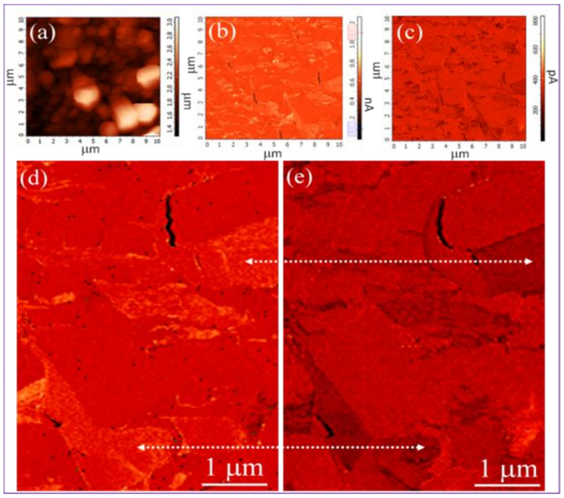

Figure 4.4 (a) AFM topography of AlGaN hexagonal microrods and corresponding PFM images with an external voltage (b) +5V and (c) –5V. The domain switching in the PE zones indicated by arrows in the zoomed portion of PFM images of (d) +5V and (e) –5V.

At the Al$_x$Ga$_{1-x}$N/AlN interface the surface charge density follows the relation,

$$\sigma_s = \nabla.P = x(P_{AlN}^{SP} - P_{GaN}^{SP})\cos\varphi \quad \text{...} \ (4.5)$$

where φ is the angle of the interface between AlN base layer and AlGaN microrods with respect to the [0001] direction. Therefore, angular orientation of the AlGaN micro–crystals with respect to the AlN base layer may also influence the σ_{s} and P^{PZ}. It may lead to the variation of induced σ_{s} over the micro–crystals and hence a possible observation of contrast in the PFM images due to the presence of different P^{PZ} domains in the sample (Figs. 4.4b and 4.4c). The bright and dark contrast, corresponding domain expansion or contraction, is found to interchange while switching the polarity of the external bias voltage from +5V (Fig. 4.4d) to −5V (Fig. 4.4e). The dotted arrows in the figure indicate some specific area showing switching (flipping in) of the P^{PZ} with respect to the external bias voltage for different planes of the crystals.

In piezo–spectroscopy mode, probing of electromechanical response can be carried out as a function of DC bias of the tip from a single point of the crystal (Fig. 4.5).

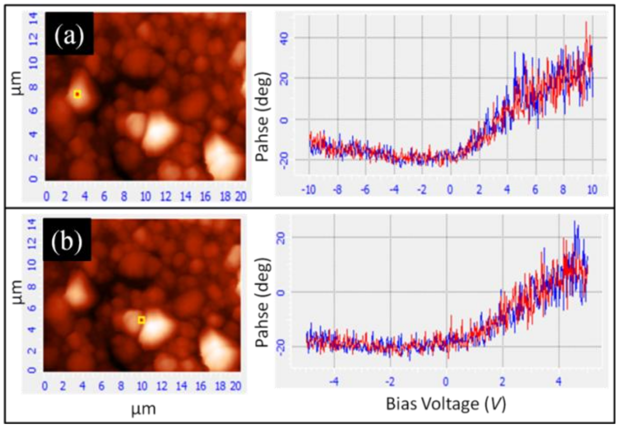

Figure 4.5 The piezo–spectroscopy to show the topography and phase profiles from a single point on the AlGaN microrod with respect to a complete cycle of +ve to –ve external bias voltage for two different places (marked) of (a) and (b) of the sample.

The graph plotted between external bias voltages against phase change, represents the variation of phase change of the P^{SP} with respect to the polarity and magnitude of the external bias. After application of one complete cycle of +ve to –ve external bias voltage, it is clearly visible that, the phase angle switches between the -20^o to $+20^o$ even for a single spot (marked in topographs in Figs. 4.5a and 4.5b) on the AlGaN crystal itself. This explains and ensures a supplementary evidence for the switching behavior of polarization in single crystal AlGaN microrod.

4.3.3 The piezoelectric coefficient (d_{33}) of AlGaN microrod

The electric field is created along the microrod (z–direction) through the PE effect, $E_z=\varepsilon_{33}/d_{33}$. Therefore, the effective PE coefficient along the c–axis can be calculated as the ratio between deformation of the crystal (ΔZ) along c–axis and applied voltage V:

$$d_{33} = \varepsilon_{33}/ E_z = \Delta Z/V \quad \ldots\ldots\ldots\ldots\ldots\ldots\ldots\ldots\ldots (4.6)$$

where $\varepsilon_{33} = \Delta Z/Z$ is the change of strain along the c–axis (Figs. 2.12b and 2.12c in the Chapter 2), and $E_z = V/Z$ is the electric field along the c–axis.[13,28-31] The strain coefficient, ε_{33} is calculated by analyzing the deformation of crystal from line scan data of the PFM image. By using the Eqn. (4.6), we calculated the approximate value of d_{33} along the c–axis as 4.14 pm/V. The calculated value of d_{33} is slightly different from the reported values 5.1 and 3.1 pm/V for unclamped AlN and GaN, respectively.[29,32] The small deviations in the value of d_{33} may be due to the following reasons. In one of the possibilities, the d_{33} value for Al doped GaN may be slightly higher than that of the undoped GaN synthesized by APCVD. At the same time, the AlGaN crystals grown on an AlN base layer over Si(100) substrate are clamped by the substrate.[13,29,32] The substrate generates some constrain to the expansion and contraction of the synthesized materials and thus affects the measured strains.[13,29,32] As a result, the measured value of d_{33} is less than the true value of an unclamped AlN and more than that of the GaN samples.

4.4 Summary

The polarized Raman spectroscopic studies for different scattering configurations with respect to the vertical and horizontal planes are used to understand the crystalline orientation of an AlGaN sub–microrod. The integrated intensity distribution for the polarized Raman images corresponding to the respective allowed vibrational modes for the c– and m–planes shows single crystalline nature of the hexagonal sub–microrods. The origin of enhanced splitting in the PL spectra along the c–plane compared to that of m–plane may be because of the interaction of electric field of the excitation wave with the intrinsic crystal field, which is the resultant of the SP and strain related PE polarizations. The existence of PE domains in the sample is confirmed by recording the PFM imaging of AlGaN hexagonal microrods. The effective PE coefficient for AlGaN microrod along the c–axis (d_{33}) is found to be ~4.14 pm/V.

4.5 References

[1] K. Chung, H. Beak, Y. Tchoe, H. Oh, H. Yoo, M. Kim, and G. C. Yi, *APL Mater.* **2014**, 2, 092512

[2] Y. Li, J. Xiang, F. Qian, S. Gradecak, Y. Wu, H. Yan, D. A. Blom, and C. M. Lieber, *Nano Lett.* **2006**, 6, 1468

[3] Y. Chang, Y. Zhang, Y. Zhang, and K. Tong, *J. Appl. Phys.* **2006**, 99, 044501

[4] M. Minary-Jolandan, R. A. Bernal, I. Kuljanishvili, V. Parpoil, and H. D. Espinosa, *Nano Lett.* **2012**, 12, 970

[5] H. D. Espinosa, R. A. Bernal, and M. Minary–Jolandan, *Adv. Mater.* **2012**, 24, 4656

[6] M. Tanaka and R. J. Young, *J. Mater. Sci.* **2006**, 41, 963

[7] A. K. Sivadasan, A. Patsha, and S. Dhara, *Appl. Phys. Lett.* **2015**, 106, 173107

[8] A. K. Sivadasan and S. Dhara, *J. Raman Spectrosc.* **2016**, 47, 656

[9] A. Patsha, P. Sahoo, S. Dhara, S. Amirthapandian, and A. Tyagi, *J. Raman Spectrosc.* **2013**, 44, 651

[10] W. Su, Y. Chen, C. Hsiao, and L. Tu, *Appl. Phys. Lett.* **2007**, 90, 063110

[11] B. Gil, *Physics of Wurtzite Nitrides and Oxides: Passport to Devices*, **2014**, Springer Series in Materials Science 197, DOI: 10.1007/978–3–319–06805–3

[12] A. K. Sivadasan, A. Patsha, S. Polaki, S. Amirthapandian, S. Dhara, A. Bhattacharya, B. K. Panigrahi, and A. K. Tyagi, *Cryst. Growth Des.* **2015**, 15, 1311

[13] A. K. Sivadasan, G. Mangamma, S. Bera, M. Kamruddin, and S. Dhara, *J. Appl. Phys.* **2016**, 119, 174304

[14] V. Y. Davydov, I. Goncharuk, A. Smirnov, A. Nikolaev, W. Lundin, A. Usikov, A. Klochikhin, J. Aderhold, J. Graul, and O. Semchinova, *Phys. Rev. B* **2002**, 65, 125203

[15] H. Harima, *J. Phys. Condes. Matter.* **2002**, 14, R967

[16] H. Grille and Ch. Schnittler, *Phys. Rev. B* **2000**, 61, 6091

[17] E. Schäfer–Nolte, T. Stoica, T. Gotschke, F. Limbach, E. Sutter, P. Sutter, and R. Calarco, *Appl. Phys. Lett.* **2010**, 96, 091907

[18] P. J. Pauzauskie, D. Talaga, K. Seo, P. Yang, and F. Lagugné–Labarthet, *J. Am. Chem. Soc.* **2005**, 127, 17146

[19] T. Azuhata, T. Sota, K. Suzuki, and S. Nakamura, *J. Phys. Condes. Matter.* **1995**, 7, L129

[20] R. G. Banal, Y. Taniyasu, and H. Yamamoto, *Appl. Phys. Lett.* **2014**, 105, 053104

[21] J. Wang, M. S. Gudiksen, X. Duan, Y. Cui, and C. M. Lieber, *Science* **2001**, 293, 1455

[22] K. Filintoglou, M. Katsikini, J. Arvanitidis, D. Christofilos, A. Lotsari, G. Dimitrakopulos, N. Vouroutzis, A. Ajagunna, A. Georgakilas, and N. Zoumakis, *J. Appl. Phys.* **2015**, 117, 075302

[23] P. Ščajev, K. Jarašiūnas, Ü. Özgür, H. Morkoç, J. Leach, and T. Paskova, *Appl. Phys. Lett.* **2012**, 100, 022112

[24] Z. Bryan, I. Bryan, M. Bobea, L. Hussey, R. Kirste, Z. Sitar, and R. Collazo, *J. Appl. Phys.* **2014**, 115, 133503

[25] P. P. Paskov, R. Schifano, B. Monemar, T. Paskova, S. Figge, and D. Hommel, *J. Appl. Phys.* **2005**, 98, 093519

[26] Y. Duan, J. Li, S. S. Li, and J. B. Xia, *J. Appl. Phys.* **2008**, 103, 023745

[27] W. Wu, C. Pan, Y. Zhang, X. Wen, and Z. L. Wang, *Nano Today* **2013**, 8, 619

[28] B. M. Wong, F. Léonard, Q. Li, and G. T. Wang, *Nano Lett.* **2011**, 11, 3074

[29] I. Guy, S. Muensit, and E. Goldys, *Appl. Phys. Lett.* **1999**, 75, 4133

[30] K. Tonisch, C. Buchheim, F. Niebelschütz, A. Schober, G. Gobsch, V. Cimalla, O. Ambacher, and R. Goldhahn, *J. Appl. Phys.* **2008**, 104, 084516

[31] A. Romanov, T. Baker, S. Nakamura, and J. Speck, *J. Appl. Phys.* **2006**, 100, 023522

[32] C. M. Lueng, H. L. Chan, C. Surya, and C. L. Choy, *J. Appl. Phys.* **2000**, 88, 5360

CHAPTER 5

SURFACE AND INTERFACE OPTICAL PHONON MODES IN 1D NANORODS AND 2D MULTI–QUANTUM WELL STRUCTURES

"*In science there are no 'depths'; there is surface everywhere*" ....Rudolf Carnap

5.1 Introduction

The presence of periodicity on the surface of nanostructures leads to the generation of a specific class of optical phonon modes apart from the group theoretically allowed optical phonons at zone centre (wave vector, q=0).[1-4] Generally, in the case of wurtzite III–nitrides, two additional phonon modes with A_1 and E_1 symmetry are observed related to such surface modulations in between the frequency range of longitudinal optical ($\mathrm{LO}_{q=0}$) and transverse optical ($\mathrm{TO}_{q=0}$) phonon modes. These optical phonons, localized at the surface of nanostructures and originating because of the vibration of surface atoms, are known as surface optical (SO) phonons. Similar type of optical modes, appearing in the case of 2D MQW structures or periodic superlattices (SLs), are termed as interface optical (IO) phonon modes.[5-10] Moreover, the relative strength of IO or SO modes may decay exponentially from surface to bulk of the sample. Therefore, the observation of SO or IO modes are highly probable in the case of nanostructures with high surface to volume ratio compared to that of with bulk material.[5-10] Thus, the observation IO or SO phonon modes are attributed to the relaxation of Raman selection rules away from the Brillouin zone centre essentially because of the breakdown of translational symmetry of surface potential due to the presence of the periodic interfaces and surface modulations.[1-10]

In the present study, we report the Raman spectroscopic investigation of the SO and IO phonon modes in 1D nanorods (NRs) and 2D MQWs, respectively. A set of vertically aligned and hexagonal shaped 1D $Al_{0.97}Ga_{0.03}N$ NRs grown by means of plasma assisted molecular beam epitaxy (PAMBE) were used for the study of SO modes. A change in the dielectric medium is demonstrated to show a significant red shift of the additional modes with respect to those in air, and they show good agreement with the calculated SO phonon frequencies. Similarly, we also investigated the IO phonon modes in the case of *c*–plane oriented 2D $[AlN/GaN]_{20}$ and $[Al_{0.35}Ga_{0.65}N/Al_{0.55}Ga_{0.45}N]_{20}$ MQW nanostructures. The nominal shift in IO phonon mode of E_1 symmetry for $[Al_{0.35}Ga_{0.65}N/Al_{0.55}Ga_{0.45}N]_{20}$ compared to that of the $[AlN/GaN]_{20}$ MQW structure is understood on the basis of change in dielectric constants (ε_m) of the surrounding medium. The observed IO phonon modes in the spectra are attributed to the periodic interfaces and surface modulations.

5.2 Surface optical phonon mode in vertically aligned 1D $Al_{0.97}Ga_{0.03}N$ NRs

The growth of vertically aligned AlGaN NRs on the buffer layer of AlGaN(~300 nm) /AlN(~200 nm) over the *c*–plane oriented sapphire substrate were carried out with the help of PAMBE system with standard effusion cells for group III sources. The use of AlGaN/AlN buffer layer significantly reduces the dislocation density and improves the overall structural quality of the nanostructures as well as the quantum efficiency the optoelectronic devices.[11-14] High purity Al (7N) and Ga (6N5) metal were used for growth and two zone effusion cells were used to generate their fluxes. The ultra high pure N_2 gas (6N) further purified by the use of GATEKEEPER^{TM} filters was activated using an RF Plasma source. The growth was monitored *in–situ* by observing the reflection high energy electron diffraction (RHEED) pattern. Prior to growth, the substrate was out gassed at a temperature of 673K and preserved it in a background vacuum level of ~10^{-9} Torr for nearly 48 h. The growth was carried out in three steps. At first, nitrogen plasma (power: 350 W, flow rate: ~1.7 sccm) was used to convert the topmost layers of the sapphire (Al_2O_3) to AlN at a temperature of 1023K. Nitridation was followed by the growth of the AlN buffer layer at 1023K in presence of excess Al flux (at 2.75×10^{-7} Torr), which was evident by the dim and diffuse RHEED pattern. The time durations for nitridation were varied from 10 s, at the initial nucleation stage, to ~2 min towards the end of the AlN growth time. This process was similar to a metal modulated epitaxial deposition step, and strongly affected the morphology of the deposited film by modulating the surface diffusion length of adatoms. However, for group III rich conditions, as employed in the present study, the excess Al form nanoscale droplets were converted to hexagonal islands during the exposure to plasma. After the deposition of AlN layer, an AlGaN film was deposited with Al flux of 1.63×10^{-7} Torr, Ga flux of 5.12×10^{-7} Torr, and a substrate temperature of 1043K. The AlN islands, formed on the substrate, acted as nucleation centers for the formation of AlGaN NRs. The growth process was monitored by the *in–situ* observation of the RHEED pattern.

The morphological shape, size and distribution of AlGaN NRs are shown in the FESEM (FEI make dual beam Helios NanoLab-600i) images acquired with 20 kV and 2.7 nA (Fig. 5.1). The low magnification image shows (Fig. 5.1a) a top view of the uniformly distributed, as well as, *c*–plane oriented NRs over the AlGaN/AlN buffer layer and the inset figure shows the schematic sketch of the sample used for the present studies. The high resolution FESEM image shows (Fig. 5.1b) well faceted hexagonal and *c*–axis oriented NRs with smooth surface morphology, separated from each other with an average distance of ~200–300 nm. In addition, the individual NRs possess sharp edges (similar to saw–tooth edges) at the corners of the hexagon with a separation of ~200 nm (Fig. 1(b)). The typical height of vertically aligned and *c*–axis oriented NRs varies between 300–500 nm, as shown in the cross–sectional view of NRs obtained in the dark field mode of STEM detector within FESEM (figure 5.1b).

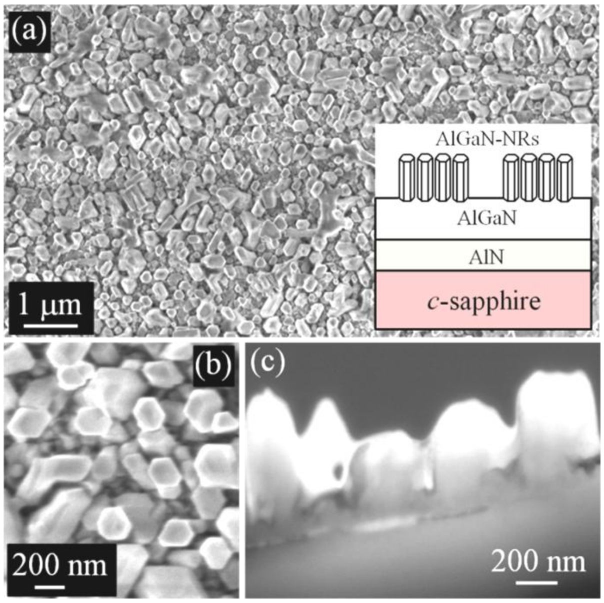

Figure 5.1 The FESEM images of 1D NRs. (a) Low magnification image with the distribution of NRs over the AlGaN/AlN buffer layers. (b) Top view of hexagonal NRs with sharp edges. (c) The high resolution STEM dark field image showing cross–sectional view of vertically aligned NRs.

A focused beam of Ga^+ ions (30 kV and 21 nA) was used to prepare the electron transparent AlGaN NR specimen for HRTEM studies. The final cleaning of the electron transparent specimen was performed using a low energy Ga^+ beam (2 kV and 9 pA) to minimize the beam damage to the specimen. Further, the electron transparency of the specimen was substantiated using a scanning transmission electron microscope (STEM) detector within FESEM. The typical height of vertically aligned and *c*–axis oriented NRs varies between 300–500 nm, as shown in the cross–sectional view of NRs obtained in the dark field mode of STEM detector within FESEM (Fig. 5.1c). A typical low magnification TEM micrograph is shown (Fig. 5.2a) for a cross–sectional NR attached to the Cu grid. The SAED pattern of the NR (Fig. 5.2b), recorded from the encircled portion of NR (Fig. 5.2a), is indexed to wurtzite phase of single crystal AlGaN with zone axis along [01-10]. The HRTEM image is shown for a typical NR (Fig. 5.2c). The corresponding inverse Fourier transform (IFT) image (Fig. 5.2d) for the selected area, marked in the figure 5.2c, shows an interplanar spacing of 2.71 Å corresponding to the (10-10) planes of AlGaN.

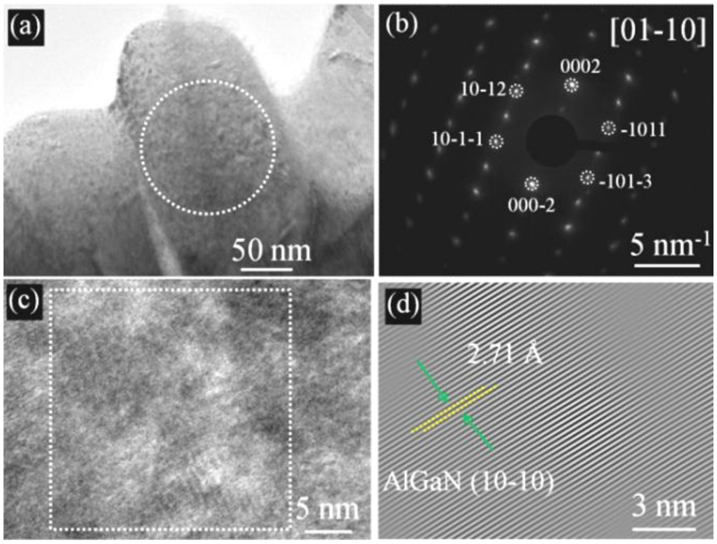

Figure 5.2 (a) The bright field TEM image of NR and its encircled portion used for SAED (b) The SAED pattern of NR indexed to wurtzite phase of AlGaN with a zone axis of [01-10] (c) The HRTEM image of NR and its marked square portion used for IFT (d) The IFT image of NR shows the (10-10) plane of AlGaN.

The elemental analysis was carried out from the recorded EELS spectra of AlGaN NR for further confirmation of its constituent elements namely, Al, Ga and N. The Al–*K*,[15] and N–*K* edges,[15] present in the EELS spectra are shown in Figs. 5.3a, and 5.3b, respectively. It is very difficult to record an adequate EELS signal from such an element with relatively high atomic number (Z=31). Thus, in order to understand the exact compositional details of the AlGaN NR along with Ga, we carried out the energy dispersive spectroscopy (EDS; Apollo X Silicon Drift Detector) analysis (Fig. 5.3c). Corresponding at% of Al, Ga and N in the NRs were found to be ~58.11(8.87), ~1.99(11.82) and ~39.90(6.09), respectively.

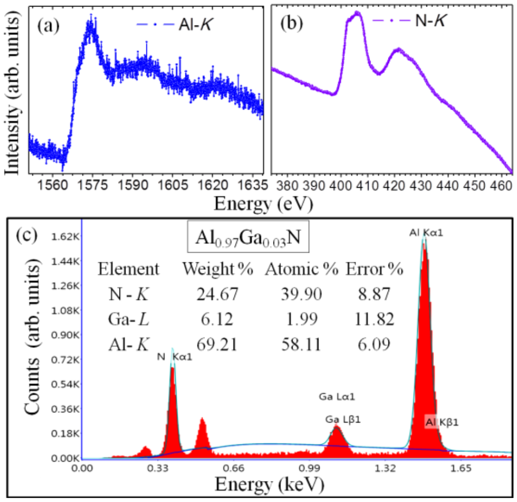

Element	Weight %	Atomic %	Error %
N - *K*	24.67	39.90	8.87
Ga- *L*	6.12	1.99	11.82
Al- *K*	69.21	58.11	6.09

Figure 5.3. The elemental and compositional analysis of AlGaN NR. The EELS spectra for (a) Al–*K*, and (b) N–*K* edges and (c) The EDS spectra

Consequently, the compositions of NRs are close to $Al_{0.97}Ga_{0.03}N$ and hence its optical properties are expected to depend on the band bowing formalism of random alloy model with respect to the constituent elements present in it.[15-18]

5.2.1 Effect of periodicity of the NRs

In order to investigate the nature of vibrational modes in the $Al_{0.97}Ga_{0.03}N$ NRs, Raman spectroscopic studies were performed in presence of air as the surrounding medium with ε_m= 1.00 (Fig. 5.4a). The sample excitation as well as the scattered spectra was collected using a 50X objective (Olympus 50X) with a numerical aperture (N.A.) value of 0.35 and a working distance of 18 mm. The corresponding laser beam diameter (d = 1.22λ/N.A.) emanated from the objective for an excitation wavelength (λ) of 514.5 nm was ~1.80 μm.[19] Raman modes centered around 656 and 883 cm^{-1} are assigned to the symmetry allowed AlN–E_2^H and AlN–A_1(LO) mode, respectively.[15-19] Moreover, two relatively intense and broad peaks, observed between the allowed E_2^H and A_1(LO) mode, are deconvoluted with Lorentzian function and are found to be centered at around 763 and 846 cm^{-1} (Fig. 5.4a).

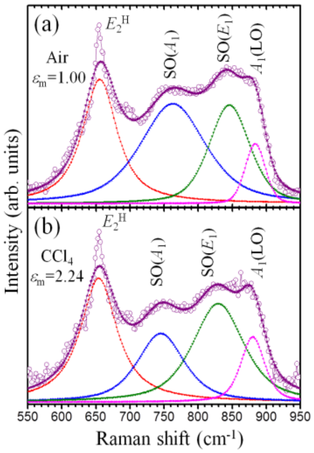

Figure 5.4 Raman spectra of 1D $Al_{0.97}Ga_{0.03}N$ NRs in different dielectric media (a) air (ε_m= 1.00) and (b) CCl_4 (ε_m=2.24)

The intermediate peaks, however were red shifted to around 745 and 830 cm^{-1} (Fig. 5.4b) with an increase in dielectric constant of the surrounding medium (ε_m = 2.24) using CCl_4 as the surrounding medium without any significant changes in the wave numbers of symmetry allowed modes in the spectrum. In order to investigate the nature of the unidentified phonon modes for $Al_{0.97}Ga_{0.03}N$ NRs, we use the general expression for the frequency of SO phonon mode for a 1D nanostructure to simulate its dispersion relation and is given by,[2-4,20,21]

$$\omega_{SO}^2 = \omega_{TO}^2 \frac{\varepsilon_0 - \rho_{nx}\varepsilon_m}{\varepsilon_\infty - \rho_{nx}\varepsilon_m} \qquad \text{......................................} \ (5.1)$$

where ω_{TO} is the $TO_{q=0}$ phonon mode frequency; ε_0 and ε_∞ are the static and high–frequency dielectric constants of the material, respectively; ρ_{nx} is a mathematical function of integral multiples of x as given below,[2-4,20,21]

$$\rho_{nx} = \frac{K_0^{'}(x) I_0(x)}{K_0(x) I_0^{'}(x)} = -\frac{K_1(x) I_0(x)}{K_0(x) I_1(x)} \qquad \text{..} \ (5.2)$$

where $I_j(x)$ and $K_j(x)$ (j = 0, 1) are the modified Bessel functions and $x = qr$ (r is the radius of the NRs and q is the wave vector responsible for the surface perturbations and hence the generation of SO phonon modes).[2-4,20,21] The values of ε_0 = 8.512 and ε_∞ = 4.621 for $Al_{0.97}Ga_{0.03}N$ NRs were calculated in accordance with the relative percentage of Al and Ga present in the system. The frequency values of A_1(TO) and E_1(TO) modes of A_1 and E_1 symmetries for $Al_{0.97}Ga_{0.03}N$ sample are considered as 611 and 671 cm^{-1}, respectively.[15-19]

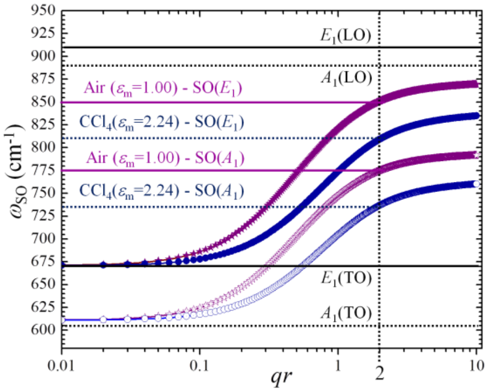

Figure 5.5 Dispersion curve for the SO modes of 1D $Al_{0.97}Ga_{0.03}N$ NRs in different dielectric media, air (ε_m= 1.00) and CCl_4 (ε_m=2.24)

The dispersion curves of SO modes (Fig. 5.5) corresponding to the frequency values of both A_1(TO) and E_1(TO) modes are simulated using the Equation (5.1). The nature of dispersion curves for SO modes of $Al_{0.97}Ga_{0.03}N$ NRs are also studied in two different dielectric media [air (ε_m = 1.00) and CCl_4 (ε_m = 2.24)] (Fig. 5.5)

5.2.2 Effect of dielectric constant of the medium

The surface phonons propagating through the surface of individual NRs may experience a periodicity of ~200 nm due the presence of saw–tooth like sharp edges of hexagonal nanostructures. In addition to that, the surface phonons propagating through the interface of AlGaN buffer layer as well as NRs can also face a dielectric contrast variation due to the periodicity (measured as the integral multiples of 200 nm) of NR–air–NR row and column like arrangement. In the present study, the assumed periodicity (λ) is the integral multiples of ~200 nm = 200×10^{-7} cm of the separation between the corner edges of hexagonal NR (Fig. 5.1b). This periodicity can also be represented in terms of the integral multiple of the separation (~200–300 nm) between the individual NRs (Fig. 5.1(b). Therefore, the a dielectric contrast variation due to the presence of NR–air–NR row and column like arrangement of the hexagonal $Al_{0.97}Ga_{0.03}N$ NRs can also be considered as an equivalent periodicity responsible for the surface modulations. The surface modulations of the sample may absorb the phonon momentum in terms of quantized units of $q = 2\pi/\lambda$.[1-5] Therefore, the calculated value of q = 314×10^{3} cm^{-1} is the Fourier component of the surface potential responsible for the surface perturbations leading to the formation of SO phonon modes. The major contribution for the intensity of SO phonons is expected to be originated due to the presence of sharp corner edges of the NRs. In addition to that, a significant contribution for the SO mode intensity can also be originated from the NR–dielectric medium (air/CCl_4) interface region over the AlGaN buffer layer of the sample. Since, the approximate radius of the hexagonal $Al_{0.97}Ga_{0.03}N$ NRs are considered as ~100 nm and the corresponding value of qr = 2.0, as indicated by the vertical dotted line in the figure 5.5. Since, the laser beam diameter (~1.80 μm) of excitation source is higher than the periodicity (λ~200 nm) of $Al_{0.97}Ga_{0.03}N$ NRs; the observed modes may have originated away from the Brillouin zone centre of the unit cell due to the breakdown of the translational symmetry of the surface potential. Incidentally, the observed intermediate modes in the Raman spectrum match well with the theoretically calculated values of SO modes corresponding to the qr value of 2.0 (Fig. 5.5). In the case of air as the dielectric medium, the calculated wave number values for SO(A_1) and SO(E_1) modes are ~775 and ~850 cm^{-1}, respectively. Similarly, in the case of CCl_4 as the surrounding medium, the corresponding values are red shifted to ~735 and 810 cm^{-1}, respectively. Therefore, the broad peaks observed around 763 and 846 cm^{-1} in the Raman spectrum of $Al_{0.97}Ga_{0.03}N$ NRs in the air medium (Fig. 5.4a) are assigned as SO(A_1) and SO(E_1) modes, respectively. Consequently, similar type of modes of around 745 and 830 cm^{-1} (Fig. 5.4b) in the Raman spectrum of $Al_{0.97}Ga_{0.03}N$ with CCl_4 as the surrounding medium, are also assigned as SO(A_1) and SO(E_1) modes, respectively. The observed red shift in SO mode frequencies of around 16–18 cm^{-1} in the Raman spectra of $Al_{0.97}Ga_{0.03}N$ NRs with CCl_4 (ε_m= 2.24), as the surrounding medium, compared to that of air (ε_m= 1.00) is because of the change in ε_m. The SO modes show red shift as the ε_m is increased while the peak position of the symmetry allowed AlN–A_1(LO) mode do not change from its initial value. This observation further confirms that the intermediate phonon modes, observed in the Raman spectra, are the SO phonon modes.[1-5,20,21,31] The small discrepancy (10–20 cm^{-1}) in the observed and calculated SO mode values for $Al_{0.97}Ga_{0.03}N$ NRs with the medium of CCl_4 is well within the error, particularly considering the large full width at half maxima of the SO modes. Thus, the technique may also be useful for studying the properties of an unknown dielectric material used as surrounding medium.

5.3 Interface optical phonon mode in 2D $[AlN/GaN]_{20}$ and $[Al_{0.35}Ga_{0.65}N/Al_{0.55}Ga_{0.45}N]_{20}$ multi–QW structures

5.3.1 Effect of dielectric constant of the medium

The vibrational properties of the samples with MQW structures of *c*–plane oriented $[GaN(\sim1.25\ nm)/AlN(\sim2.0\ nm)]_{20}$ (schematic in Fig. 5.6a) and $[Al_{0.35}Ga_{0.65}N(\sim1.75\ nm)/Al_{0.55}Ga_{0.45}N(\sim2.0\ nm)]_{20}$ (Fig. 5.6b showing schematic as well as a TEM micrograph at the outset) SLs grown using PAMBE technique,[11-15,32] were probed by Raman spectroscopy at 80K. The periodic bi–layers of 3.25 and 3.75 nm are measured for $[GaN/AlN]_{20}$ and $[Al_{0.35}Ga_{0.65}N/Al_{0.55}Ga_{0.45}N]_{20}$ MQWs, respectively.[32] The spectral lines centered around 570, 659 and 890 cm^{-1} (Figs. 5.6c and 5.6d) are assigned to be the allowed symmetric Raman modes of GaN–E_2^H, AlN–E_2^H and AlN–A_1(LO) modes of wurtzite phase, respectively.[15-19] The peak centered at ~750 cm^{-1} is from the sapphire substrate. The mode is observed, as the MQW samples with wideband gap materials (band gap >3.47 eV at room temperature) are transparent to 514.5 nm (2.41 eV) excitation.

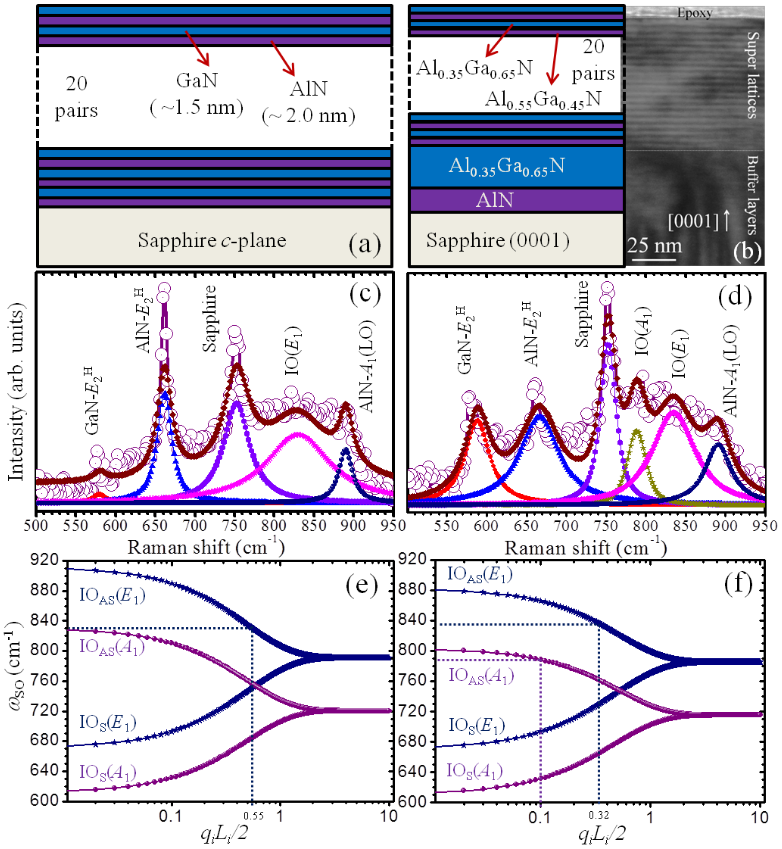

Figure 5.6 The schematic representation of *c*–plane oriented MQW structures of (a) $[GaN/AlN]_{20}$ and (b) $[Al_{0.35}Ga_{0.65}N/Al_{0.55}Ga_{0.45}N]_{20}$ SLs. Outset shows a TEM micrograph of the MQW. (c) and (d) the corresponding Raman spectra for 514.5 nm excitation recorded at 80K. (e) and (f) the respective simulated dispersion relation for the IO phonon modes. Dotted horizontal and vertical lines are drawn to indicate observed IO phonon modes and corresponding $q_iL_i/2$ values, respectively.

For understanding the additional broad peaks (Figs. 5.6c and 5.6d) observed around ~788 and ~830–834 cm^{-1}, we simulated the dispersion curves for the IO phonon modes by considering ε_0 and ε_∞ as the respective static and high frequency value of dielectric constants ($\varepsilon(\omega)$) of the material. The symmetric (S) and asymmetric (AS) modes of IO phonon in 2D nanostructures are defined by the following equations,[2-5,26-30]

$$\omega_{IO}^2(q)_S = \omega_{TO}^2\left[\frac{\varepsilon_0 \tanh(q_i L_i/2) + \varepsilon_m}{\varepsilon_\infty \tanh(q_i L_i/2) + \varepsilon_m}\right] \quad \ldots\ldots\ldots\ldots\ldots\ldots\ldots (5.3)$$

$$\omega_{IO}^2(q)_{AS} = \omega_{TO}^2\left[\frac{\varepsilon_0 \coth(q_i L_i/2) + \varepsilon_m}{\varepsilon_\infty \coth(q_i L_i/2) + \varepsilon_m}\right] \quad \ldots\ldots\ldots\ldots\ldots\ldots\ldots (5.4)$$

where L_i (i = 1, 2) is the edge width of the rectangular QW plates whose growth direction is considered to be along the z–direction; q_i (i = 1, 2) is the IO phonon wave–vectors in the QW structures. In order to compute the dispersion relations (Eqns. (5.3) and (5.4)) for the IO phonon modes, it is assumed that the similar parity for the surface potentials of TO and LO phonon modes in the two mutually orthogonal directions ($q_1^2 + q_2^2 = q^2$; $q_1L_1 = q_2L_2$).[2-5,26-30]

The ε_m follows the Lyddane–Sachs–Teller (LST) relation corresponding to A_1 and E_1 symmetries.[1-5] The values of ε_0 and ε_∞ for AlN and GaN are considered from the available reports for assigning the dielectric contrast for the [GaN/AlN]$_{20}$ MQWs.[17] Similarly, the dielectric constants for the different 2D medium for [$Al_{0.35}Ga_{0.65}N/Al_{0.55}Ga_{0.45}N$]$_{20}$ structures are estimated on the basis of reported values of AlN and GaN,[17] followed by the numerical calculations with respect to the different Al percentage in the compositions of 2D layers in the MQW. The calculated values for ε_0 and ε_∞ for each sample are shown in the Table 5.1. The corresponding frequency values of A_1(TO) and E_1(TO) symmetry modes for different MQW samples are 611 and 671 cm^{-1}, respectively, taken under consideration by the two–mode behavior of the random alloy model for AlGaN.[15-19] With the help of the above tabulated data, the dispersion relations for IO phonon modes are simulated by using the Equations (5.3) as well as (5.4), and then the resultant curves are plotted for the respective sample as shown in the Figs. 5.6e and 5.6f.

Table 5.1: The dielectric constants for AlN, GaN and AlGaN with different stoichiometry.

Materials	ε_0	ε_∞
AlN	8.50	4.60
GaN	8.90	5.40
$Al_{0.55}Ga_{0.45}N$	~ 8.72	~ 5.04
$Al_{0.50}Ga_{0.50}N$	~ 8.70	~ 5.00
$Al_{0.35}Ga_{0.65}N$	~ 8.64	~ 4.88

The IO phonon mode for $[GaN/AlN]_{20}$ MQWs are calculated by considering AlN QWs as the material of interest and GaN QWs as the surrounding medium. Similarly, in the case of $[Al_{0.35}Ga_{0.65}N/Al_{0.55}Ga_{0.45}N]_{20}$ MQWs, $Al_{0.55}Ga_{0.45}N$ and $Al_{0.35}Ga_{0.65}N$ QWs are considered as the material of interest and the surrounding medium, respectively. The peak centered around ~830 cm^{-1}, observed in the Raman spectra of $[GaN/AlN]_{20}$ MQWs (Fig. 5.6c), may originate because of the presence of an IO phonon mode of E_1 symmetry (IO(E_1)) as indicated in the calculation. Similarly, the peaks centered at ~788 and ~834 cm^{-1}, observed in the Raman spectra of $[Al_{0.35}Ga_{0.65}N/Al_{0.55}Ga_{0.45}N]_{20}$ MQWs (Fig. 5.6d), may have evolved because of the simultaneous presence of IO phonon mode of A_1 symmetry (IO(A_1)) as well as IO(E_1) mode, respectively. The origin of the additional IO(A_1) peak in the Raman spectra in the

$[Al_{0.35}Ga_{0.65}N/Al_{0.55}Ga_{0.45}N]_{20}$ sample compared to that of the $[GaN/AlN]_{20}$ MQW may be because of the presence of additional $Al_{0.35}Ga_{0.65}N$(~320 nm)/AlN(~200 nm) buffer layer present on the sapphire substrate (Fig. 5.6b). In order to confirm it, a bi–layer thin film of $Al_{0.50}Ga_{0.50}N$(~300 nm)/AlN(~200 nm) (schematic Fig. 5.7a) was also studied for its symmetry allowed Raman phonon modes of AlN–E_2^H and AlN–A_1(LO) along with the presence of IO modes (Fig. 5.7b).

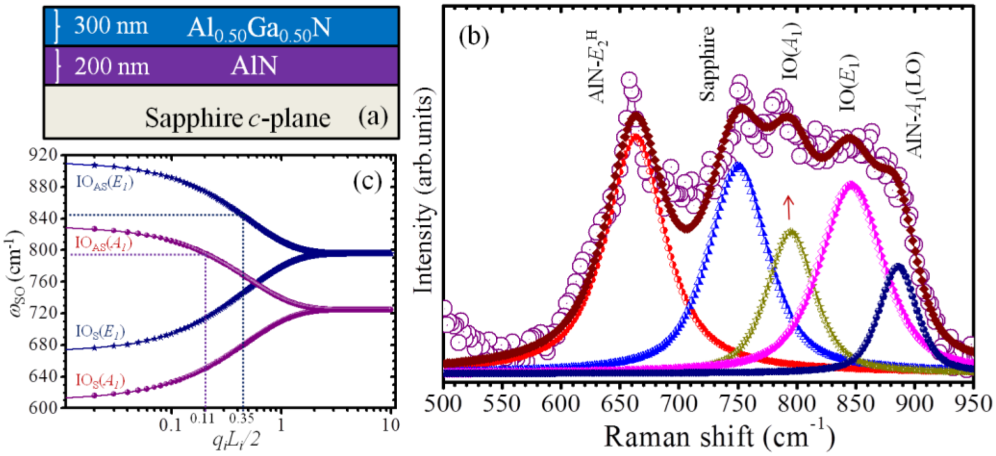

Figure 5.7 (a) The schematic representation of thin film structures of $Al_{0.50}Ga_{0.50}N$/AlN (b) The Raman spectra for 514.4 nm excitation recorded at 80K and (c) the respective simulated dispersion relation for the IO phonon modes. Dotted horizontal and vertical lines are drawn to indicate observed IO phonon modes and corresponding $q_iL_i/2$ values, respectively.

Similarly, the dispersion curve (Fig. 5.7c) for IO phonons are simulated by considering AlN layer as the material of interest and $Al_{0.50}Ga_{0.50}N$ as the surrounding medium using the corresponding values of ε_0 and ε_∞ as shown in the Table 5.1. We could identify the mode frequencies of IO phonons, at IO(A_1) ~794 cm^{-1} with significant intensity and IO(E_1) at ~846 cm^{-1} (Fig. 5.7b). The distinct IO(A_1) mode with high intensity, observed for $Al_{50}Ga_{50}N$/AlN bi–layer sample, is close to the observed value of ~788 cm^{-1} in case of $[Al_{0.35}Ga_{0.65}N/Al_{0.55}Ga_{0.45}N]_{20}$ MQW sample. The small shift of ~6 cm^{-1} for IO(A_1) and ~13 cm^{-1} for IO(E_1) modes, observed in the $Al_{50}Ga_{50}N$/AlN bi–layer thin film as compared to those for $[Al_{0.35}Ga_{0.65}N/Al_{0.55}Ga_{0.45}N]_{20}$ MQW, may be because of the different dielectric constants in the layered structures with different Al contents (Table 5.1). Moreover, the broadening of IO(E_1) mode corresponding to the $[Al_{0.35}Ga_{0.65}N/Al_{0.55}Ga_{0.45}N]_{20}$ sample (Fig. 5.7b) may be because of the contribution originating from the IO(E_1) mode corresponding to the $Al_{0.35}Ga_{0.65}N$/AlN buffer layer. In this regard presence of a broad peak at ~846 cm^{-1} corresponding to the $Al_{50}Ga_{50}N$/AlN bi–layer sample may be noted (Fig. 5.7b).

5.3.2 Effect of the periodicity of interface layers

The periodic surface modulation and IOs of SL structures of 2D MQWs may lead to the relaxation of Raman selection rules because of the breakdown of translational symmetry of the surface potential,[1-5,28] and it is anticipated that the unidentified Raman modes observed in the recorded spectra from the MQWs belong to the above mentioned IO(A_1) and IO(E_1) phonon modes, respectively. The surface layers of MQWs and buffer layers absorb an additional momentum in terms of the quantized units of q ($=2\pi/\lambda$) and the expected edge lengths (L) corresponding to the IO(A_1) and IO(E_1) phonon modes are calculated for a periodicity of the surrounding medium separated with a thickness of the material of interest, λ ~2 nm (for QWs) and λ ~200 nm (for buffer layer and bi–layer thin film) (Table 5.2). The nature of IO(A_1) mode, observed in the $[Al_{0.35}Ga_{0.65}N/Al_{0.55}Ga_{0.45}N]_{20}$ SL, is attributed to the presence of MQW structure as well as the $Al_{0.35}Ga_{0.65}N$/AlN buffer layers present in it. Therefore, in case of the sample $[Al_{0.35}Ga_{0.65}N/Al_{0.55}Ga_{0.45}N]_{20,}$ the corresponding q and L values are calculated for IO(A_1) modes for a pair of layer thickness, λ ~2 and ~200 nm, respectively. The observed IO(A_1) mode wave number with significant intensity as well as the order of *q* and *L* (Table 5.2) match well with the sample which posses $Al_{0.50}Ga_{0.50}N$/AlN bi–layered thin film alone on the sapphire substrate (Fig. 5.7).

Table 5.2: The *q* and *λ* of the respective IO phonon modes observed in the Raman spectra of the MQW structures with an expected 2D plate length (*L*).

Substrate for all of the sample is sapphire	[GaN(~1.25 nm)/AlN(~2.0 nm)]$_{20}$		[$Al_{0.35}Ga_{0.65}N$(~1.75 nm)/$Al_{0.55}Ga_{0.45}N$(~2.0 nm)]$_{20}$ on $Al_{0.35}Ga_{0.65}N$(~300 nm)/ AlN(~200 nm) buffer layer		$Al_{0.50}Ga_{0.50}N$(~320 nm)/AlN(~200 nm)	
IO modes	$\omega_{IO}(A_1)$	$\omega_{IO}(E_1)$	$\omega_{IO}(A_1)$	$\omega_{IO}(E_1)$	$\omega_{IO}(A_1)$	$\omega_{IO}(E_1)$
Wave number	–	830	788 cm^{-1}	834 cm^{-1}	794 cm^{-1}	846 cm^{-1}
$x = qL/2$	–	0.55	0.10	0.32	0.11	0.35
λ (periodicity of surrounding medium)	–	2 nm	200 nm (buffer layer)	2 nm (QWs) 200 nm (buffer layer)	200 nm (thin film)	2 nm (QWs) 200 nm (thin film)
$q = 2\pi/\lambda$	–	3.14×10^{7} cm^{-1}	3.14×10^{5} cm^{-1}	3.14×10^{7} cm^{-1} and 3.14×10^{5} cm^{-1}	3.14×10^{5} cm^{-1}	3.14×10^{7} cm^{-1}
$L = 2x/q$ (nm)	–	35	637	20.38 (λ ~2 nm) 2038 (λ ~200 nm)	700	22.40 (λ ~2 nm) 2240 (λ ~200 nm)

The 2D shapes with finite *L* can be formed on the sample surface by the horizontal uneven irregularities generated during the growth period. The typical FESEM image of MQWs shows

(Fig. 5.8) the nanometer sized platelets uniformly distributed all over the horizontal surface of SLs and the surface protrusions are of the order of 10s to 100s of nm scale.

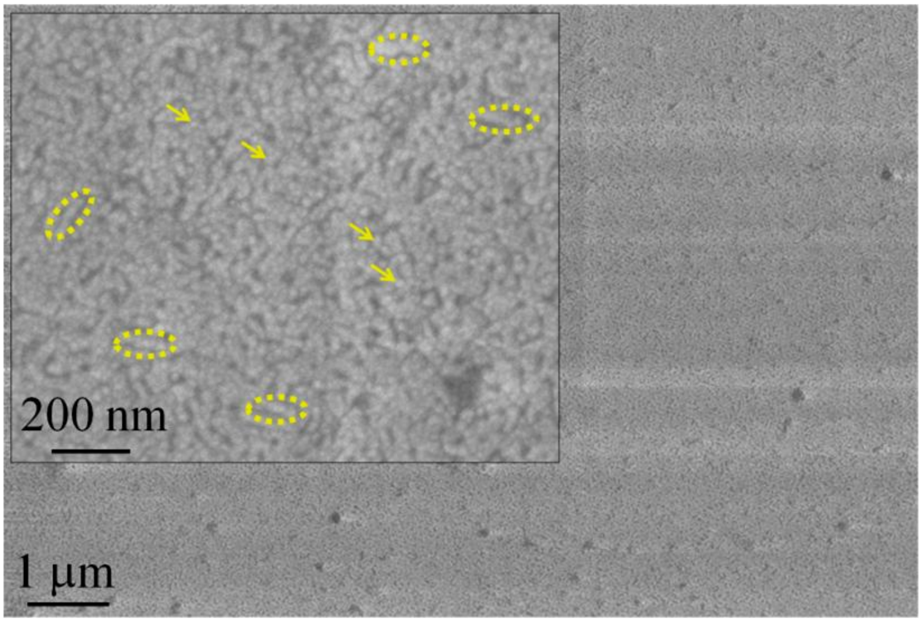

Figure 5.8 The typical FESEM image shows the morphology of the topmost surface layer of MQWs containing the nanometer sized platelets uniformly distributed all over the surface. The inset shows a high magnification image for the surface protrusions in the order of 10s (arrow head) to 100s (encircled portions) of nm. The integral multiples of nanometer sized protrusions also can act as a micron sized platelets (~2 μm).

The integral multiples of nanometer sized protrusions also can act as a micron sized platelets (~2 μm). Moreover, the required *L* values fall in the order of 10s and 100s of nanometers to a few micrometers (~2 μm). It is very important to notice that the spot size of the excitation laser (~2 μm) can easily cover the required area generated by the 2D plate lengths. The small shift in IO(E_1) phonon mode (~4 cm^{-1}) for $[Al_{0.35}Ga_{0.65}N/Al_{0.55}Ga_{0.45}N]_{20}$ compared to that for the $[GaN/AlN]_{20}$ MQWs is because of the difference in ε_m of the surrounding medium.[1-5,32] This red shift of the observed mode in between the allowed $(TO)_{q=0}$ and $(LO)_{q=0}$ Raman modes with increasing ε_m value, because of the change in the surrounding medium, can be considered as a further confirmation for the presence of IO mode.

5.4 Summary

In conclusion, the nature of SO phonon modes are investigated in the Raman spectra of $Al_{0.97}Ga_{0.03}N$ vertically aligned *c*–axis oriented hexagonally shaped 1D NRs. The dispersion relation for both SO(A_1) and SO(E_1) phonon modes with A_1 and E_1 symmetries, respectively for two different media, air and CCl_4 are simulated to match with the experimentally observed non–zone center (for wave vector, $q\neq0$) phonon modes in the Raman spectra. The origin of the SO phonon mode is because of the presence of sharp corner edges of the well–faceted hexagonal NRs with a periodicity (λ) of ~200 nm as well as the equivalent surface modulations generated due the integral multiples of the separation between the arrays of row and columnar like arrangement of NRs. The corresponding Furrier component of the surface potential, providing necessary surface perturbation in the NRs, is used successfully to estimate the SO modes. The observed red shift in the $q\neq0$ mode frequencies of around 16–18 cm^{-1} in the Raman spectra for $Al_{0.97}Ga_{0.03}N$ NRs in presence of CCl_4 with different dielectric constants of the surrounding medium compared to that for air, confirms the presence of SO mode in the observed Raman modes. Moreover, apart from the symmetry allowed Raman modes, the IO phonon modes are also observed in the Raman spectra of [GaN(~1.25 nm)/AlN (~2.0 nm)$]_{20}$ and [$Al_{0.35}Ga_{0.65}N$(~1.75 nm)//$Al_{0.55}Ga_{0.45}N$(~2.0 nm)]$]_{20}$ MQW structures. The dispersion relation for both IO(A_1) and IO(E_1) phonon modes for MQW structures are calculated and are matched with the experimentally observed IO phonon modes in the Raman spectra. For $[GaN/AlN]_{20}$ MQW structure, the IO(E_1) phonon mode alone is observed, whereas in case of $[Al_{0.35}Ga_{0.65}N/Al_{0.55}Ga_{0.45}N]_{20}$ MQW structure, both IO(A_1) and IO(E_1) are identified simultaneously. The red shift of IO mode (~4 cm^{-1}) of $[GaN/AlN]_{20}$ compared to that for $[Al_{0.35}Ga_{0.65}N/Al_{0.55}Ga_{0.45}N]_{20}$ MQW structure with the change in dielectric constant of the surrounding medium, further confirms the existence of IO modes in the observed Raman Spectra. The relative increase for intensity of IO(A_1) in [$Al_{0.35}Ga_{0.65}N/Al_{0.55}Ga_{0.45}N$]$_{20}$ MQW sample is evolved because of the presence of $Al_{0.35}Ga_{0.65}N$/AlN buffer layer in the sample, as confirmed with the observation of the similar IO(A_1) mode with higher intensity in the $Al_{0.50}Ga_{0.50}N$/AlN bi–layer thin film structure. The observation of the IO phonon modes is attributed to the relaxation of Raman selection rules because of the breakdown of translational symmetry because of the presence of the periodic interfaces and surface modulations of superlattice structure of MQWs. The integral multiples of the nanometer sized protrusions, uniformly distributed all over the horizontal surface of SLs, in the order of 10s and 100s of nanometers to a few micrometers (~2 μm) are found to act as the expected edge lengths responsible for the breakdown of symmetry.

5.5 References

[1] H. Zhu, J. Q. Ning, C. C. Zheng, S. J. Xu, S. M. Zhang and H. Yang, *Appl. Phys. Lett.* **2011**, 99, 113115

[2] S. Dhara, P. Sahoo, A. K. Tyagi and B. Raj *Nanowires–Implementation and Applications*, **2011**, *Ed.* Abbas Hashim, Intech Open Access, Croatia, http://www.intechopen.com/articles/show/title/surface–optical–modes–in–semiconductor–nanowires

[3] Q. Xiong, J. Wang, O. Reese, L. C. Lew Yan Voon and P. C. Eklund, *Nano Lett,* **2004**, 4, 1991

[4] R. Gupta, Q. Xiong, G. D. Mahan and P. C. Eklund, *Nano Letters.* **2003**, 3, 1745

[5] S. Bhattacharya, A. Datta, S. Dhara and D. Chakravorty, *J. Raman Spectrosc.* **2011**, 42, 429

[6] S. M. Komirenko, K. W. Kim, M. A. Stroscio and M. Dutta, *Phys. Rev. B* **1999**, 59, 5013

[7] J. J. Shi, *Phys. Rev. B* **2003**, 68, 165335

[8] D. A. Miller, *Optical physics of quantum wells*. **1996**, Institute of Physics, London,

[9] T. Ruf, *Phonon Raman Scattering in Semiconductors, Quantum Wells and Superlattices*. **1998**, Springer–Verlag, Berlin

[10] A. K. Arora, M. Rajalakshmi and T. Ravindran, *Encyclopedia of Nanoscience and Nanotechnology*, **2004**, 8, 499

[11] P. Pramanik, S. Sen, C. Singha, A. S. Roy, A. Das, S. Sen, D. V. Sridhara Rao and A. Bhattacharyya, *IEEE J. Quant. Electron.* **2016**, 52, 4300206

[12] P. Pramanik, S. Sen, C. Singha, A. S. Roy, A. Das, S. Sen, A. Bhattacharyya, D. Kumar and D. V. Sridhara Rao, *J. Cryst. Growth* **2016**, 439, 60

[13] M. A. Khan, *phys. stat. sol. (a)* **2006**, 203, 1764

[14] H. Hirayama, N. Noguchi, T. Yatabe, and N. Kamata, *Appl. Phys. Express.* **2008**, 1, 051101

[15] A. K. Sivadasan, A. Patsha, S. Polaki, S. Amirthapandian, S. Dhara, A. Bhattacharya, B. K. Panigrahi and A. K. Tyagi, *Cryst. Growth Des.* **2015**, 15, 1311

[16] V. Yu. Davydov, I. N. Goncharuk, A. N. Smirnov, A. E. Nikolaev, W. V. Lundin, A. S. Usikov, A. A. Klochikhin, J. Aderhold, J. Graul, O. Semchinova and H. Harima, *Phys. Rev. B* **2002**, 65, 125203

[17] J. Wu, *J. Appl. Phys.* **2009**, 106, 011101

[18] A. K. Sivadasan, G. Mangamma, S. Bera, M. Kamruddin and S. Dhara, *J. Appl. Phys.* **2016**, 119, 174304

[19] A. K. Sivadasan, A. Patsha and S. Dhara, *App. Phys. Lett.* **2015**, 106, 173107

[20] P. Sahoo, S. Dhara, C. R. Das, S. Dash, A. K. Tyagi, B. Raj, P. Chandramohan and M. P. Srinivasan, *Intl. J. Nanotechnol.,* **2010**, 7, 823

[21] S. Sahoo, S. Dhara, A. K. Arora, P. Chandramohan, M. P. Srinivasan and R. Krishnan, *Appl. Phys. Lett.* **2010**, 96, 103113

[22] S. E. Wu, Y. W. Huang, T. H. Hsueh, S. Dhara, Y. F. Lai, C.Y. Wang and C. P. Liu, *J. Raman Spectrosc.* **2009**, 40, 2044

[23] S. Sahoo, M. S. Hu, C. W. Hsu, C. T. Wu, K. H. Chen, L. C. Chen, A. K. Arora and S. Dhara, *Appl. Phys. Lett.* **2008**, 93, 233116

[24] C. L. Hsiao, L. W. Tu, T. W. Chi, M. Chen, T. F. Young, C. T. Chia and Y. M. Chang, *Appl. Phys. Lett.* **2007**, 90, 043102

[25] I. M. Tiginyanu, A. Sarua, G. Irmer, J. Monecke, S. M. Hubbard, D. Pavlidis and V. Valiaev, *Phys. Rev. B* **2001**, 64, 233317

[26] R. Ruppin and R. Englman, *Rep. Prog. Phys.* **1970**, 33, 149

[27] B. E. Sernelius, *Surface Modes in Physics*, **2001**, Wiley–VCH: New York,

[28] C. H. Ho, P. Varadhan, H. H. Wang, C. Y. Chen, X. Fang and Jr–H. He, *Nanoscale*, **2016**, 8, 5954

[29] R. Mata, A. Cros, K. Hestroffer and B. Daudin, *Phys. Rev. B* **2012**, 85, 035322

[30] G. D. Mahan, R. Gupta, Q. Xiong, C. K. Adu and P. C. Eklund, *Phys. Rev. B* **2003**, 68, 073402

[31] A. K. Sivadasan, C. Singha, K. G. Raghavendra, S. Amirthapandian, A. Bhattacharyya, A. Dasgupta and S. Dhara "*Surface optical phonon modes in hexagonal shaped 1D* $Al_{0.97}Ga_{0.03}N$ *nanorods*", (*Communicated*)

[32] A. K. Sivadasan, C. Singha, A. Bhattacharyya, and S. Dhara, *Phys. Chem. Chem. Phys*, **2016**, 18, 29864

CHAPTER 6

LIGHT–MATTER INTERACTIONS IN THE SUB–DIFFRACTION REGIME

"*Matter is Energy ...Energy is Light...We are all Light Beings*" ....Albert Einstein

6.1 Introduction

Till now the nanoscale focusing and imaging in the sub–diffraction limit is achieved mainly with the help of plasmonic field enhancement by confining the light assisted with noble metal nanostructures.[1-7] In this context, the proximity induced PL intensity enhancement can be understood by assuming the existence of reasonably long lived photons in the intervening space between the NWs.[8] A non–zero non–equilibrium population of such photons may cause stimulated emission leading to the enhancement of PL emission.[8] The enhancement of PL emission facilitates far–field spectroscopic imaging of a single semiconductor AlGaN NW of sub–wavelength. An optical characterization tool of Raman spectroscopy, with extremely weak scattering cross section tool, is not popular to analyze scattered signal from a single nanostructure in the sub–diffraction regime. In this regard, plasmonic assisted characterization tools are only relevant in spectroscopic studies of nanoscale object in the sub–diffraction limit.[1-8] The NSOM technique is not only a tool for imaging of sub–diffraction limited objects, but also a prominent characteristic tool for understanding the intrinsic properties of the nanostructures.[1-7]

The present chapter includes the far–field spectroscopic PL imaging of a single semiconductor AlGaN NW using the peak intensity of free excitonic (FE) emission in the sub–wavelength scale. In case of the optical confinement effect, a non–zero non–equilibrium population of long lived photons is envisaged to influence the increased PL emission intensity from the single NW. In a far–field optical configuration, we report the polarized RRS of a single AlGaN NW to understand the crystallographic orientations in the sub–diffraction length scale. The present investigations also include the studies of the light–matter interaction of an isolated single and semiconductor AlGaN NW along with metallic Au NP catalysts in the near field regime by using the NSOM technique with a laser excitation of 532 nm. In order to understand the light–matter interaction of AlGaN NW, we invoked the semiconductor band picture by analysing the different energy states related to native defects with the help of PL measurement from a single AlGaN NW. We also studied the effects of plasmonics in the NSOM images of Au NPs which was involved in the VLS growth mechanism of AlGaN NWs.

6.2 Photonic confinement of UV–light

6.2.1 The proximity induced optical confinement between the interaction area of an array of NWs

The FESEM image (Fig. 6.1a) shows the uniform and mono–dispersed NWs all over the substrate. The NWs with a narrow size distribution of 100 (±10) nm are shown (Fig. 6.1b). The high resolution image (outset of Fig. 6.1b) of the cylindrically shaped AlGaN NW shows very smooth surface morphology with an Au NP at the tip of the NW (Fig. 6.1b).

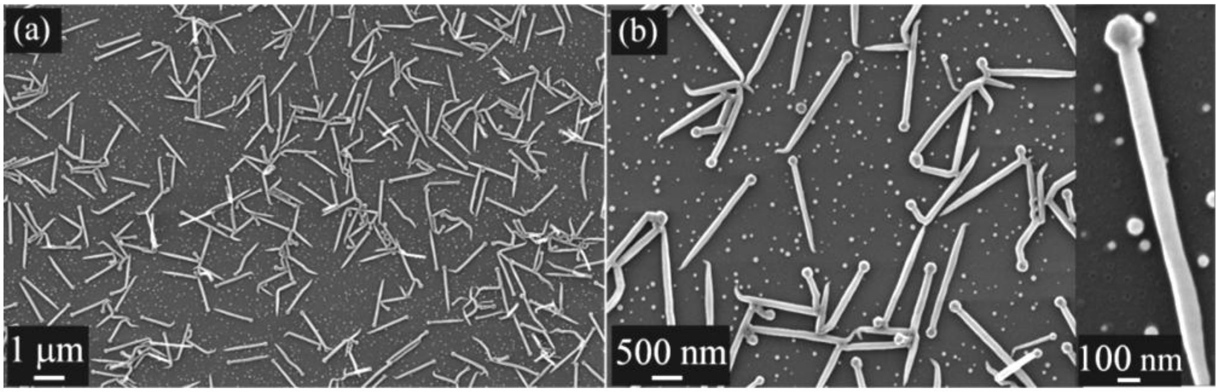

Figure 6.1 (a) Typical low magnification image shows the uniform and mono–dispersed NWs (b) AlGaN NWs with a smooth and narrow size distribution; a single NW with a diameter of 100 (±10) nm shown in the outset.

The Au NPs participated in the VLS growth process of the AlGaN NWs,[9] which have uniform size of ~120 nm and was found to be well separated from each other. The interface region between the Au NPs and AlGaN NWs is negligible compared to the total area of the NW.

The polarized PL measurements at 300K for the single AlGaN NW (schematic, Fig. 6.2) are performed in two different configurations of $Z(XX)\bar{Z}$ and $Z(XY)\bar{Z}$, which are considered as parallel (π) and perpendicular (σ) polarizations, respectively. The long axis of cylindrical NWs is considered as X direction, whereas the incident and backscattered light propagation directions are measured along the Z and $\bar{Z}$ directions, respectively. The parallel, $Z(XX)\bar{Z}$ and perpendicular, $Z(XY)\bar{Z}$ polarizations were configured using a half wave plate and a polarizer kept in the backscattering geometry, as shown in the schematic of the experimental setup used for the measurements (Fig. 6.2). In the $Z(XX)\bar{Z}$ configuration, the excitation electric field vector (E_e) is parallel to the long axis ($E_e \| X$, π–polarization) and E_e is perpendicular to the horizontal X–axis ($E_e \perp X$, σ–polarization) in $Z(XY)\bar{Z}$ configuration.[10-16] In both cases, the incident direction (wave vector) of laser light is perpendicular to the horizontal axis ($k \perp X$) of AlGaN NW.

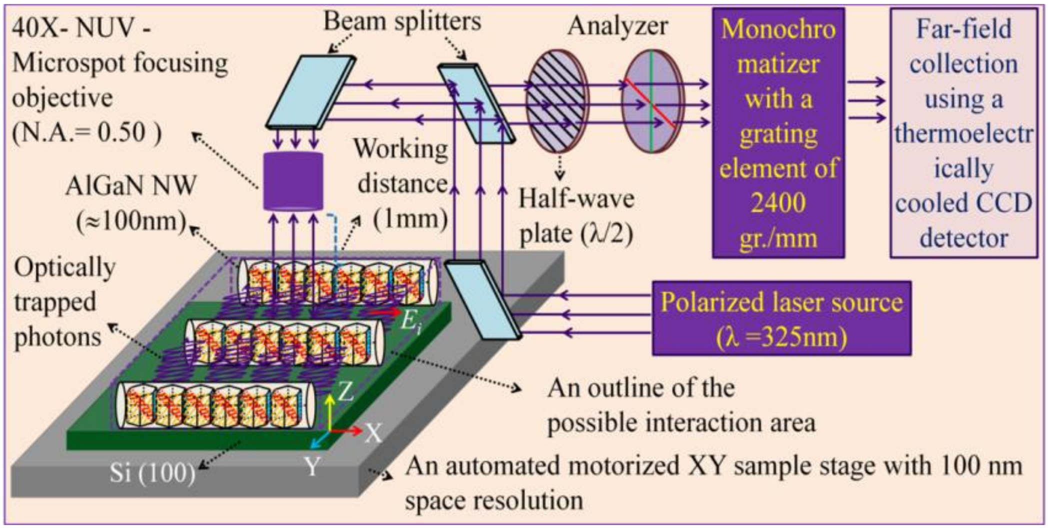

Figure 6.2 The schematic representation of the experimental setup for recording single NW spectra and imaging using polarized PL spectroscopy. The outline of interaction area depicts the long lived photons leading to the optical confinement effect in between the semiconductor AlGaN NW columns.

It was found that the polarized PL peak intensity value for a single NW was higher for π–polarization, as compared to that of the σ–polarization (Fig. 6.3a).[10-16] This observation is typical 1D semiconductor NWs and is because of the optical confinement of polarized light within the material, due to variation of refractive index of NWs and its surrounding media.[10-16] The optical image of the mono–dispersed AlGaN NW with a separation of ~2 μm, using an objective of 100× with N.A. value of 0.85, is shown in the inset of figure 6.3a. The single NW, used for recording the PL spectra, is indicated by a dotted arrow. It was ensured that the individual NWs were well separated (~2 μm) compared to the excitation laser spot size of ~0.80 μm to receive a PL spectrum of a single NW alone. Considering around 5.0% error for the Gaussian spreading of incident beam diameter, the maximum possible laser beam diameter can be calculated as ~0.84 μm. Thus, it was ensured that the PL spectra were collected from the centre portion of a single NW with minimum interference of any other signals that might be contributed from adjacent NWs. The peak observed at ~3.55 eV is due to the recombination of free exciton (FE).[9] A tiny peak centered at 3.73 eV is assigned to

A_1(LO) mode of GaN.[9] The peak observed at ~3.30 eV is identified with electronic transition (DAP) from a shallow donor state of nitrogen vacancy (V_N) to a deep acceptor state of Ga vacancy (V_{Ga}).[9]

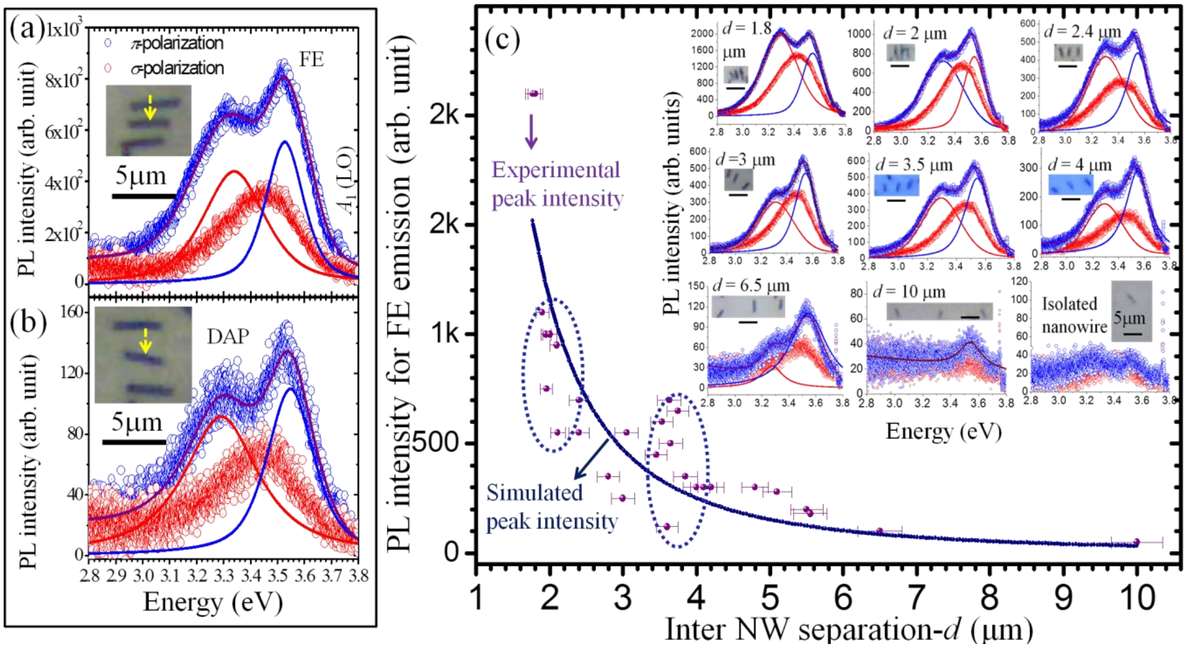

Figure 6.3 Polarized PL spectra for *π*– and *σ*–polarized configurations of a single AlGaN NW for the inter–NW separations of (a) 2 µm and (b) 4 µm. Inset shows the optical image of mono–dispersed NWs on the Si(100) substrate. The single NW selected for the polarized PL spectra is indicated by an arrow. (c) The statistical dependence of PL intensity corresponds to FE emission with respect to the separation of consecutive NWs. Inset shows PL spectra correspond to different separations and the scale bars in the inset are equal to a length of 5 µm.

The variation in intensity for different polarization configurations depends on the material geometry as well as the anisotropy of the medium. Thus, the intensity of *π*–polarization (I_π) can be very different from that of the *σ*–polarization (I_σ) due to the confinement effect, as mentioned earlier. The observed polarization anisotropy is typically defined in terms of the polarization ratio ($\rho = I_\pi - I_\sigma / I_\pi + I_\sigma$; also called as the degree of polarization).[10-16] For the present study, the polarization ratio of AlGaN NW (~100 nm) for the PL emission was calculated as ~0.533.

A strong correlation of the PL intensity (Figs. 6.3a and 6.3b) with the proximity to other NWs was observed in the present study. An increase in the PL intensity by one order is observed, when the separation from the nearest neighbour NW is decreased from 4 μm (inset Fig. 6.3b) to 2 μm (inset Fig. 6.3a). The similar experiments were carried out for a large number of times with different separation between the consecutive NWs to get a good statistics (Fig. 6.3c). We have plotted FE emission intensity at the peak energy versus the separation between the NWs (d) within the limit of finite error using statistics from the measurements at different spots along the wires (Fig. 6.3c). The inset of figure 6.3c shows the representative PL spectra observed for few typical inter–NW separations. It is clear that the observed emission intensities of PL spectra increase with decreasing d values. Interestingly, the PL intensity varies inversely proportional the interaction area of ($l \times d$), where l and d are the NW length and the inter–NW separation, respectively (Fig. 6.3c). However, the scattering of the data–points observed in the PL intensities with respect to d is possibly because of the misalignment of NWs from its perfect parallel configuration with each other (as indicated by the error bars for the x–scale in figure 6.3c).We have also confirmed $1/d^2$ dependence of the PL intensities with inter–NW separation extending down to sub–micron size using scanning probe microscopy coupled to a Raman spectrometer (Fig. 6.4).

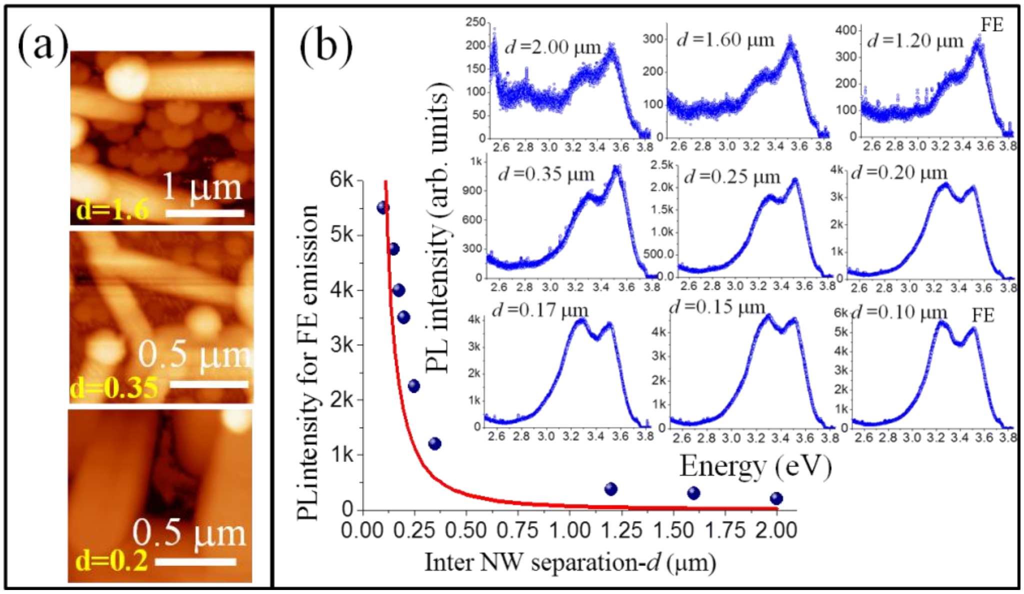

Figure 6.4 (a) The representative topographic images of NWs used for recording the PL spectra by means of an atomic force microscopic (AFM) tip of 20 nm assisted with a long working distance NUV objective of 15× (N.A. = 0.4) in the scanning probe microscopy (SPM, MV4000; Nanonics, Israel) coupled to Raman spectrometer (inVia; Renishaw, UK). (b) The statistical dependence of PL intensity in the 2D semiconductor micro– and nano– sized interaction area with respect to the separation of consecutive NWs. Inset shows the PL spectra corresponding to different separations.

A collection of mono–dispersed AlGaN NWs with near uniform size distribution (Fig. 6.1), and in close proximity to each other, may lead to the existence of reasonably long lived photons (owing to multiple interactions) in the intervening space between the NWs. These photons originate from an external laser source (reflected), as well as from electronic transitions within the materials, and exist in between the intervening space of NWs so long as the external pump laser is on. A non–zero non–equilibrium population density of such long lived photons increases the stimulated emission by utilizing electrons in excited states. The elevation in photon density in the intervening space may be the reason for enhanced PL due to proximity of other NWs. In order to understand the phenomenon quantitatively, let us assume that the external pump laser promotes electrons to an upper level (U) from the ground state (G), where N_U and N_G be the number of electrons in the excited and ground states (N_G+N_U =

N, being a conserved quantity). One can write down a rate equation for spontaneous emission/absorption of photons,[17] $dN_U/dt = -dN_G/dt$,

$$\frac{dN_U}{dt} = -\frac{N_U}{\tau_{sp}} - W_P(N_U - N_G) + R_P \qquad \text{…..…………………(6.1)}$$

where τ_{sp} is the time for spontaneous electronic transition from U to G state, with emission of a photon. R_P is the rate at which electrons are pumped to U by absorption of photons. The intermediate term is necessary when the electronic transitions are also induced by external photons, *i.e.*, stimulated emission/absorption processes. W_P is the rate of stimulated emission/absorption per electron.[17] Suppose, σ is the cross sectional area for stimulated emission from a single electron at U due to the interaction with one external photon, and N_L be the total number of local long lived photons, confined in an available interaction volume V. If the photon group velocity in the medium is v_g, then the total number of stimulated emission/absorption events per second from one electron is $\sigma \cdot v_g \times N_L/V = W_P$ (having dimension inverse of time). When the system is in dynamic equilibrium, putting $\frac{dN_U}{dt} = 0$ one gets,

$$N_U = \frac{R_P + \frac{(\sigma . v_g) N N_L}{V}}{\frac{2(\sigma . v_g) N_L}{V} + \frac{1}{\tau_{sp}}} \qquad \text{………..……………(6.2)}$$

If there are no local photons (no stimulated emission or absorption of photons), *i.e.*, $N_L = 0$, the time averaged $N_U = R_P\, \tau_{sp}$. On the other hand, in large N_L limit, N_U approaches the value $N/2$, which is the maximum thermodynamically achievable population of U. Similarly, we can write down a rate equation for the number of photons responsible for stimulated emission/absorption process,

$$\frac{dN_L}{dt} = -\frac{N_L}{\tau_{ph}} + \frac{N_U}{\tau_{sp}} + \frac{(\sigma.v_g)}{V}(N_U - N_G) \qquad \text{.....………………(6.3)}$$

where, τ_{ph} is the decay time for these photons due to processes other than the stimulated emission/absorption. In order to get the steady state value of N_L, we set $dN_L/dt=0$. For $N_G = N-N_U$, and expressing N_U in terms of N_L from the equation (6.2), we find $N_L = R_P\,\tau_{ph}$ and

$$N_U = R_P\tau_{sp}\,\frac{1+\dfrac{2(\sigma.v_g)N\tau_{ph}}{V}}{1+\dfrac{(\sigma.v_g)\tau_{ph}.R_P\tau_{sp}}{V}} \qquad \text{……………..(6.4)}$$

The PL intensity, I_{PL} is the total number of photons per second emanating from all possible transitions of electrons from *U* to *G*. The number of such transitions per second is proportional to N_U, that is, $I_{PL} = (h\upsilon)|M|^2N_U$, where $h\upsilon$ is the energy difference between *U* and *G*, and *M* being a matrix element for this transition. The ratio of the second term in denominator and numerator in equation (6.4), is $R_P\tau_{sp}/N = N_U(N_L=0)/N <<1$. In fact, this ratio approaches 1/2 only when N_L approaches infinity. Neglecting the second term in the denominator, we get,

$$I_{PL} \propto R_P\tau_{sp}(1+2\sigma v_g N\tau_{ph}/V) \qquad \text{…………………………..…..(6.5)}$$

The second term in the equation (6.5) is responsible for the increase in PL intensity due to the presence of the intervening long lived photons in between the NWs. Thus, the increase in the PL intensity is proportional to lifetime of these photons τ_{ph}, the stimulated emission cross section σ, and is inversely proportional to the available interaction volume (*V*) occupied by these photons.[17] Since, $V = h\times l\times d$ where, *h*, *l* and *d* are the height, length and separation between the NWs; so for a fixed *h* (~100) nm, the diameter of the NWs less than the excitation wavelength (λ)), the increase in PL intensity is inversely proportional to the interaction area ($l \times d$).

6.2.2 Polarized PL imaging of single NW in the sub–diffraction regime

The PL imaging of single AlGaN NW with an average diameter 100 (±10) nm is carried out over an area of 3 × 1 μm^2 using an excitation laser of wavelength of 325 nm. The figure 6.5a shows the PL maps of single NW generated by integrating the intensity of FE emission for π–polarization. The PL maps for σ–polarization with the variation of intensity along the NW for FE emission is also studied as shown in the figure 6.5b. The optical image of a single NW used for both π– and σ– polarized PL maps is also shown (inset Fig. 6.5b) with a schematic grid pattern used for the mapping. The scale bar of 3 μm represents the true dimension along the long axis of the NW only. The variation of intensity in the PL maps observed for different polarization configuration is due to difference in the interaction of electric field strength with NW. In π–polarization, the excitation electric field, which is parallel to the NW long axis strongly interacts with the NW (Fig. 6.5a). In this configuration, the internal electric field $E_{i\pi}$ in the NW medium remains same as the external electric field $E_{e\pi}$ (*i.e.*, $E_{i\pi} \sim E_{e\pi}$). Whereas, in case of σ–polarization, the internal electric field $E_{i\sigma}$ will attenuate according to the relation $E_{i\sigma} = [2\varepsilon_0 / (\varepsilon + \varepsilon_0)]E_{e\sigma}$, where $E_{e\sigma}$ is the external electric field perpendicular to the long axis, ε is the dielectric constant of the cylindrical NW (~5.8 for GaN) and $\varepsilon_0 = 1$ in air or vacuum.[10-16] Along with the cylindrical geometry of the NW, the large dielectric contrast between the NW and the surrounding medium strongly favours absorption and emission of light for π–polarization compared to those for σ–polarization.[10-16] The intensity distributions in the PL maps for FE emissions with different polarizations (Figs. 6.5a and 6.5b) are observed to be good agreement with the above relation.

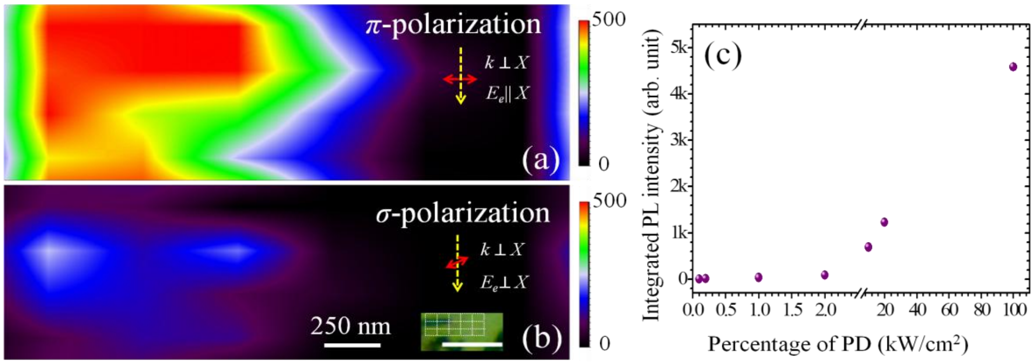

Figure 6.5 The (a) π– and (b) σ– polarized PL maps for a single AlGaN NW. The optical image of a typical single NW with a schematic grid pattern used for PL imaging is shown in the inset. The scale bar corresponds to a length of 3 μm. (c) The integrated peak intensity Vs excitation laser power density (PD) from a single NW with an inter–NW separation of ~ 2 μm with a maximum laser PD of 63 kW/ cm^2.

The elevation in the emission properties of an emitter can also be understood in terms of antenna effects.[17,18] However, in the present study, the confinement of light due to the antenna effect in the nanostructure configurations (insets of Fig. 6.3) is minimum because of the dipole interactions corresponding to the measured NW (middle), which is parallel to the adjacent NWs can be negligible. Thus, we emphasize photonic confinement of light as a cause for the enhancement of PL emission intensity ($I_{PL,}$ Eqn. (6.5)) confined in the interaction area between the adjacent parallel NWs. In this context, the excitation laser (pump) power dependence of emission from a single NW with inter–NW separation, d ~2 μm is also investigated. The integrated emission peak intensity *vs*. excitation laser power density (PD) (Fig. 6.5c) shows a non–linear behavior, which is a confirmation for the possible presence of stimulated emission process.[19-21]

In the Abbe's diffraction limit (λ/2N.A.),[1] the far–field spectroscopic imaging or focusing is not possible for nanostructures having dimension <325 nm while using 325 nm excitation wavelength and an objective lens with N.A. value of 0.50. Considering negligible interface area of the catalyst Au NP, as compared to that for the total surface area of the NW (Fig. 6.1), possibility of plasmonic interaction between the Au NPs and AlGaN NWs with a 325 nm excitation source can also be ruled out. However, the optical confinement effect for the light–matter interactions allow one to record the PL maps of single AlGaN NW in the sub–wavelength scale even in the absence of any plasmonic effect. The dimension of PL maps of single NW (~200 nm) using *π*–polarization is found to be enlarged as compared to the FESEM images of a single AlGaN NW (~100 nm; outset Fig. 6.1b). The spread is essentially due to the focusing limit (~0.8 μm) of the incident beam which is higher than the spatial resolution (~100 nm) of the motorized sample stage used for the PL mapping.

6.3 Vibrational studies of single NW in the sub–diffraction regime

6.3.1 Resonance Raman spectroscopy in the optically confined NWs

Utilizing the optical confinement of a single NW in the proximity of surrounding NWs with a dielectric contrast,[8] polarization dependent RRS experiments were performed for a single AlGaN NW for investigating the crystalline orientation. Since the Raman spectrum (Fig. 6.6a), obtained from a single NW by using 514.5 nm excitation showed very poor intensity, we performed RRS study using the 325 nm (3.815 eV) excitation above the RT band gap of wurtzite AlGaN (~3.55 eV)[9] to maximize the Raman signal for a single NW in the sub–diffraction limit by invoking Fröhlich interaction of electron–phonon coupling.[22] In RRS, we excited the NWs with a laser source having energy greater than the band gap of the material. So, it led to the interaction of conduction electron and longitudinal optical (LO) phonon of ionic crystals and hence an improvement of Raman intensities could be noticed.

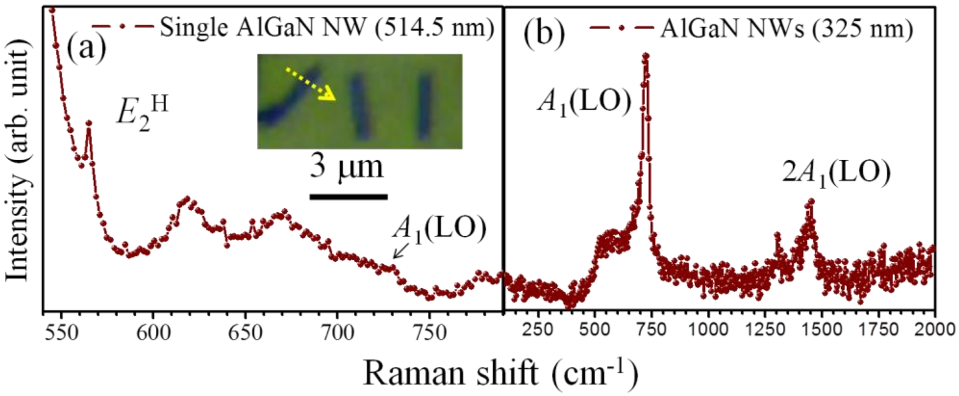

Figure 6.6 (a) The Raman spectrum for a single AlGaN NW with an excitation wavelength of 514.5 nm showing weak intensities of modes corresponding to the wurtzite phase. Inset shows the optical image of NW used for recording the Raman spectrum (indicated by an arrow) (b) RRS observed for an ensemble of AlGaN NWs using the 325 nm excitation wavelength with first and second order A_1(LO) modes

From the RRS studies of ensemble AlGaN (Fig. 6.6b), the electron–phonon coupling strength is estimated to be ~0.6 from the intensity ratio of $2A_1$(LO)/A_1(LO).

6.3.2 Polarized Raman spectrum of single NW: Growth direction

The polarized RRS of single NW shows only one peak (Fig. 6.7a) centered around 725 cm^{-1} which is assigned to A_1(LO) mode of the AlGaN.[9] The peak observed at 521 cm^{-1} is because of the optical vibrational mode of the Si(100) substrate.[23] The sample is chosen for the polarized micro–Raman spectra in such a way that single crystalline AlGaN NW is horizontally lying on the Si(100) substrate itself. The axis along the cylindrical NW is chosen as X direction, where as the incident and the scattered light propagation direction is considered along the Z direction. The parallel $Z(XX)\bar{Z}$ and perpendicular $Z(XY)\bar{Z}$ polarization was configured using a half wave plate and a polarizer (Fig. 6.2). According to the polarization selection rule in the backscattering configuration for a wurtzite [0001] GaN, (i.e., Z||[0001]), only the E_2^H phonon mode with E_2 symmetry should be observable in the $Z(XY)\bar{Z}$

while both E_2^H and A_1(LO) phonon modes should be viewed in the $Z(XX)\bar{Z}$ configuration as in the previous studies (Table 4.1). However, it is well known that E_2^H mode will not be active in the RRS. The E_2^H mode, incidentally was observed for the 514.5 nm excitation wavelength (Fig. 6.6a). However, we preferred polarized RRS studies in these nanostructure as the A_1(LO) mode alone as it was useful in identifying the crystallographic information of wurtzite phase in the backscattering configuration. The A_1(LO) mode around 725 cm^{-1}, was observed in the $Z(XX)\bar{Z}$ configuration and the same mode was absent in the case of the $Z(XY)\bar{Z}$ configuration. Incidentally, the optical mode of Si was also found to disappear in the $Z(XY)\bar{Z}$ configuration in the cubic symmetry.[23] Hence, the presence of A_1(LO) mode in the $Z(XX)\bar{Z}$ configuration and the absence of it in the $Z(XY)\bar{Z}$ configuration clearly indicates that the horizontally lying NWs on the Si(100) substrate may have the crystallographic growth orientations normal to the non–polar *m*–plane [1-100] (schematic, Fig. 6.7b). For further confirmation, a typical single NW (Fig. 6.7c) involved in the parallel arrangement of NWs used for recording a HRTEM as shown in the figure 6.7d. It shows an inter–planar spacing of 2.98 Å corresponding to (1-100) *m*–planes of AlGaN. The SAED pattern of the single NW (Fig. 6.7d) is indexed to wurtzite phase of single crystal AlGaN with zone axes along [0001]. Therefore, the growth direction of the AlGaN NW is along the *m*–planes of the wurtzite structure. The structural analysis is exactly matching with the information inferred from the polarized RRS study (Figs. 6.7a and 6.7b). Thus, the polarized Raman spectroscopy is an accurate tool for understanding the crystallographic orientations even at the nanometer scale. It was ensured that the individual NWs are well separated (~3 μm as shown in inset Fig. 6.7a) as compared to the excitation laser spot size ~0.8 μm to provide a Raman spectrum corresponding to a single NW.

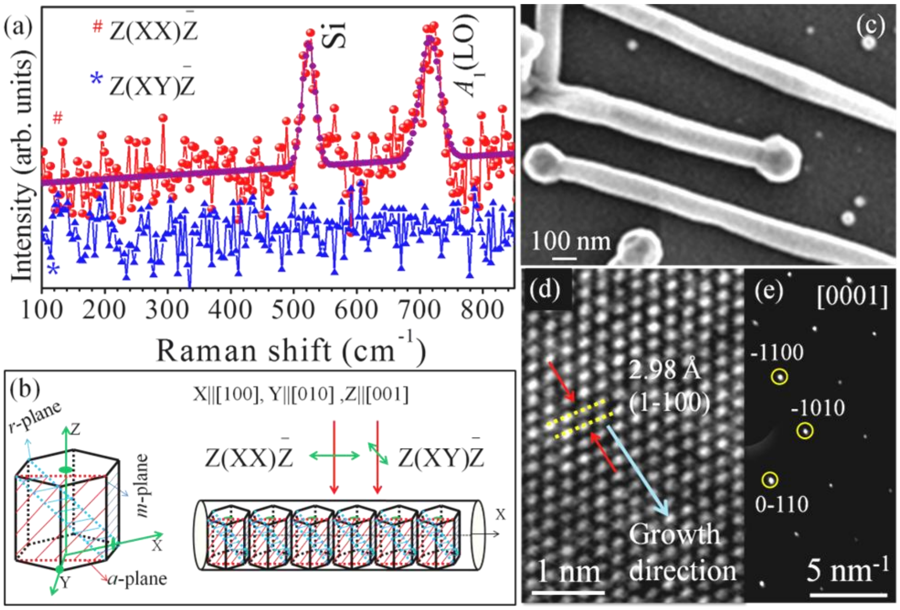

Figure 6.7 (a) Polarized Raman spectra for single NW with an excitation wavelength 325 nm for different polarization configurations. (b) The schematic depiction for a single NW with two different polarization configurations and the possible stacking arrangement of wurtzite unit cells in the cylindrically shaped NW (c) Typical FESEM images of NWs with a mutual parallel arrangement (d) HRTEM image of a single AlGaN NW shows growth direction along *m*–plane [1-100] (e) The SAED pattern is indexed to wurtzite phase of AlGaN with zone axis along [0001].

In the present study, the confinement of polarized light is because of the trapped photons in between semiconductor NW–air–semiconductor NW configuration as shown schematically (Fig. 6.2). Optical confinement of polarized light was reported in the 1D semiconductor–dielectric and metal–dielectric interfaces.[8,24-27] Since, there is a variation of refractive index in AlGaN NW–air–AlGaN NW interface, the excitation photons is confined in between the NWs giving rise to long lived photon in enhancing its intensity.[8,24-27] The optically trapped photons in between the consecutive NWs interact with the material and yields the enhanced Raman spectra.[8,28-30] Use of RRS with strong electron–phonon coupling along with optical confinement of polarized light are also exploited to understand the crystallographic orientations for the sub–diffraction limit of ~100 nm NW using a wavelength of 325 nm. The optical confinement of polarized light in the nanostructures of diameter ~100 nm, which is well above the quantum confinement size of 11 nm for GaN,[21] is envisaged for the polarization measurements in the dielectric contrast of ~ 5.6 for AlGaN with respect to that of 1 for the surrounding medium of air.[8,10-16,28]

6.4 Near–field interactions of visible light with sub–diffraction limited nanostructures

6.4.1 Semiconductor AlGaN NW

The resultant near–field light–matter interaction (Fig. 6.8) is shown for AlGaN single NW along with Au NPs of various sizes recorded using the NSOM technique (Fig. 2.13, Chapter 2). The high resolution topographic AFM images of the single NW in the 2D and 3D (Figs. 6.8a and 6.8b) show smooth and cylindrical shape, as observed in the FESEM images, with a diameter of ~120 nm.

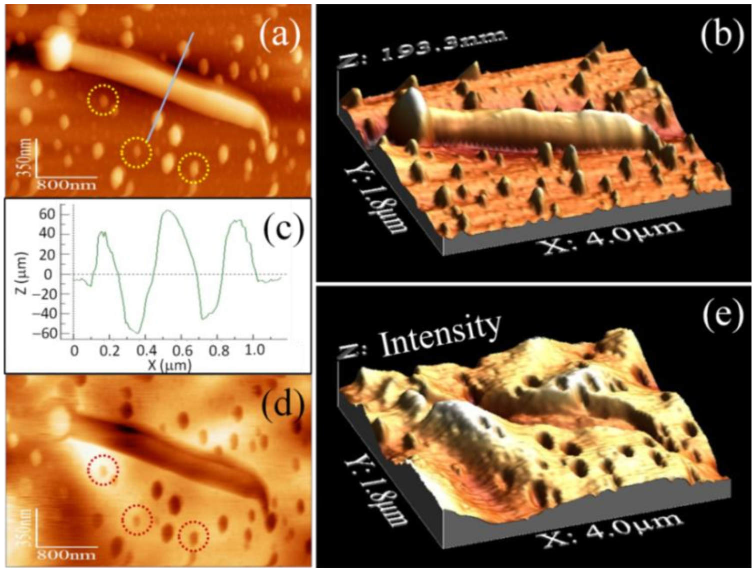

Figure 6.8 The topographic (a) 2D and (b) 3D AFM images of a single AlGaN NW along with Au NPs, (c) The height variation of AFM cantilever along the line across Au NP–AlGaN NW–Au NP as shown in (a) and the corresponding optical NSOM images of a single AlGaN NW along with Au NPs are shown in (d) 2D and (e) 3D. The Au NPs with size of the order ~20 nm is encircled in the AFM topography and in the optically resolved NSOM images.

The height variations of AFM cantilever along the line across Au NP–AlGaN NW–Au NP show (Fig. 6.8c) the height of AlGaN NW and Au NP as 120 and 40 nm, respectively. Moreover, we also observed Au NPs with a size smaller than 40 nm in the same image and it was very clearly resolved by the NSOM technique with an aperture probe diameter of 150 nm. The Au NPs with sizes ~20 nm are encircled in the AFM topography (Fig. 6.8a) and in the optically resolved NSOM images (Fig. 6.8d). The NSOM images of AlGaN single NW as well as catalyst Au NPs in 2D and 3D are also shown (Figs. 6.8d and 6.8e). The NSOM images for a few and an ensemble of AlGaN NWs show similar results as observed for the single NW.[31] Results with high repeatability, observed for the similar NSOM experiments,[31] ensure that the reduction of intensity in the NSOM images is due to the prominent absorption of light and it is not because of any topography related artefacts. Moreover, the observed AFM images maintain the same cylindrical shape as well as smooth morphology as observed in FESEM images (Fig. 6.8) which confirms that the NSOM images are also not affected by any type of artefacts or feedback problems while performing the measurements. Since the diameter of AlGaN NW (~120 nm) is far below the diffraction limit for the excitation wavelength (532 nm), one need to shorten the wavelength down to the sub–diffraction regime for obtaining highly resolved optical images. Using metallic coated NSOM probe, it is possible to produce an evanescent wave with momentum higher than that of the original excitation wavelength $\lambda_0=2\pi/k_0(\omega)$ with wave vector of $k_0(\omega)=\omega/c$, where c is the velocity of light. Therefore, the evanescent waves emanating from the NSOM probe aperture possess a group of wave vectors higher than the original excitation laser as $k_{ev}(\omega)=\omega/v$, with different velocities (v) slower than the excitation wave velocity ($v < c$).[1-7] Therefore, the NSOM measurements are advantageous to provide super–resolution. With this advantage, in the present study, we have achieved an optical special resolution up to the order of ~20 nm with the 150 nm apertured probe as mentioned earlier. At the same time, it preserves the excitation frequency and energy.[1-7] Thus, the NSOM offers the possibility of optical as well as spectroscopic imaging in the sub–diffraction regime. Therefore, from the scanned images using NSOM technique, we can understand even the intrinsic properties of a sample as revealed by its electronic or vibrational energies.[1] By taking this advantage, we used the NSOM technique to understand the interaction of green laser (532 nm = 2.33 eV) with single semiconductor AlGaN NW in the near–field regime. The reported RT band gap of AlGaN NWs is ~3.53 eV,[9] which is higher than the excitation energy of 2.33 eV. Therefore, a complete transmission of light through the AlGaN NW is expected. However, surprisingly we observed a prominent absorption of light along the AlGaN NW, as shown in the NSOM images in 2D and 3D (Figs. 6.8d and 6.8e).

For better understanding of the light–matter interaction of AlGaN NW, we recorded PL spectrum (Fig. 6.9a) in the energy range of 1.7 to 3.8 eV from an ensemble and single NW using an UV excitation of 325 nm (~3.815 eV). Distinct PL peaks, centered at 3.53, 3.30, 2.05, and 1.76 eV, are observed (Fig. 6.9a). The PL spectrum, recorded for an ensemble as well as single NW using an available visible excitation of 514.5 nm (~2.41 eV) which is close to the excitation used in NSOM measurement, also shows the similar low energy emission peaks centered at ~2.08, and ~1.77 eV (Fig. 6.9b). The PL emission at ~3.53 eV and ~3.30 eV is assigned as FE and DAP emissions, respectively, as discussed earlier.[9] The presence of unintentional O dopant in the AlGaN NW may be responsible for the emission at ~2.05–2.08 eV (Fig. 6.9), which may be observed because of the recombination of electrons from the shallow donor state of V_N to the holes in the deep acceptor state of O_N–V_{Ga} complex.[32]

Similarly, the presence of unavoidable impurity of C in the sample produces the C_N–V_{Ga} complex, which also may act as a deep acceptor leading to the PL emission peak centered at ~1.76–1.77 eV (Fig. 6.9) for recombination of electrons from the shallow donor state of V_N.[33,34]

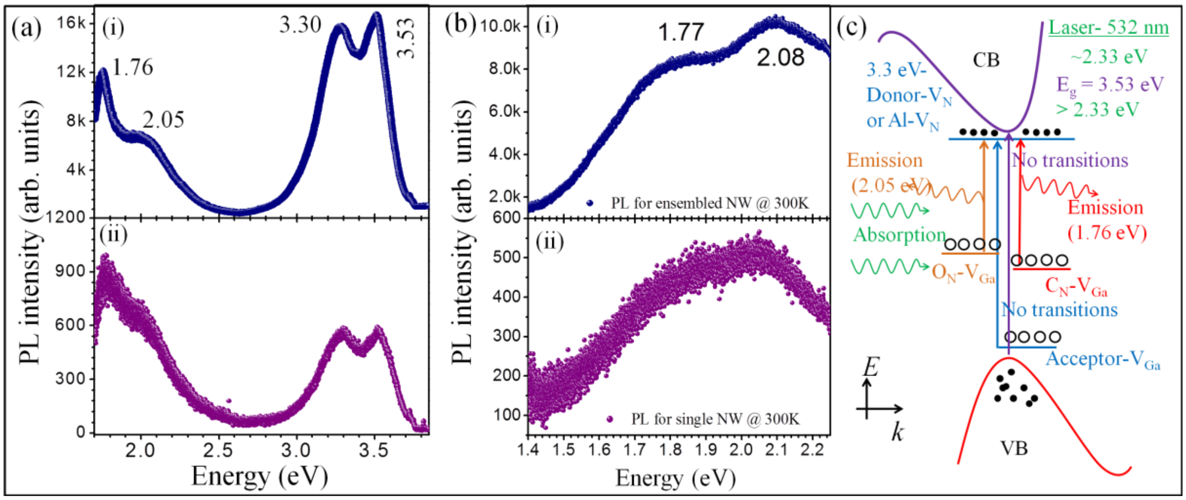

Figure 6.9 The room temperature PL spectra with an excitation of (a) 325 nm (3.815 eV) and (b) 514.5 nm (2.41 eV) for (i) an ensemble and (ii) a single AlGaN NW, respectively. (c) The schematic band diagram of AlGaN NW showing possible light–matter interactions and electronic transitions for a ~2.33 eV excitation.

The interaction of single AlGaN NW with light in the near–field regime is realized by using the help of possible energy levels in the schematic representation of band–diagram (Fig. 6.9c). Even though, we are using the evanescent wave to image the NW, the energy of the electromagnetic (*em*) field is preserved as 2.33 eV. Therefore, it does not invoke any electronic transition for DAP and FE emission at ~3.30 and ~3.53 eV, respectively, which are well above 2.33 eV. However, the excitation energy of 2.33 eV is sufficient to activate the transitions at ~2.05 and ~1.76 eV. The emissions at ~1.76 and ~2.05 eV are blocked by the band pass filter used before the detector in the NSOM experimental setup (Fig. 2.13, Chapter 2). Therefore, the probing light energy is utilized for exciting the defect levels and hence we observe a significant absorption along the single NW in the NSOM images (Figs. 6.8d and 6.8e).

6.4.2 Metallic Au nanoparticles

In the NSOM images of the AlGaN samples, we also observed strong SPR related absorption for Au NPs. Therefore, we also studied the near–field interaction of metallic Au NP with the same visible laser light of energy 2.33 eV (Fig. 6.10). The high resolution topographic 2D and 3D AFM images of the Au NP (Figs. 6.10a and 6.10b) shows smooth and spherical shape of the NP with a diameter of ~100 nm. The resultant NSOM images of catalyst Au NP in 2D and 3D are shown in figures 6.10c and 6.10d. Like semiconductor AlGaN NW, the NSOM image of Au NP (Figs. 6.10c and 6.10d) also shows strong absorption of *em* waves, but the mechanism behind the light–matter interaction is entirely different from the earlier case. A significant absorption of light with wavelength 532 nm by Au NP is observed because of the fact that the SPR peak value ~540 nm for Au NPs matches the excitation wavelength.[35-37] The NSOM measurement is also performed for an ensemble of Au NPs showing similar strong SPR absorption.[31]

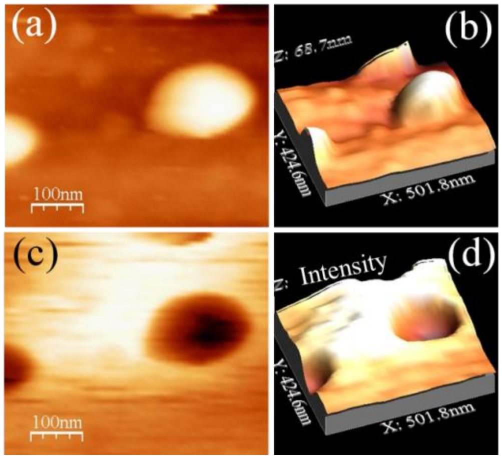

Figure 6.10 AFM topography (a) 2D and (b) 3D and the corresponding optical NSOM images (c) 2D and (d) 3D of a typical Au NP.

At resonance, the incident *em* waves coupled with collective oscillation electrons can produce surface plasmon polariton (SPP), which is perpendicular to the surface of Au NP. The frequency dependent wave vector of SPP can be expressed as in terms of frequency dependent dielectric constants of metal ($\varepsilon_m = \varepsilon_m' + i\varepsilon_m''$) and surrounding medium ($\varepsilon_d = 1$, for air or vacuum), $k_{spp}(\omega) = \frac{\omega}{c}\sqrt{\frac{\varepsilon_d . \varepsilon_m}{\varepsilon_d + \varepsilon_m}}$. Therefore, the effective wavelength of the SPP is $\lambda_{spp} = 2\pi/k_{spp}$.[7,38-40] The SPPs, with a specific wavelength smaller than the excitation, can propagate through the surface of Au NPs up to a propagation length, which depends on the complex dielectric constants of the metal and dielectric medium.[6,38-40] Once the SPP propagates through the surface of Au NP and crosses the metallic region, then the *em* wave may decouple from the SPP and it can be converted to a propagating wave. The intensity of the absorption is influenced by the frequency dependent poalrizability of the Au NPs and it can be vary with respect to the size of the Au NPs.[5,38-40] Thus, because of the variation of different sizes of the Au NPs, it is possible to observe them with relatively different absorption intensities (Figs. 6.8d and 6.8e). Apart from the formation of SPP, some portion of the absorbed excitation laser may also participate in the lattice phonon generations leading to heating as well as inter–band transitions of Au NPs.[35,41]

6.5 Summary

In conclusion, we have recorded the far–field spectroscopic image using polarized PL spectra for a cylindrically shaped single AlGaN NW with a diameter 100 (±10) nm in the sub–wavelength scale. The PL intensity from a single NW is found to be sensitive to the proximity of other NWs and is found to be increased by an order of magnitude as the separation between NWs varies from 10 to 2 μm. The proximity induced enhancement of PL intensity can be understood by assuming the existence of reasonably long lived photons in the intervening space between the NWs. A non–zero non–equilibrium population of such photons may cause additional stimulated emission, leading to the enhanced PL emission with the intensity proportional to $1/(l \times d)$. Thus, the report is encouraging for analysing and processing nanoscopic objects in the sub–wavelength limit with the far–field configuration using the diffraction limited optics. The proposed alternative methodology avoids the complex material processing for achieving optimized noble metal thickness involved in the plasmonic technique. Polarized resonance Raman spectroscopy (RRS) studies of a single AlGaN NW of diameter ~100 nm with optical confinement in the dielectric contrast of surrounding NWs is used to understand its crystalline orientation. The crystallographic orientations predicted by the optically confined RRS studies shows a good agreement with the structural analysis. As a matter of fact, optical confinement effect due to the dielectric contrast of NW with respect to that of surrounding media along with strong electron–phonon coupling of resonance Raman spectroscopy is useful for the spectroscopic analysis in the sub–diffraction limit of ~100 nm using a wavelength of 325 nm.

We envisage the use of the NSOM technique for direct understanding of light–matter interaction of semiconductor as well as metallic nanostructures of sub–diffraction limited dimension in the near–field regime. As a major accomplishment, we achieved an optical spatial resolution up to ~20 nm even with a 150 nm apertured NSOM probe. The isolated single and semiconductor AlGaN NW with a diameter ~120 nm grown *via* VLS mechanism was observable because of the significant absorption of visible light owing to the electronic transitions originated from the native defect related energy levels, as supported by PL studies. The NSOM images of metallic Au NP catalyst with diameter ~100 nm shows a strong surface plasmon resonance related absorption of excitation laser with an energy of 2.33 eV (λ = 532 nm) due to the formation of surface plasmon resonance on the surface of the Au NPs.

6.6 References

[1] S. Kawata, Y. Inouye and P. Verma, *Nature Photonics*, **2009**, 3, 388

[2] A. Polman, *Science* **2008**, 322, 868

[3] E. Ozbay, *Science* **2006**, 311, 189

[4] M. Achermann, *J. Phys. Chem. Lett.* **2010**, 1, 2837

[5] N. Rotenberg and L. Kuipers, *Nature Photonics* **2014**, 8, 919

[6] W. L. Barnes, A. Dereux and T. W. Ebbesen *Nature* **2003**, 424, 824

[7] C. Genet and T. Ebbesen, *Nature* **2007**, 445, 39

[8] A. K. Sivadasan M. Sardar and S.Dhara, *Ann. Phys. (Berlin)* , **2016**, DOI:10.1002/andp.201600165

[9] A. K. Sivadasan, A. Patsha, S. Polaki, S. Amirthapandian, S. Dhara, A. Bhattacharya, B. K. Panigrahi, A. K. Tyagi, *Cryst. Growth Des.* **2015**, 15, 1311

[10] J. Wang, M. S. Gudiksen, X. Duan, Y. Cui, C. M. Lieber, *Science* **2001**, 293, 1455

[11] H.Y. Chen, Y.C. Yang, H.W. Lin, S.C. Chang, S. Gwo, *Opt. Express* **2008**, 16,13465

[12] J. B. Schlager, N. A. Sanford, K. A. Bertness, J. M. Barker, A. Roshko, P. T. Blanchard, *Appl. Phys. Lett.* **2006**, 88, 213106

[13] H. E. Ruda, A. Shik, *Phys. Rev. B* **2005**, 72, 115308

[14] H. E. Ruda, A. Shik, *J. Appl. Phys.* **2006**, 100, 024314

[15] P. P. Paskov, T. Paskova, P.O. Holtz, B. Monemar, *Phys. Rev. B* **2004**, 70, 035210

[16] J. B. Schlager, N. A. Sanford, K. A. Bertness, J. M. Barker, A. Roshko, P. T. Blanchard, *Appl. Phys. Lett.* **2006**, 88, 213106

[17] C. Gies, J. Wiersig, and F. Jahnke, *Quantum Statistical Properties of the Light Emission from Quantum Dots in Microcavities; invited book chapter in Advances in Single Semiconductor Quantum Dots,* **2009**, Peter Michler Ed., Springer, ISBN 978–3–540–87445–4

[18] A. E. Krasnok A. P. Slobozhanyuk, C. R. Simovski, S. A. Tretyakov, A. N. Poddubny, A. E. Miroshnichenko, Y. S. Kivshar and P. A. Belov, *Sci. Rep.* **2015**, 5, 129956: DOI: 10.1038/srep12956

[19] M. S. Eggleston, K. Messer, L. Zhang, E. Yablonovitch and M. C. Wu, *Proc. Natl. Acad. Sci. U.S.A.* **2015**, 112, 1704

[20] X. Duan, Y. Huang, R. Agarwal and C. M. Lieber, *Nature* **2013**, 421, 241

[21] J. C. Johnson, H. J. Choi, K. P. Knutseni, R. D. Schaller, P. Yang and R. J. Saykally, *Nat. Mater.* **2002**, 1, 106

[22] S. Dhara, S. Chandra, G. Mangamma, S. Kalavathi, P. Shankar, K. G. M. Nair, A. K. Tyagi, C. W. Hsu, C. C. Kuo, L. C. Chen, K. H. Chen, and K. K. Sriram, *Appl. Phys. Lett.* **2007**, **90**, 213104

[23] P. A. Temple, and C. Hathaway, *Phys. Rev. B* **1973**,**7**, 3685

[24] H. Cao, Y. G. Zhao, S. T. Ho, E. W. Seelig, Q. H. Wang, and R. P. H. Chang., *Phys. Rev. Lett.* **1999**, 82, 2278

[25] Y. Bian, and Q. Gong, *Nanotechnology* **2014**, 25, 345201

[26] B. Wood, J. Pendry, and D. Tsai, *Phys. Rev. B* **2006**, 74, 115116

[27] O. Painter, J. Vučkovič, A Scherer, *J. Opt. Soc. Am. B.* **1999**,16, 275

[28] L. Cao, J. S. White, J. S. Park, J. A. Schuller, B. M. Clemens, and M. L. Brongersma, *Nat. Mater.* **2009**, 8, 643

[29] T. Tanabe, M. Notomi, E. Kuramochi, A. Shinya, and H. Taniyama, *Nature Photonics* **2007**, 1, 49

[30] P. J. Pauzauskie, and P. Yang, *Materials Today* **2006**, 9, 36

[31] A. K. Sivadasan, K. K. Madapu, S. Dhara, *Phys. Chem. Chem. Phys.* **2016**, 18, 23680

[32] A. Patsha, S. Amirthapandian, R. Pandian, and S. Dhara, *J. Mater. Chem. C* **2013**, 1, 8086

[33] D. Zhou, Y. Ni, Z. He, F. Yang, Y. Yao, Z. Shen, J. Zhong, G. Zhou, Y. Zheng and L. He, *Phys. Status Solidi C*, **2016**, 13, 345

[34] C. Seager, A. Wright, J. Yu and W. Götz, *J. Appl. Phys.* **2002**, 92, 6553

[35] M. Li, S. K. Cushing and N. Wu, *Analyst* **2015**, 140, 386

[36] V. Myroshnychenko, J. Rodríguez–Fernández, I. Pastoriza-Santos, A. M. Funston, C. Novo, P. Mulvaney, L. M. Liz–Marzán and F. J. G. de Abajo, *Chem. Soc. Rev.* **2008**, 37, 1792

[37] S. A. Maier and H. A. Atwater, *J. Appl. Phys.* **2005**, 98, 011101

[38] J. Weiner, *Rep. Prog. Phys.* **2009**, 72, 064401

[39] J. Zhang, L. Zhang, and W. Xu, *J. Phys. D: Appl. Phys*. **2012**, 45, 113001

[40] W. A. Murray and W. L. Barnes, *Adv. Mater.* **2007**, 19, 3771

[41] M. R. Beversluis, A. Bouhelier and L. Novotny, *Phys. Rev. B.* **2003**, 68, 115433

CHAPTER 7

BRIEF SUMMARY OF THESIS AND SCOPE FOR FUTURE WORK

"*Let us not seek the Republican answer or the Democratic answer, but the right answer. Let us not seek to fix the blame for the past. Let us accept our own responsibility for the future*" ...John F. Kennedy

7.1 Summary of thesis

As the title suggests, the present thesis mainly reports the "Optical Properties of AlGaN Nanostructures." A brief, summary of the thesis is outlined as follows,

1. Growth of AlGaN nanostructures by atmospheric pressure chemical vapor deposition (APCVD) technique *via* catalyst assisted vapor–liquid–solid (VLS) mechanism as well as the self catalytic vapor–solid (VS) mechanism.
2. Tuning of the surface morphology for AlGaN nanostructures was achieved by means of changing the growth parameters, namely, catalysts size and its distribution, onset temperature of NH_3 and its flow rate. The present study includes the successful synthesize of cylindrical as well as well–faceted triangular and hexagonal shaped nanostructures.
3. The crystallographic studies ensure that the cylindrical and triangular nanowires (NWs) grown along the non–polar *m*–plane (1-100), whereas, the hexagonal shaped sub–microrods are grown along the polar *c*–plane (0001).
4. The high intense photoluminescence (PL) spectra observed for the as prepared sample at room temperature, even with low excitation power ensures the premier optical quality of the material. The observed blue shift of PL emission for the AlGaN nanostructures compared to that of GaN confirms the presence of Al in the sample.

The atomic percentage of Al is found to be 2.0–3.0% using the band bowing formalism of the random alloy formation.

5. The crystallographic orientation dependent polarized Raman studies and Raman imaging for the allowed phonon modes of AlGaN crystallites show the single crystalline nature of the hexagonal sub–mocrorods.
6. The polarization dependent PL studies show the variation of the emission intensities for *m*–plane and *c*–plane oriented AlGaN crystallites by the influence of the native defect states and intrinsic electric fields present in the crystallites.
7. The presence of intrinsic electric field is confirmed by the piezo–response force microscopic (PFM) studies of the AlGaN crystallites. The contrast variation in the PFM image is due to the variation of surface charge density over the surface of AlGaN microrods originating due to the crystalline orientation with respect to its AlN base layer. The effective piezo electric coefficient for AlGaN microrod along the *c*–axis (d_{33}) is found as ~4.14 pm/V.
8. The presence of surface optical (SO) phonon modes are identified in the Raman spectra of the 1D array of $Al_{0.97}Ga_{0.03}N$ nanorods (NRs) in the presence of air and CCl_4 as the surrounding media. The observed red shift in the $q \neq 0$ mode frequencies of around 17–18 cm^{-1} in the Raman spectra for $Al_{0.97}Ga_{0.03}N$ NRs in the presence of CCl_4 with different dielectric constants of the surrounding medium compared to that for air, confirms the presence of SO mode in the observed Raman modes

The Fourier component of the surface potential for a periodicity of ~200 nm required for the breakdown of its translational symmetry is identified by the theoretical simulation of dispersion curve for the SO modes and matched with the experimental data probed by the Raman spectra.

9. The interface optical (IO) phonon modes are observed in the Raman spectra of $[GaN(\sim1.25 \text{ nm})/AlN (\sim2.0 \text{ nm})]_{20}$ and $[Al_{0.35}Ga_{0.65}N(\sim1.75 \text{ nm})/Al_{0.55}Ga_{0.45}N(\sim2.0 \text{ nm})]_{20}$ multi–quantum well (MQW) structures. The red shift of IO mode (~4 cm^{-1}) of $[GaN/AlN]_{20}$ compared to that for $[Al_{0.35}Ga_{0.65}N/Al_{0.55}Ga_{0.45}N]_{20}$ MQW structure with the change in dielectric constant of the surrounding medium confirms the existence of IO modes in the observed Raman Spectra.

   The observation of the IO phonon modes is attributed to the relaxation of Raman selection rules because of the breakdown of translational symmetry of the surface potential due the presence of the periodic interfaces and surface modulations of superlattice (SL) structure of MQWs

10. The proximity induced enhancement of PL intensity is observed in the case of the mono–dispersed AlGaN NW sample. A non–zero non–equilibrium population of localized photons may cause additional stimulated emission, leading to the enhanced PL emission. The confined light in the dielectric contrast is used for spectroscopic PL imaging of a single NW of diameter ~100 nm in the sub–diffraction limit using 325 nm excitation.
11. Polarized resonance Raman spectroscopy (RRS) study of a single AlGaN NW of diameter ~100 nm with optical confinement in the dielectric contrast of surrounding NWs is used to understand its crystalline orientation and the observations are confirmed with the transmission electron microscopy based structural analysis.

12. The visible light–matter (2.33 eV ; λ = 532 nm) interaction with AlGaN NW is studied using the near–field scanning optical microscopy (NSOM) technique. The observed significant absorption of visible light owing to the electronic transitions originated from the native defect related energy levels, as supported by PL studies.
13. The successful achievement of an optical spatial resolution up to ~20 nm for metal Au nanoparticles (NPs) even with a 150 nm apertured NSOM probe. The strong surface plasmon resonance (SPR) related absorption of metallic Au NP catalyst of diameter ~100 nm with an energy of 2.33 eV (λ = 532 nm) of the excitation laser is recorded with the help of NSOM technique.

7.2 Scope for future work

Relying on our present investigations, it is possible to extend the study for further explorations in different research area for AlGaN NWs. Along with the optical properties, study of transport properties and photocurrent can be performed for single, as well as ensembled nanostructures. A study of surface states and corresponding charge transport mechanism can be carried out using localized probes for the application in chemical sensing. In addition, the investigations of light–matter interactions at near–filed regime can be extended using tip enhanced Raman spectroscopic studies.